UNIVERSITA' DEGLI STUDI DI MILANO-BICOCCA

DIPARTIMENTO DI FISICA G. OCCHIALINI

SCUOLA DI DOTTORATO IN SCIENZE
CORSO DI DOTTORATO IN FISICA E ASTRONOMIA

CICLO XXV

THE CUORE POTENTIAL AS A COHERENT INTERACTION BASED OBSERVATORY FOR SUPERNOVA NEUTRINOS

Settore Scientifico Disciplinare FIS/04

Tesi di Dottorato di:
Matteo Biassoni

Tutore: Prof. Oliviero Cremonesi

Coordinatore: Prof. Giberto Chirico

Anno Accademico 2011-2012

Contents

CONTENTS

List of Figures

List of Tables

Introduction

It was about 82 years ago when the existance of the neutrino (also known as neutron at those times) was first postulated by Wolfgang Pauli, and it (the neutrino), just newly born, immediately saved the world (our physicists' world, at least) from the catastrophic falling of the energy (not to mention momentum and spin) conservation law, so much endangered by the continuous energy spectrum of the electrons from beta decay. What a feat for such a small particle! A very important particle then, the neutrino, but so elusive that, after almost a century, we still know very little about it: it is small, but we don't know how and why it is so small; we know they are three, one for each flavour, and we know they don't weight the same because they mix, but we don't know which is the haviest; we know it likes left but not right, but we don't know why; we know it has an antiparticle, but we don't know whether it is itself its own antiparticle and so on...

Despite all of these unknown properties are being studied by many experiments all over the world, neutrino is also proving an incredibly powerfull tool to explore other unknown physical phenomena that no other messangers can tell us something about. It brings information about extreme astrophysical phenomena, as well as the answer to the great cosmological questions; it can tell us what happens in the core of a collapsing star as well as how nucleons are distributed inside a nucleus; these are just some examples.

CUORE (Cryogenic Underground Observatory for Rare Events, see Chapter 1, Chapter 2, Chapter 3) is going to be an experiment whose main goal is to answer to some of the fundamental questions about neutrino's nature and properties; it is going to search for neutrinoless double beta decay, a nuclear process that is forbidden by the Standard Model and whose observation would prove that neutrinos are Majorana particles and possibly give some hint to solve the hierarchy problem. At the same time, CUORE is expected to be able to exploit neutrinos as a tool for the study of astrophyiscal phenomena, in particular the explosion of core-collapse supernovae.

The main goal of my PhD thesis is to demonstrate that CUORE detector will be able, given the expected performance in terms of active mass, energy resolution and background, to significantly detect the neutrinos emitted by a collapsing star at the end

of its life. The activity mainly consists in the theoretical calculation of the expected signal and sensitivity under different detector conditions in the case of a supernova explosion (see Chapter 4), and the development and testing of a dedicated online trigger and offline analysis tool (see Chapter 5). I developed numerical calculations and simulations with both C++ and Mathematica$^{\text{TM}}$ programming languages, and wrote a C++ code, that was inserted in the official CUORE analysis and DAQ software suite, to implement an online trigger system for supernova detection during data taking. This work led to a publication ([1]), an internal note and was presented in some national and international conferences (SIF2011, Neutrino2012, IFAE2012).

Besides the thesis topic, my three-year PhD experience was mainly devoted to the advancement of CUORE project; in this perspective I was assigned to some technical tasks, both of hardware and software nature. Starting from 2011, I actively took part in the construction of CUORE-0 experiment (CUORE first tower built and operated like a stand-alone experiment as well as a demonstrator for the cleaning and building protocols to be used in CUORE construction) at LNGS (Laboratori Nazionali del Gran Sasso, Italy), with a major effort in the work of connection of the temperature reading devices to the detectors, by means of a semi-automatic robotic system for the glue deposition and the detectors handling in ultra-clean environment. This activity includes the management of a robotic system composed by a cartesian robot for the deposition of glue spots on detectors crystals, and an anthropomorphic robot for the handling of crystals and semiconducting sensors without the direct intervention of the operator. I developed the competences for programming the cartesian robot movements in order to tune the parameters (time, speed, amount of deposited glue) of the process. In the same context, I worked on the development of an imaging acquisition and elaboration system for the online monitoring and quality check of the process. I also co-operated in the set up of a system for the stabilisation of the temperature in the working environment, i.e. a ultra-clean glove box built inside a clean-room. During the prolonged work in clean-room, I acquired the competence and the attitude that are required to work in ultra-clean environments.

During summer 2012 I led a part of the cooling down procedure that brought CUORE-0 to the base temperature in the Hall A cryostat at LNGS. Some major problems connected with the cryogenic system (contamination and ^{3}He depletion of the helium mixture used in the dilution refrigerator) that prevented the detectors from reaching the base temperature were analyzed and solved.

A fraction of my time was also devoted to some collateral activities, some of them connected to the study of some aspects and problems of cryogenic detectors in general. I carried out a study of the response of bolometric detectors, like the ones used

in CUORE, to the interaction of particles in ancillary parts of the detector itself, in particular in the glue connecting the sensors to the absorber. An original measurement was performed with an alpha source dissolved in the glue. I built the detector and analysed the data developing a model to explain the observed behaviour. The results from this measurements are likely to be published in the near future.

I designed and built the detector that collected the data used for the publication of [2].

Starting from late 2011 I also joined the INFN-founded ABSURD experiment (A Background SUrface Rejection Detector, Section 3.4). ABSURD is an R&D project for the development of alpha background rejecting bolometers; I contribute to the project with my experience in building and analyzing data from cryogenic detectors and today I'm deeply involved in the construction of silicon-based bolometric light detectors featuring an innovative temperature measurement system (see Section 3.4.2).

During many cool down cycles of bolometric detectors at LNGS (and marginally in Milano-Bicocca University) I developed a fairly large experience in dilution refrigerators operating procedures and problem solving, in the management of cryogenic liquids, low temperature measure instruments and high vacuum/high pressure devices and systems in general.

CUORE and ABSURD related R&D activities often require the building of cryogenic detectors. These detectors are almost always realised starting from an original design optimised for the purpose of the particular activity. I developed a fair experience in this field and, in order to design the detector assembly and interact with mechanical workshops for its construction, I learnt to use 3D modelling software (Autodesk^{TM}Inventor^{TM}in particular).

Chapter 1

The CUORE experiment

The CUORE experiment is the result of more than twenty years of development of the bolometric technique applied to the Physics of rare events. Mainly conceived for the search for neutrinoless double beta decay ([3]), its detector's performance and unique features give it the potential for a much wider range of applications in the low rate particle and nuclear Physics field.

1.1 Bolometric technique

CUORE detectors (often reffered to as *thermal detectors*) are based on the bolometric technique which represents the theoretically simplest approach to a calorimetric measurement of a particle's energy. An *absorber* is kept at a given temperature when a particle interacts in it releasing its kinetic energy via the standard radiation-matter interactions (depending on the particle energy). After a time lag (whose duration depends on many factors but is usually short enough to fit the time requirements of a low rate particle detector) all the deposited energy, independently of the processes responsible for the deposition itself, is converted to heat. This heat contribution produces a rise in the temperature of the absorber which depends on the total energy originally deposited by the radiation. An electrical signal proportional to the energy is then generated by means of a temperature sensor, or *thermistor*, which is coupled to the absorber and is sensitive to its temperature variations. The single elements of a thermal detector, i.e. the absorber, the thermistor and the thermal couplings between them, are described hereafter.

1.1.1 Absorber

The absorber is the element of a thermal detector where the energy carried by the inter-acting particle is released and converted into a measurable temperature variation. The time evolution of the effects of the radiation interaction in the absorber is described from the microscopic point of view in the following. The most relevant processes responsible for the transfer of the energy from the particle to the absorber are ionization and atomic excitations. Recombination and relaxation of the excited states are characterized by very short time constants. The result of this first processes is the production of out-of-equilibrium vibrational excitations of the absorber lattice, called non-thermal phonons[1]. The shape of this non-thermal component of the phonon spectrum depends on the mechanisms responsible for its production, i.e. on the processes involved in the energy deposition. The non-thermal phonons lose energy by interacting with lattice impurities and crystal surfaces and the phonon specrum evolves (on a timescale of picoseconds) until a new equilibrium condition is reached, with a new higher temperature (see Fig. 1.1).
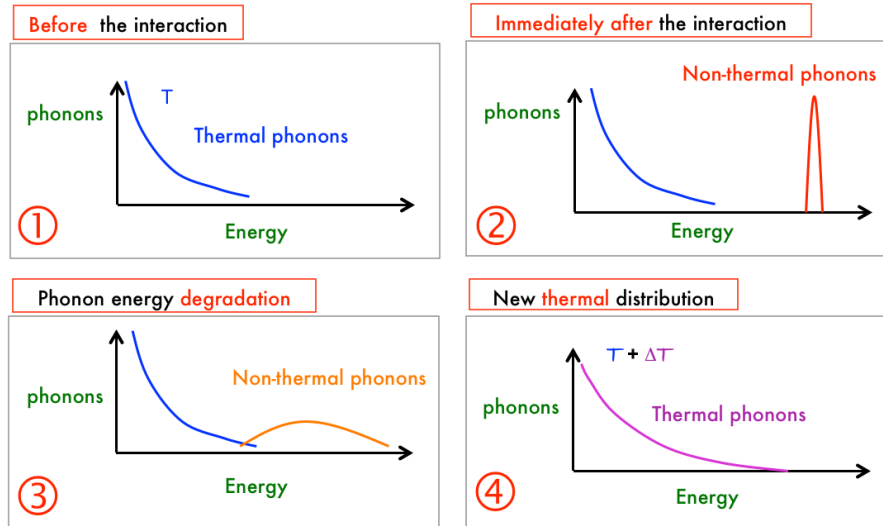
Figure 1.1: Sketch of time evolution of phonon spectra after particle interaction

---

[1]Phonons are the quanta of vibration of a crystal lattice; they can be interpreted as particles to which one can associate an energy. In this way the thermal status of a lattice can be described through the spectrum of its phonons. The mean energy of the phonons spectrum at thermal equilibrium is usually referred to as the temperature of the crystal.

The difference between the old and new temperature of the lattice is associated to the energy released by the particle.

A crucial parameter for the absorber in a thermal detector is its heat capacity, which connects the temperature variation to the energy deposition as in Eq. 1.1:

$$\Delta T = \frac{E}{C(T)} \tag{1.1}$$

where ΔT is the temperature variation induced by an energy deposition E in an isolated absorber with a heat capacity $C(T)$[2]. For a given energy deposition, the smaller is the heat capacity of the absorber the larger is the temperature variation and the more sensitive is the detector. For this reason only some materials can be used as absorber in a thermal detector. Dielectric crystals are in particular the best choice. The heat capacity of a non-superconducting diamagnetic solid at low temperature is in general the sum of the contributions from the lattice and the electron component; the specific heat for a solid is (Eq. 1.2):

$$c(T) = c_l(T) + c_e(T) \tag{1.2}$$

The lattice specific heat is described, for temperatures below the Debye temperature Θ_D, by the Debye law (Eq. 1.3):

$$c_l(T) = \frac{12}{5}\pi^4 N_A k_B \left(\frac{T}{\Theta_D}\right)^3, \quad T < \Theta_D \tag{1.3}$$

where N_A and k_B are the Avogadro number and the Boltzmann constant respectively. The specific heat for the electrons is (Eq. 1.4):

$$c_e(T) = \frac{ZR}{\Theta_D}\pi^2 \frac{T}{\Theta_F} \tag{1.4}$$

where Z, R and Θ_F are the number of conduction electrons, the gas constant and the Fermi temperature respectively. At low temperature the lattice specific heat decreases much faster than the electrons one, thus making a dielectric and diamagnetic crystal, for which the elctrons don't contribute to the specific heat, more suitable as for using as absorber in a thermal detector. The Debye temperature of the crystal, written in Eq. 1.5 as a function of the material properties (h is the Plank constant, N the number of atoms in the volume V of the solid and c_s the sound speed in the material), is a

---

[2]It is worth noting that, even if the heat capacity is in general a rapidly changing function of the temperature, in most practical cases the variations are so small compared to the starting temperature that the relation can be considered linear.

relevant parameter in the choice of the absorber as well: the larger it is, the smaller is the heat capacity of the crystal at a given temperature.

$$\Theta_D = \frac{hc_s}{2k_B}^3 \sqrt{\frac{6}{\pi}\frac{N}{V}} \tag{1.5}$$

1.1.1.1   Material choice

In CUORE the absorber is made of tellurium dioxide (TeO_2). TeO_2 is a dielectric and diamagnetic material which can be grown in macroscopic crystals with good crystallographic properties.

The choice of TeO_2 is motivated by many factors. First of all ^{130}Te is a double beta decay emitter and its natural isotopic abundance is very high (34.167% [4]), thus allowing the use of tellurium compounds without the need of isotopic enrichment (which is, in general, a very complex and expensive procedure). Moreover, tellurium is a heavy element and hence represents a large fraction of total tellurium dioxide mass. ^{130}Te contributes to the total mass of CUORE TeO_2 crystals for 27.8%, corresponding to 206.2kg. Being a large atomic number nucleus, tellurium shows a very favorable cross section for coherent processes involving neutrinos and possibly weakly interacting dark matter candidates (Section 2.3).

Another advantage of TeO_2 is that it is relatively easy to grow in large mass dielectric and diamagnetic crystals with a very good purity level and a high Debye temperature (see Eq. 1.5). CUORE crystals are 750g, $5 \times 5 \times 5 cm^3$ cubic shaped and contaminations in the bulk are known to be very low (see Chapter 3).

For what concerns the main goal of CUORE, the search for neutrinoless double beta decay, ^{130}Te is a good candidate thanks to its relatively favorable nuclear matrix element and a high Q-value (2527keV) (that puts the double beta decay signature in a region of the energy spectrum where the background contributions are small, see Chapter 3).

1.1.2   Sensor

As described above the absorber is the element of the thermal detector where the radiation releases its energy, which is quickly converted into heat and produces a proportional increase of the absorber temperature. The second element of a bolometer is a sensor which must be able to measure the temperature variation of the absorber generating a signal (usually electrical) that can be eventually acquired and processed to extract the maximum amount of information on the interacting radiation. In CUORE this sensor is a NTD[3] germanium thermistor. The NTD thermistors [5] are germanium devices

---

[3]Neutron Trasmutation Doping

whose doping level is precisely tuned by exposing them to a controlled reactor neutron flux, and are then cassified as *Semiconductor Thermistors*[4]. Semiconductors behave like insulators (their resistivity is very high at room temperature) but they have a gap between valence and conduction band as small as few eV, thus becoming conductors as the temperature exceeds the value at which $k_B T$ is larger than the gap. When they are doped introducing impurities in the lattice (by Neutron Transmutation Doping, for example) new energy levels are created within the gap, allowing conduction at low temperature by the *hopping mechanism*. In this mechanism the electrons, when pushed to an energy level within the gap by a phonon interaction, can move in the lattice by tunnelling (*hopping*) through the potential barrier separating the impurity sites. The larger is the concentration of impurities in the lattice, and the closer are the energy levels generated by the impurities to the Fermi energy, the higher is the probability for an electron to jump and move within the lattice, and the smaller is the resistivity of the doped semiconductor. This conduction regime is well described by a model called *Variable Range Hopping*[6]. For a critical concentration of impurities, depending on the semiconductor and the dopant, the semiconductor stops behaving like an insulator and starts conducting like a metal. Around this critical condition, called *metal-insulator transition* (MIT)[7], the material resistivity shows a strong dependence on the temperature and it is well suited for using as a temperature sensor.

A parameter that characterizes the sensor performance is the logarithmic sensitivity η:

$$\eta = \left| \frac{\mathrm{d}\log R(T)}{\mathrm{d}T} \right|. \tag{1.6}$$

Equation 1.6 is equivalent to

$$\frac{\mathrm{d}R}{R} = \eta \frac{\mathrm{d}T}{T}. \tag{1.7}$$

The larger is η in Eq. 1.7, the larger is the resistance variation of the sensor for a given temperature variation. The VRH model predicts, for germanium NTDs, a dependance of the resistivity on the temperature described by the law in Eq. 1.8:

$$\rho(T) = \rho_0 \exp\left(\frac{T_0}{T}\right)^{\gamma} \tag{1.8}$$

where ρ_0 and T_0 are characteristic parameters of the thermistor and depend on the doping level, while $\gamma = 1/2$. From Eq. 1.8 using Eq. 1.6 the resistance of the termistor

---

[4]Another common type of temperature sensors used in thermal detectors are the *Transition Edge Sensors* (TES).

as a function of the temperature can be derived:

$$R(T) = R_0 \exp\left(\frac{T_0}{T}\right)^\gamma \tag{1.9}$$

where R_0 depends on the geometry of the sensor. Standard CUORE NTDs are characterized by the following parameters:

$$R_0 \simeq 1.15\Omega, \quad T_0 \simeq 3.35\text{K} \quad \text{and} \quad \gamma = 1/2. \tag{1.10}$$

The corresponding resistance (R_S) at the working point temperature $T_S \simeq 10\text{mK}$ is of the order of 100MΩ.

1.1.3 Sensor-absorber coupling

As described in Section 1.1.2 the resistance of the thermistor depends on its temperature. For the thermal detector to work properly it is crucial that the sensor and the absorber are thermally coupled in such a way that the information contained in the temperature evolution of the absorber is transmitted to the sensor and converted into a resistance variation. In CUORE the thermal link between the NTD and the crystal is provided by a matrix of epoxy glue[5] spots. Since the glue is an amorphous material only thermal information (i.e. thermal phonons) can be transmitted from the absorber to the thermistor, meaning that the thermistor is, in good approximation, always at the same temperature of the crystal. The time evolution of the sensor resistance reflects the time evolution of the absorber temperature provided resistance-temperature relation of Eq. 1.9.

The choice of coupling the sensor and the absorber with an amorphous material has the main advantage of being simple and cheap, but does exclude the possibility of extracting any information other than the total energy deposited in the absorber. Any information coming from the spectral shape of the phonon signal generated by the interaction of the particle is in fact lost because non-thermal phonons cannot diffuse through the glue interface.

1.1.4 Working point and bolometer operation

To read the resistance variation of the sensor a simple bias circuit is used: a bias voltage V_B is generated by a ultra-stable voltage generator closed on a load resistor (with resistance R_L) in series with the thermistor. The load resistance is chosen much

---

[5]Araldite bicomponent glue is used because of its good performance at low temperature and low radioactivity level

larger than the thermistor resistance R_{bol} (and its temperature-induced variation). In this way the current I that flows in the circuit (Fig. 1.2) is constant and the voltage drop across the thermistor (V_{bol}) is proportional to R_{bol}:

$$V_{bol}(T) = I \times R_{bol}(T) \tag{1.11}$$
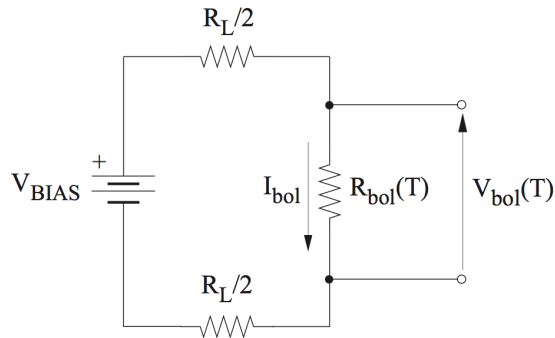
Figure 1.2: Circuit used for the bias and read-out of the bolometer: R_L is the load resistance, R_{bol} is the thermistor resistance.

The current I_{bol} flowing through the thermistor produces a power dissipation that heats up the thermistor itself in what is called the "electrothermal feedback". In static condition, i.e. when no additional power is injected in the system but the (small) one dissipated by the excitation current, the thermistor temperature (T_S) is

$$T_S = T_{hs} + \frac{P}{G} \tag{1.12}$$

where T_{hs} is the temperature of the heat sink, i.e. a large mass whose temperature can be assumed constant, and G is the conductance to it. Given 1.12 and 1.9 the dependence of the resistance on the dissipated power is reported in Fig. 1.3 for various values of the base (zero-power) temperature, i.e. the heat sink temperature.

The effect of the electrothermal feedback is the non-ohmic behavior of the thermistor, whose I-V relation is depicted in Fig. 1.4 (the curve is called "load curve"). For small currents the relation is nearly linear but increasing the current the slope increses until the so called inversion point (IP) is reached. A further increase of the current flowing through the thermistor corresponds to a drop of the voltage due to the significant heating and consequent reduction of the resistance.
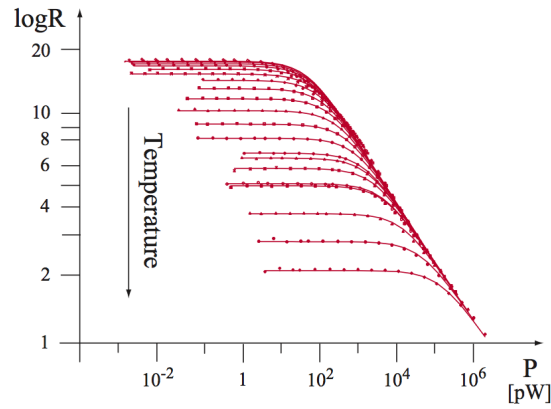
Figure 1.3: Resistence of the NTD thermistor as a function of the power dissipated in the "electrothermal feedback". Lower resistance at zero power correspond to higher heat sink temperature (base temperature).
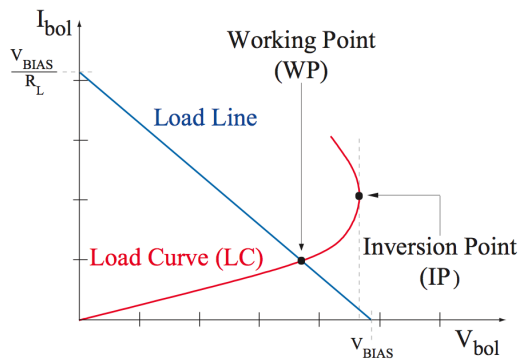
Figure 1.4: Relation between the current flowing through a NTD thermistor and the voltage across it (load curve); the effect of the electrothermal feedback is evident in the non-ohmic behavior in proximity of the inversin point where a further increase of the current corresponds to a reduction of the voltage.
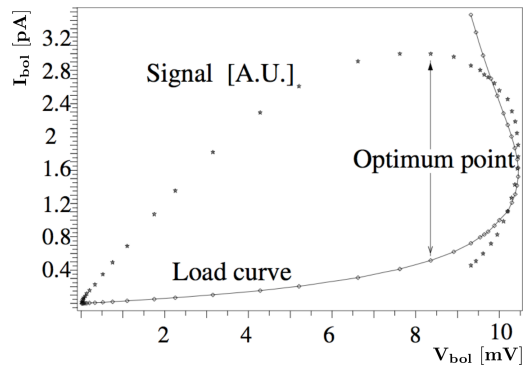
Figure 1.5: Sampling of the ampitude of a pulse (generated by a fixed energy deposition) varying the static voltage of the bolometer (i.e. varying the bias voltage). The working point corresponds to the value of V_{bol} where the amplitude of the signal is maximum.

In static condition, i.e. when the system is not perturbed by any external energy injection, the thermistor electrical and thermal parameters are described by a point on the load curve.

The dynamic response of the thermistor can be calculated as follows: for a thermistor at a temperature T_S corresponding to a static resistance R_S (always considered $R_S \ll R_L$), the injection of an amount E of energy generates a variation of the voltage

$$\Delta V = \eta V \frac{\Delta T}{T_S} = \eta \sqrt{P R_S} \frac{E}{C T_S} \qquad (1.13)$$

where η is the sensitivity defined in 1.7, C is the heat capacity of the absorber and P is the power dissipated on the thermistor by the current flowing in the bias circuit. Relation 1.13 vanishes both for $P \to 0$ (if no excitation current flows through the thermistor no voltage drop can be measured) and $P \to \infty$ (after the inversion point of the load curve, increasing the power dissipation correspond to reducing the resistance that vanishes at high temperature). Thus a maximum of ΔV from 1.7 exists for a specific value of P (i.e. of I_{bol} or V_{bias}) corresponding to the maximum signal for a given energy deposition. This configuration is called working point and is usually determined experimentally: a fixed amount of energy is released in the bolometer (using a dedicated heater or, in principle, a monochromatic radiation) and the amplitude of the corresponding pulse is recorded varying the bias voltage. In Fig. 1.5 the amplitude of the signal (in arbitrary units) for a set of value of V_{bol} is superimposed to the load curve and the working point is represented. The thermistor will be operated with the bias current (bias voltage) that corresponds to the voltage across the bolometer that vary the most when a given variation of the temperature is generated.

1.2 Detector assembly

CUORE detector design is based on the concept of modularity, both for scalability purposes and for scientific reasons. A basic structure, the so called "single module", is repeated a number of times in the space to produce a matrix of detectors whose spatial structure is optimized.

1.2.1 Single module

The single module is the atomic structure of CUORE detector and is represented by four bolometers, each composed by a tellurium dioxyde crystal (weighting 750g and measuring $5 \times 5 \times 5 \mathrm{cm}^3$ each) equipped with an NTD thermistor and a silicon heater. The four bolometers are held in position, in a 2×2 matrix, by a copper structure

consisting of two frames and four spacers (columns). The crystals don't touch the copper directly but sit on PTFE spacers. These PTFE parts have a double purpose:

- limiting the direct thermal link between the absorber and the heat sink;

- firmly holding the crystals to minimize vibrations; the special "z" shape exploits the differential thermal contraction of copper and PTFE to generate the right amount of pressure on the crystals.

Fig. 1.6 is a picture of a single module of the kind used in CUORICINO[8] experiment, which is based on the same building principle. CUORE single modules (more properly called floors since they are always assembled in a multi-floor structure) are very similar but for the fact that each frame is shared by two adjacent floors in order to further reduce the amount of copper facing the bolometers and the distance among the bolometers themselves[6].

1.2.2 Tower and array

The next higher level structure composing the CUORE detector is a tower (Fig. 1.8) made of 13 floors, each being one of the single modules described in 1.2.1. Each tower has some ancillary structures designed to host the wires that bring the signal from the bolometers to the read-out electronics and the power to the heaters. These structures are made of copper and designed to accomplish a double function:

- shield the bolometers against any radiation coming from the wires (even if they are carefully selected to meet stringent specifications on their radiopurity, they are made of materials that are usually not suited to high radiopurity enivironment);

- thermalize the wires that go from a warmer part of the system directly to the bolometers that are usually the coldest part, avoiding the bolometers to be loaded with parassitic power.

To realize the CUORE detector 19 tower will be mounted side by side in a closely packed cylindrical configuration (Fig. 1.7), designed to minimize the distance among the bolometers. The whole array, consisting of a total of 988 bolometers for a total mass of 741kg (817kg accounting for copper and PTFE structures, of which 206kg are ^{130}Te) will be enclosed by a copper shield and mounted in the cryostat (see Section 1.3).

---

[6]For this reason a CUORE-like single module cannot exist but connected to the others in a larger structure, see 1.2.2.
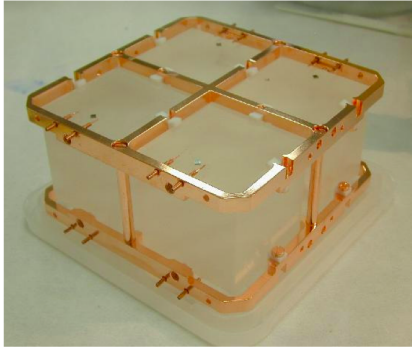
Figure 1.6: Single module of the kind that used to form CUORICINO experiment; CUORE single modules are very similar but each frame is shared by two floors to minimize the amount of copper and the distance among the crystals.
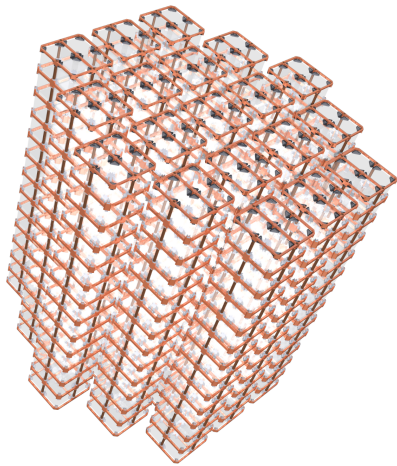
Figure 1.7: The full cylindrical array of 19 towers.
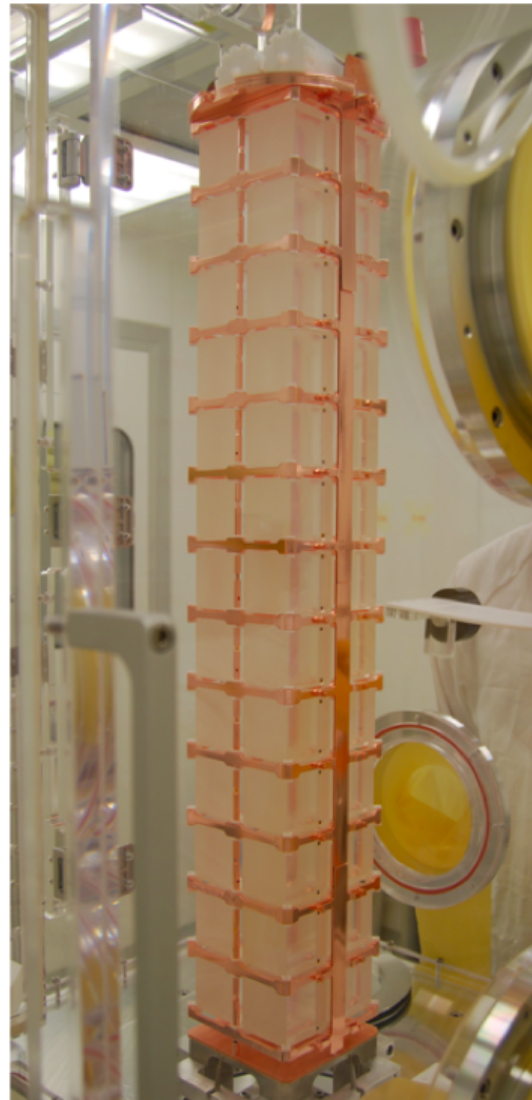
Figure 1.8: One of the towers of CUORE. It is composed by 13 floors of 4 bolometers each, with anchillary structures to host the wiring system.

The described modular structure has two main advantages. From the point of view of the building effort, a modular detector can be easily scaled once the technique for the construction of a single module exists. Procedures and protocols can be developed to ensure the minimum probability of contamination of the surfaces or of damaging of delicate parts. The number of tools and the space in ultra-clean environment are also minimized together with the cost and time required for building the detector.

More important is the scientific reason for the choice of this kind of structure: mounting the bolometers in a very closed array with the minimum amount of inactive material between the active elements (which corresponds to the segmentation of standard detectors) allows to optimally exploit the principle of time and space coincidence. By acquiring the data from all the elementary detectors at the same time, one can develop methods to extract information from the contemporary observation of events in different locations, i.e. on different bolometers. The possibility of detecting coincident events on adjacent bolometers allows CUORE to be used more like a highly segmented detector than a simple collection of single bolometers. This possibility can be exploited in many different ways:

- discriminate events that involve a single crystal from events that release energy in more than one crystal (particularly usefull in the search for double beta decay, Section 2.1);

- study the sources of background located near the surface of the crystals and hence sharing their energy among different crystals;

- discriminate the residual background coming from and induced by cosmic muons by "tracking" them and thus tagging secondary events;

- identify bursts of events (induced both by background or physics phenomena) reducing the probability of pileup, Chapter 5;

- study correlated noise.

Some of these uses of the coincidence technique will be better described in the following.

1.3   Cryogenic setup

In order to exploit Eq. 1.5 to minimize the heat capacity of the crystal and maximize the sensitivity, bolometers are operated at very low temperature (of the order of few to few tens of millikelvin, depending on the sensor being used). Cooling about one ton of

material to such a low a temperature is a technological challenge by itself. A two stage cryogenic system will be used (see Fig. 1.9 for the complete technical design).
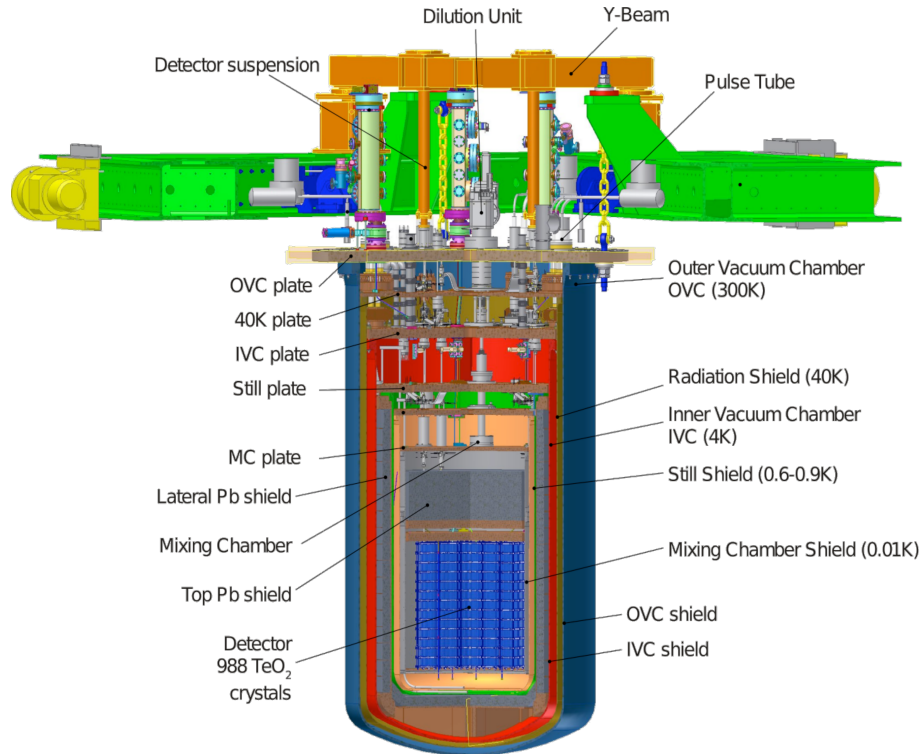
Figure 1.9: Complete technical design of CUORE cryogenic system.

Five 2-stages pulse tubes cool a first shield at a temperature of about 40K and a second one (the IVC) at few K, replacing the combination of liquid helium and *1Kpot* (pumped liquid helium) that was used in elder cryostats. A pulse tube is a cryogenic liquids free cryocooler without moving parts in the low temperature part of the device. It expoloits a series of low frequency compressions and expansions of a gas through heat exchangers to develop the needed cooling power. Since the only moving mechanical part is the compressor and it operates at room temperature and can be put at any distance from the pulse tube, this device is particularly suited for low noise applications because it is almost vibration free. This feature, combined with the possibility of continuous

operation (liquid helium systems operation time is limited by the need of periodically refill the helium reservoir) lead to the choice of pulse tubes as cryocoolers for the "high temperature" stage of CUORE cryostat.

The second stage is a dilution unit, the most common device for continuous operation in the millikelvin region. It is a closed circuit system that forces the circulation of a mixture of helium-3 and helium-4 with a system of pumps. During normal operation almost all the helium-4 is condensed in the coldest part of the circuit while helium-3, whose vapor pressure is higher than the helium-4 one, is partially pumped away from the so-called diluted phase of the mixture and sent back in the concentrated phase. The cooling power is provided by the endothermic diffusion of helium-3 from the concentrate phase to the diluted one, process that is sustained by the osmotic pressure generated by constantly pumping (hence depleting in helium-3) on the diluted phase. The boundary between the condensated and the diluted phases is in the so-called mixing chamber that is therefore the coldest part of the whole system and can reach temperatures as low as few millikelvin. A strong thermal link between the mixing chamber and the detectors has to be provided to efficiently remove heat from the bolometers, cool them down to the working temperature and keep them cold despite the unavoidable heat load. To minimize the heat load on the mixing chamber some tricks have to be adopted: all the wires bringing the signals from the detectors to ambient temperature are carefully thermalized at different stages to reduce the heat load; radiation shields at different temperatures, covered with multiple layers of super-insulating high refectivity material, surround the detectors in an onion-like structure to reduce the exchange of heat through radiation between surfaces at different temperatures; all the system is, of course, vacuum tight to prevent conduction and convection that would prevent the cooling. CUORE cryostat will be provided with two dilution units that will work in parallel.

To speed up the cooling from ambient to base temperature CUORE cryostat will use an additional "fast cooling" system consisting in a closed circuit where cold helium gas will be continuously circulated in the IVC volume.

1.4   Data acquisition

In a large scale experiment like CUORE a foundamental role is played by the data acquisition system (or DAQ system). It's primary goal consists in the manipulation of the voltage signal coming directly from the read-out and front-end electronics to produce a digital version of the information produced by the detector that can be stored and properly analyzed. In Section 1.4.3 we will describe a special version of the DAQ system that exploits, in the data acquisition phase, a filtering algorithm that is usually applied

in the offline analysis. The online implementation of this filter, however, guarantees better performances in some conditions. In general, however, the output of the DAQ system should be a reproduction of the signal coming from the detector preserving the maximum amount of information; it will be the responsability of the analysis, performed on the data, to extract, by means of ad hoc algorithms, the physical quantities of interest. If, in the CUORE detector, the hardware part of the DAQ system is unique, the part responsible for the recording of the data has, up to now, been implemented in three different versions that differ for the choice of the triggering technique and, at the end, for the conditions under which they give the best results (Section 1.4.2 and Section 1.4.3): a continuous data flow acquisition, a derivative trigger and an optimum (or matched) filter based technique, or optimum trigger. They will be described, with a particular attention to the last one which is crucial for the supernova trigger algorithm described in Chapter 5.

1.4.1 DAQ hardware and front-end electronics

The choice of the DAQ hardware has been matched to the features of CUORE bolometers signal. With a frequency bandwidth extending up to 12Hz, the typical rise time of the signal is of the order of few tens of milliseconds while the decay time is about one order of magnitude bigger (the time constants of the signal may vary from one bolometer to another due to the combined effect of many factors, but the average shape is in most of the cases similar to the one in Fig. 1.10).
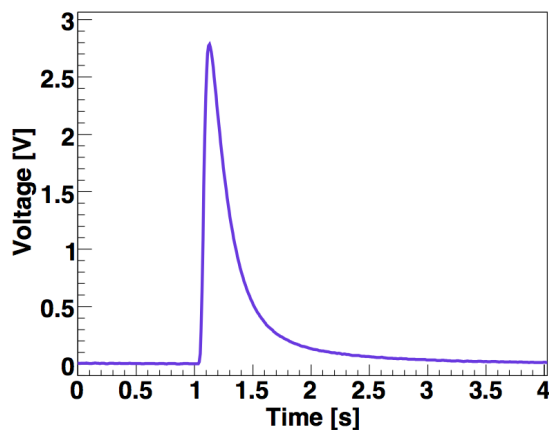
Figure 1.10: Example of bolometer signal with typical rise and decay times of the order of tens of milliseconds.

A sampling frequency of few hundreds Hz is therefore adequate to properly reconstruct the signal from all detectors.

To minimize the common mode noise, that can affect the very first part of the readout chain, the signals are acquired in a differential configuration of the front-end electronics, i.e. with the two poles of the signal, V_+ and V_-, symmetric with respect to the ground. In normal operation the signal is unipolar with the amplitude

$$V = V_+ - V_-$$

in the range [0,10]V. During the characterization of the detector working point (Section 1.1.4) the voltage can vary in a symmetric range [-10,10]V.

The electronics modules responsible for the digitization of the signal should guaratee that no deterioration of the energy resolution is introduced by the digitization process itself. Since CUORE bolometers are expected to operate with resolutions of the order of few keV [9] over a dynamic range of about 20MeV, an ADC with at least 16 bit resolution must be adopted.

Finally the digitizer modules must be able to handle a number of samples large enough to acquire a time window of some (usually 5) seconds to ensure that the recorded data contains all the signal (leading edge and all the decay phase), without the loss of any relevant frequency, plus a segment of baseline before the signal (called pre-trigger) that is used during the analysis to determine the exact temperature of the detector when the interaction occurred.

National instruments M-series boards fullfill the adove described requirements:

- 18-bit resolution analog-to-digital converter (ADC) with multiplexer to digitize many channels in parallel;

- programmable sampling frequency up to 500kSamples/s;

- internal reference signal and calibration circuit to correct gain and offset errors, to guarantee stability over time and temperature changes;

- programmable input range up to [-10,10]V, anti-aliasing filter (40kHz or 750kHz) and trigger.

The boards are hosted in a PXI standard crate. A back-panel provides the signals routing and the possibility to share a common clock source. The communication PXI chassis and the data acquisition computers is controlled by a proper interface that implements a communication protocol over an optic fiber, thus guaranteeing high data transfer rate and complete elctrical isolation between the DAQ system and the DAQ computers.

1.4.2 Derivative trigger and continuous data acquisition

The CUORE data acqusition (and slow control) software is called *Apollo*. It is almost completely a custom software, the only exceptions being the National Instruments drivers used to interface with the DAQ boards, and the ROOT[7] software package used for online data quality monitoring and data handling and storage. Written in C++ programming language and running on Scientific Linux computers, *Apollo* is designed with a high level of modularity, to provide easy scalability with the number of acquired channels and subsystems. It is composed by several parallel processes distributed over different computers; communication and data transfer between different processes exploits standard network connections and protocols. The choice of using a distributed system results in a flexible and scalable system that exploits standard and cheap computing resources.

Many of the *Apollo* processes access the CUORE database, an online repository of all the information about the geometry of the detector, the mapping and settings of various readout components, the performed measurements and relevant quantities evaluated in the off-line analysis.

In Fig. 1.11 a sketch of the DAQ system is reported. For a detailed description of the role that each component plays see, for example, [10].

Since the event rate in a bolometer for rare events physics is expected to be low, and the sampling frequency is typically low, a software trigger was implemented. This means that the data are continuously digitized and pre-processed to search for events by means of software implemented algorithms. This system alows very customizable configurations.

The trigger algorithm implemented in CUORE mainly for the search for high energy events (like $\beta\beta0\nu$ events) is a derivative trigger: the difference in the signal amplitude of two samples at a given time distance (called *average*), which can be considered a discrete implementation of the derivative of the signal, is compared with a reference value (the *threshold*) sample by sample (see Fig. 1.12). If the derivative of the signal is larger than the threshold for at least a given number of consecutive samples, than the trigger fires and a trigger flag is assigned to the first sample that exceeded the threshold. By means of a Montecarlo simulation that reproduces the bolometers pulses and noise, and real data containing pulser events, the performance of the trigger was checked. As shown in Fig. 1.13 a threshold as low as few mV (that tipically corresponds to an energy threshold of less than 50keV) can be achieved with this simple and fast algorithm, mainly dedicated to high energy events.

Since the goal of the derivative trigger is to select only physical events, a random trigger

---

[7]http://root.cern.ch
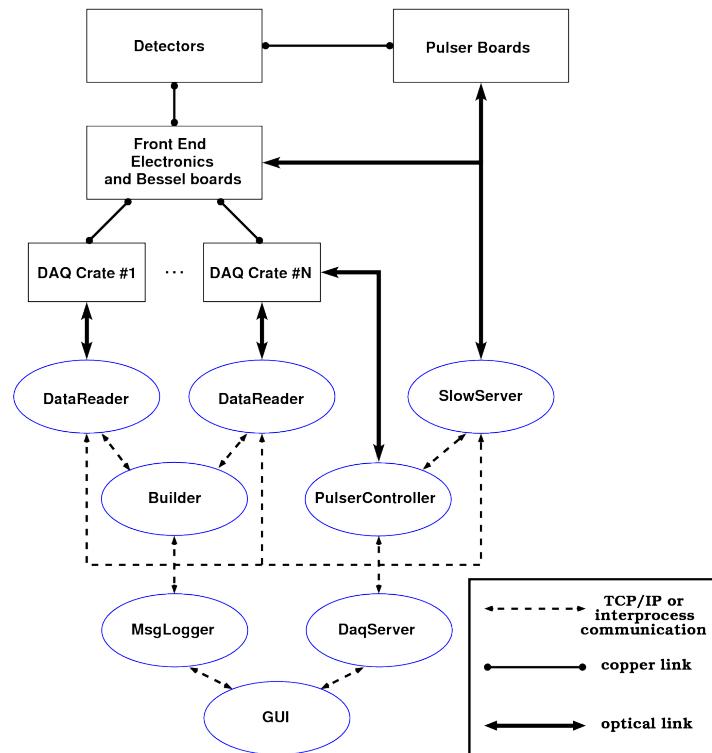
Figure 1.11: Sketch of the DAQ system with main components, processes and connections.

is used in parallel to acquire noise-only baselines that are used in the offline analysis to apply matched filtering techniques.

If the derivative trigger is simple and effective in triggering high energy events down to some tens of keV, the main problem of this kind of trigger is that it can be critically inefficient at low amplitudes thus leaking important informations. Any analysis tool, as sofisticated as it can be, will only be applied to those signals that where selected by the trigger. Since every bolometer is a stand-alone detector with its unique features, many studies can be performed on the signal even when no evident pulse is present. The possibility of recording the data flow continuously has therefore been implemented. The data coming from the digitizer boards are recorded sample by sample, without any selection or reduction of the information content. Thanks to this approach, the original signal can be reprocessed offline with state of the art (and also slow) algorithms, allowing also cross checks for the results validation.
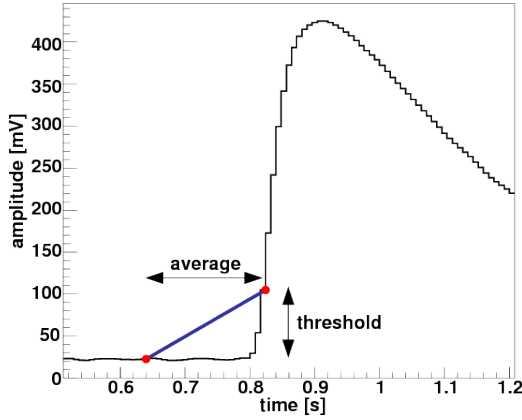
Figure 1.12: Sketch of the derivative trigger algorithm: for each sample, the difference between the signal amplitude of the considered sample and another sample at a fixed time distance is compared with a reference threshold.
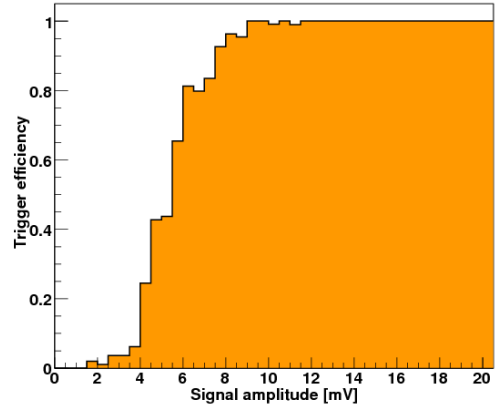
Figure 1.13: Efficiency of the derivative trigger algorithm evaluated by means of a dedicted Montecarlo simulation of bolometers pulses.

1.4.3 OptimumTrigger

The OptimumTrigger algorithm has been implemented to allow an online selection of phisical events also at low energy, where the standard derivative trigger fails and indiscriminately triggers noise fluctuations together with (few) true pulses. The OptimumTrigger is based on the same principle of the optimum filter (or matched filter) whose application to high energy data gave satisfactory results in the analysis of data from many bolometric detectors (in particular CUORICINO [8]). Optimum trigger application to data maximizes the signal-to-noise ratio, increasing the resolution. At the same time it returns pulse shape parameters that can be effectively used to discriminate physical pulses (the one expected from the detector when a partilcle interacts in the absorber) from noise, pile-up and spikes (fast pulses that can origin from electronics or particle interactions in elements of the detector different from the absorber, for example the thermistor). The basic idea of OptimumTrigger is to apply optimum filer to continuous data flow, than search the output of the filter (that should show the maximum signal-to-noise ratio) for pulses and eventually discard false triggers by means of the pulse shape parameters that the OptimumTrigger calculates.

Optimum filter

The optimum filter algorithm allows to estimate the amplitude A of a signal maximizing the signal-to-noise ratio. The filter expression is derived making the following assumptions:

- the detected signal y(t) can be parametrized as

$$y(t) = As(t) + n(t) \qquad (1.14)$$

  where $s(t)$ is the time evolution of the signal, A is the signal amplitude, and $n(t)$ is the noise;

- the shape of the signal $s(t)$ is known and doesn't depend on A;

- the noise $n(t)$ is stationary and its power spectrum $N(\omega)$ is known and well approximated by

$$N(\omega) = \langle n(\omega)n(\omega^*)\rangle \qquad (1.15)$$

  where $n(\omega)$ is the fourier transform of $n(t)$ and $\langle\rangle$ indicates the expectation value.

In the real case where the optimum filter is applied, the data are sampled, so that Eq. 1.14 becomes:

$$y_i = As_i + n_i \qquad (1.16)$$

where i is the sample index.

Let's start considering the particular case of the white noise. Since the fluctuations in the time domain are uncorrelated and gaussian distributed, the starting point is finding a filter that maximizes, as a function of the dispacement j (the position of application of the filter), the likelihood

$$L_j(y_i|A_j) = \prod_i \frac{1}{\sqrt{2\pi}\sigma} \exp\left[-\frac{(y_i - A_j s_{i-j})^2}{2\sigma^2}\right] \qquad (1.17)$$

i.e. a filter that makes the data y_i as close as possible to the signal s_i alone. σ is the noise RMS. The likelihood has to be maximized for each shift j, so

$$\frac{\mathrm{d}}{\mathrm{d}A_j} L_j(y_i|A_j) \propto \sum_i (y_i - A_j s_{i-j})s_{i-j} = 0 \qquad (1.18)$$

that leads to:

$$\hat{A}_j = \frac{\sum_i y_i s_{i-j}}{\sum_i s_{i-j}^2} = \frac{\sum_i y_i s_{i-j}}{\sum_l s_l^2} \ . \qquad (1.19)$$

$\hat{A}_i$ is the desired output of the optimum filter, hence corresponds to the filtered signal y_i'. Eq. 1.19 can be rewritten as a convolution

$$y_i' = y_i \otimes K_i \qquad (1.20)$$

where

$$K_i = \frac{s_{-i}}{\sum_l s_l^2} \tag{1.21}$$

is the "kernel" of the filter. If applied to the pure signal component s_i the filter leaves its amplitude unmodified, while the noise RMS is reduced to

$$\sigma'^2 = \frac{\sigma^2}{\sum_l s_l^2} \ . \tag{1.22}$$

The amplitude of the filtered signal is maximum (and equal to 1 if no noise is present) when j is equal to the time distance between the reference pulse s_i and the actual signal. Filtered signals will therefore be shifted by $-i_M$, where $-i_M$ is the time distance between the maxima of y_i and s_i. To align the maxima of the original and filtered signals, the filter kernel K_i can be shifted by $-i_M$. Moving to the frequency domain, Eq. 1.20 corresponds to

$$y'(\omega_k) = y(\omega_k) \cdot K(\omega_k) \tag{1.23}$$

that becomes

$$y'(\omega_k) = y(\omega_k) \cdot K(\omega_k) e^{-\imath \omega i_M} \tag{1.24}$$

once the alignement of the maxima is performed. From the above expression we obtain the transfer function of the filter:

$$H(\omega_k) = K(\omega_k) e^{-\imath \omega i_M} = \frac{1}{E_s} s^*(\omega_k) e^{-\imath \omega i_M} \tag{1.25}$$

where $E_s = \sum_l s_l^2$ is the energy of the signal s.

If the noise is not white and correlated the likelihood of Eq. 1.17 cannot be written. However a generic noise can be "whitened" by applying the filter

$$W(\omega_k) = \frac{1}{n(\omega_k)} \tag{1.26}$$

to the data y_i. The shape of the signal is modified as well (becoming $s(\omega_k)/n(\omega_k)$) and the transfer function of Eq. 1.25 becomes

$$H(\omega_k) = h\frac{s^*(\omega_k)}{n^*(\omega_k} e^{-\imath \omega i_M} \frac{1}{n(\omega_k)} = h\frac{s*(\omega_k)}{N(\omega_k)} e^{-\imath \omega i_M} \tag{1.27}$$

where h is a normalization constant that leaves unmodified the amplitude of the signal component s at the output of the filter:

$$h = 1 / \sum_k \frac{|s(\omega_k)|^2}{N(\omega_k)} \,. \tag{1.28}$$

In this case the noise power spectrum at the output of the filter will be

$$N'(\omega_k) = h^2 \frac{|s(\omega_k)|^2}{N(\omega_k)} \tag{1.29}$$

and the rms, using Eq. 1.28

$$\sigma'^2 = \sum_k N'(\omega_k) = h \,. \tag{1.30}$$

To apply the optimum filter obtained in Eq. 1.27 to conditions (that are necessary to apply the discrete convolution theorem that was used in the passage from Eq. 1.20 to Eq. 1.23), the data should satisfy two conditions:

- the data to be filtered (y_i) have to be periodic;

- the length of the filter H_i should be equal to that of y_i.

OptimumTrigger

If the filtered data are not periodic (as they are when the optimum filter is applied to a continuous data flow), a wraparound problem occurs because some of the data from the right side of the window will be moved during the convolution with the response functin to the left side, and vice-versa. To solve this problem the following steps are needed to build the transfer function:

1. build the optimum filter transfer function $H(\omega_k)$ of length M using the reference signal s_i and the noise power spectrum $N(\omega_k)$, both of length M;

2. transform $H(\omega_k)$ to the time domain using DFT, obtaining the kernel H_i of length M;

3. insert M zeros in the middle of H_i to obtain the new kernel H_i^d of length $2M$;

4. smooth H_I^d in proximity of the zero insertion[8], obtaining the smoothed kernel H_i^{ds};

5. transform H_i^{ds} back to the fraquency domain, obtaining the final transfer function $H^{ds}(\omega_k)$, of length $2M$.

---

[8]The smoothing of H_i^d is needed to avoid the Gibbs phenomenon, i.e. the fact that, if a discontinuity is created when the zeros are added to H_i^d, fake frequancies are introduced in its DFT.

Once the transfer function $H^{ds}(\omega_k)$ has been built, a data sample of length $2M$ can be filtered. The first and last $M/2$ samples will be spoiled because of the non-periodicity of the data, but the M samples in the middle will be correctly filtered. The continuous data flow is therefore processed filtering windows of length $2M$ overlapped by M and taking only the M central samples of each window as output (see Fig. 1.14).
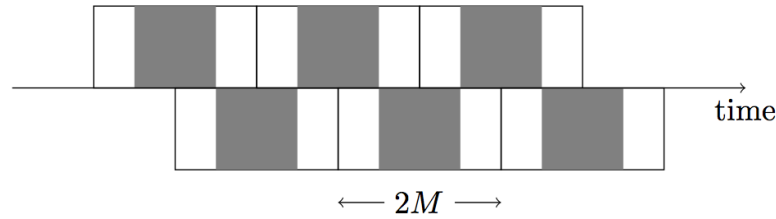
Figure 1.14: Sketch of the filtering procedure with OptimumTrigger: the continuous data flow analyzed in windows of length $2M$ (white rectangle), and only the M middle samples are correctly filtered (gray rectangle); the windows are overlapped by M samples to guarantee the continuity of the correcly filtered data.

The information needed in point 1 of the procedure for building the filter, i.e. the shape and the noise power spectrum, is obtained from data: the reference signal is obtained as an average of several large amplitude signals, while the noise power spectrum is obtained by averaging the noise power spectra (squares of the FT) of several baselines (sample windows where no signal is present). Once the filter is built, the filtering algorithm is applied to the data stream coming from the DAQ system and the output, compared to the original signal (see Fig. 1.15 and Fig. 1.16, both taken from [11]), show the following features:

- the noise fluctuations are reduced;

- the low-frequency components of the baseline are suppressed;

- the baseline has zero mean;

- the filter is sensitive to the shape pf the expected signal, hence different shapes are highly suppressed.

Once the data are filtered, the signals are triggered by means of a standard threshold trigger. The threshold is usually defined in terms of number of sigma of the filtered noise, that is known from Eq. 1.30. In this way a rough estimate of the average rate of
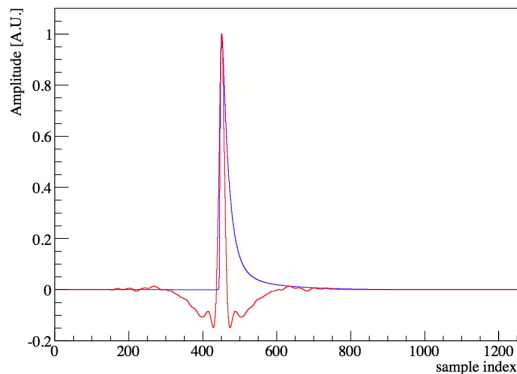
Figure 1.15: An example of the optimum trigger applied to the average pulse, i.e. a signal obtained by averaging several high energy pulses to reduce the noise as much as possible. The red pulse has the typucal shape of the output od the optimum trigger applied to signal only: it is symmetric and shorter than the original one but shows some oscillations around the maximum.
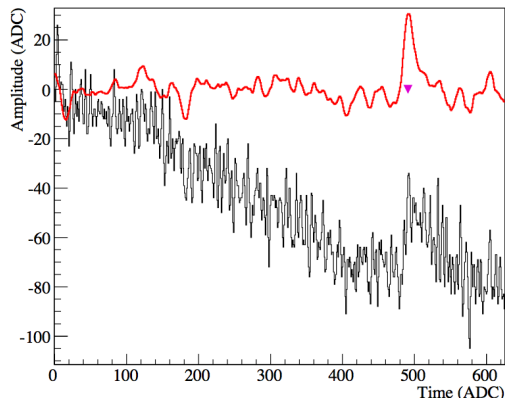
Figure 1.16: An example of the output of the optimum filter applied to a window where a signal is present but its amplitude is small compared to the noise fluctuations. The signal-to-noise ratio in the red line is highly increased, the overall slope is removed together with the noise fluctuations that are smoothed out. The signal will be much easier to trigger.

false triggers can be made. When a data sample exceeds the threshold, a local maximum is looked for in a moving window as large as the full-width-half-maximum of the output of the filter when applied to the average pulse. In this way the position of the maximum of the pulse should be located. A pile-up event where the second event amplitude is smaller than the first one is not triggered if the distance between the two maxima exceeds the width of the window. When the trigger fires the position of trigger that is recorded in the event is shifted back, with respect to the maximum, so that it lies in the middle of the rise of the pulse (the size of the shift is, once again, calcultated as the distance between the middle of the rise and the maximum of the filtered average pulse). This operation is needed because the analysis algorithms that are applied afterward expect the maximum to be after the trigger position.

Since the typical output of the optimum filter corresponding to a pulse has an oscillatory shape with several zeros befor and after the maximum, when a high energy event occurs, some of the secondary maxima can be also higher than the trigger threshold and hence be triggered as pulses. This problem has been solved by vetoing any trigger occurring in the regions where the secondary maxima lie. The inefficiency introduced by this veto is usually negligible if the low rate of events that characterizes bolometric detectors is considered.

The optimum filter has the ability of maximizing the signal-to-noise ratio in presence of signals having the expected shape, suppressing those characterized by a different one. Another feature has been implemented to further improve the performances of the OptimumTrigger: when a signal is triggered, a pulse shape indicator is also calculated. During the data analysis this indicator, called χ^2_{OT}, can be used to perform a further selection of the triggered pulses and reject noise events or pulses with wrong shape that, despite their amplitude being suppressed by the optimum filter, are nevertheless above threshold. χ^2_{OT} is calculated as follows: a triggered pulse is fitted using a cubic spline of the filtered average pulse, with the amplitude and position of the maximum as free parameters (the baseline is fixed to zero). The χ^2/ndf of the fit is used to calculate the shape indicator. Since the amplitude and position of the pulse are already known (the optimum filter is already a maximum likelihood fit of the data), this further fit only serves to remove digitization effects and to estimate the shape parameter. For this reason the free parameters of the fit are bound: the position can vary within a $[-1, 1]$ samples range arond the known position of the pulse, and the amplitude in the $[A, A(1 + \epsilon)]$, where A is the amplitude of the filtered signal and ϵ the maximum error in the amplitude that can be introduced by the digitization, evaluated as the difference between the amplitudes of the maximum sample and the sample right after in the filtered average pulse. The fit range is four times the full-width-half-maximum of the filtered average pulse. In Fig. 1.17 some examples of fits for pulses of different energies and shapes are shown. Eventually the shape indicator is computed as

$$\chi^2_{OT} = \sum_{i=0}^{L-1} \frac{(y'_i - f_i)^2}{\sigma_L^2 (L - 2)} \tag{1.31}$$

where y'_i is the filtered signal, f_i is the estimated fit function, and σ_L is the amount of noise expected in a window of length L. This calculation slightly differs from the expected chi-square in the fact the the noise at the denominator is not the average noise of the entire acquired window, but it is depleted in low frequencies because the fit window is shorter than the acquisition one. Therefore:

$$\sigma_L^2 = \sum_{k=M/L}^{M-M/L} \frac{|s(\omega_k)|^2}{N(\omega_k)} \ . \tag{1.32}$$

It is worth noting that the indicator χ^2_{OT} does not follow a true χ^2 distribution because, even if the expected value is still 1, the variance is not $2/(L - 2)$ because the errors at the filter output are correlated.
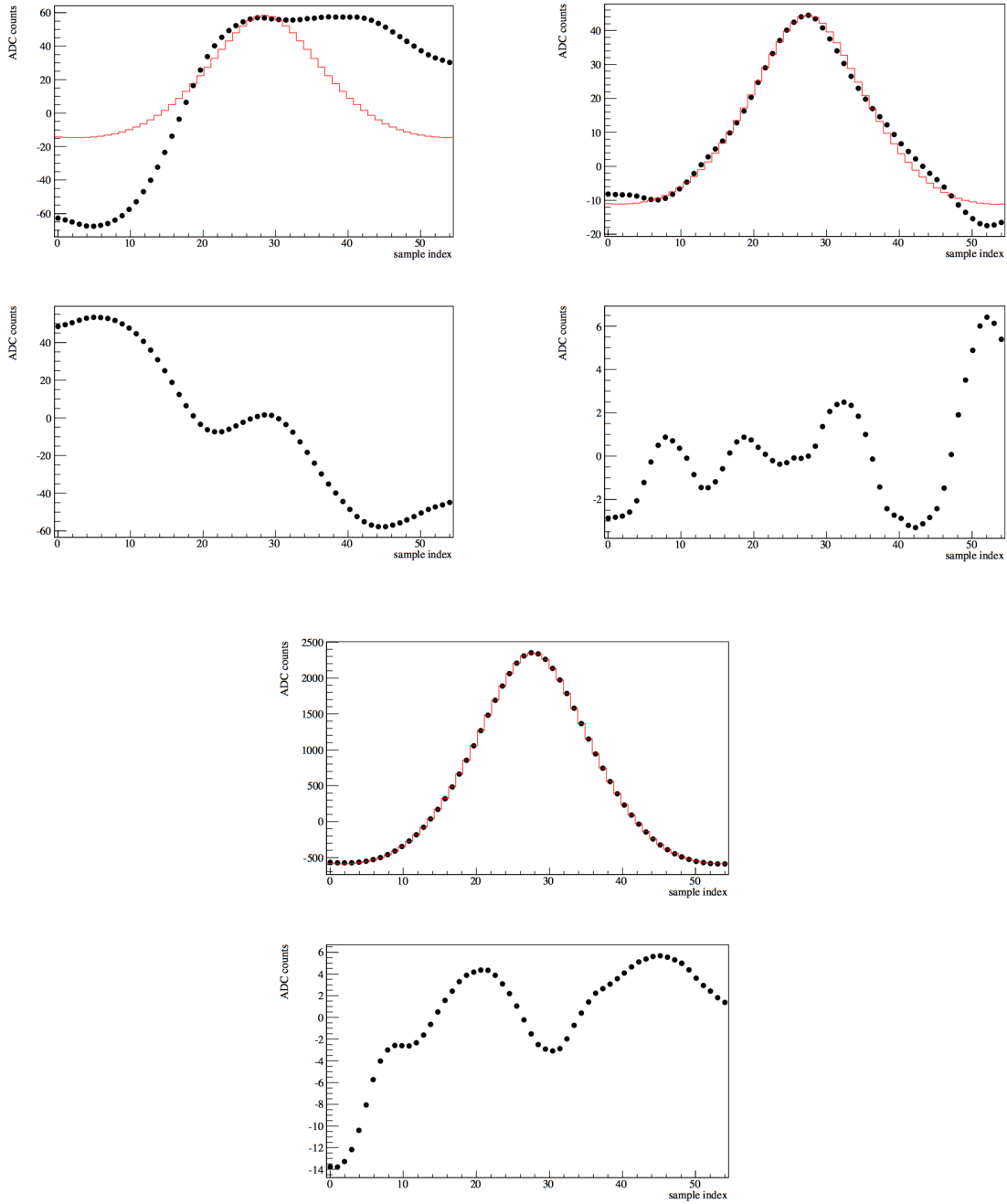
Figure 1.17: Some examples of pulses of different amplitude and shape, fitted with the spline of the filtered average pulse to calculate the pulse shape indicator, χ^2_{OT}. For each event, the top plot is the fitted pulse, the bottom plot are the residual. Top left: $E \sim 3 - 4$keV, $\chi^2_{OT} = 132$. Top right: $E \sim 3 - 4$keV, $\chi^2_{OT} = 0.5$. Bottom: $E \sim 200$keV, $\chi^2_{OT} = 2.3$.

In Fig. 1.18 the data from a test run are used to report a typical distribution of the χ^2_{OT} parameter versus the event energy. The events are clearly divided in several groups:
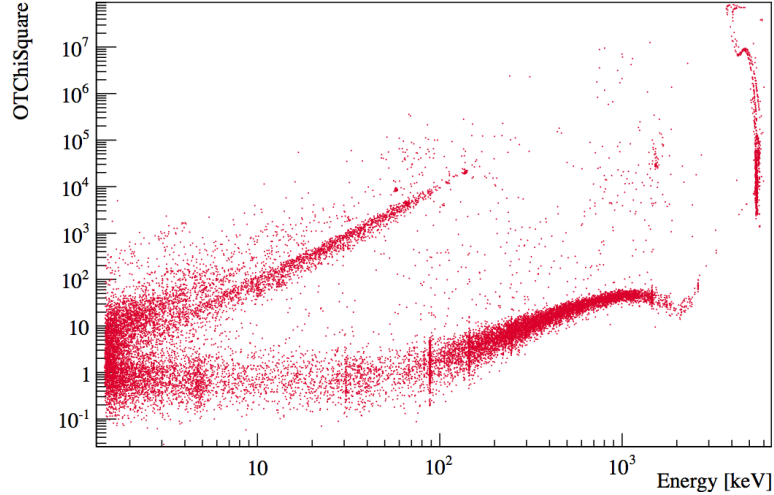
Figure 1.18: Example of χ^2_{OT} distribution versus the energy of the triggered event. The events om the lower band are particle induced and have a shape similar to the expected one. The upper band includes all those events whose shape differs from the expected one. As the energy decreases the separation between the two bands vanishes. The choice of a threshold on χ^2_{OT} implies an efficiency in the selection of particle events and the rejection of bad events.

the lower band, that includes the events with a smaller χ^2_{OT}, corresponds to particle-induced events whose shape is very similar to the average pulse that is used in the OptimumTrigger algorithm. The upper band events, and in general all the events with higher χ^2_{OT}, are tipically mechanical vibrations, electronic spikes and pile-up. Since the signal-to-noise ratio inevitably decreases when the amplitude of the signal decreases, the separation between the two bands also decreases as the energy decreases. This implies that, for a given threshold value of χ^2_{OT} that is set to accept or reject events, the cut efficiency, both for acceptance and rejection, depends in general on the energy.

In Fig. 1.19 the efficiencies for both signal, ϵ_S, and background, ϵ_B, events are reported (again, the data from the same test run used for Fig. 1.18 are used). Both ϵ_S and ϵ_B are calculated starting from the spectra of accepted and rejected events, with a given threshold for χ^2_{OT}. The lower radioactive peak (at about 30keV) is considered. Both specra are fitted with a background plus signal model and the output of the fit is used to calculate

$$\epsilon_S = \frac{S_A}{S_A + S_R} \, , \tag{1.33}$$
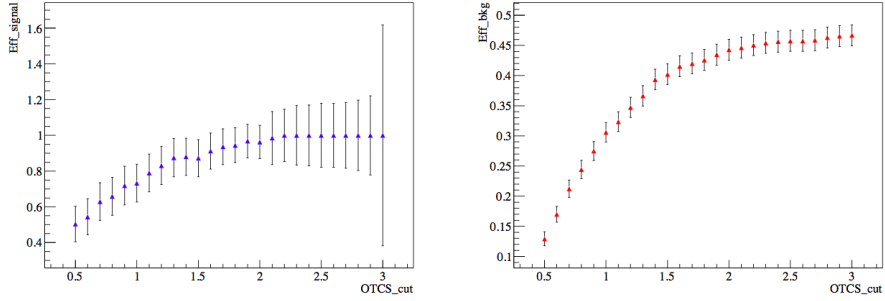
Figure 1.19: Efficiency of selection of signal and background events performing a cut on the χ^2_{OT} parameter with different thresholds. The cut in this example is performed on the events in an energy region centered around a 30keV peak. On the left, in blue, the efficiency for signal selection, ϵ_S, is plotted, on the right the efficiency for background, ϵ_B.
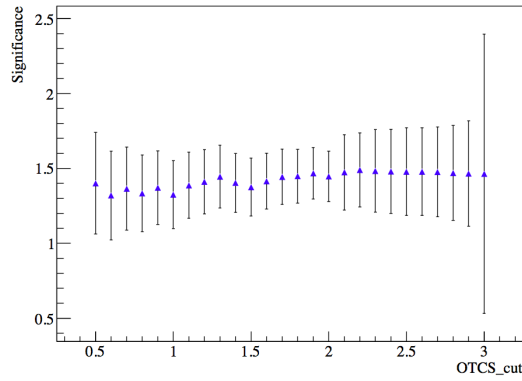
Figure 1.20: Statistical significance of the cut on χ^2_{OT} as a function of the cut threshold.

where S_A and S_R are the values of the fitted signal in accepted and rejected spectra respctively, and

$$\epsilon_B = \frac{B_A}{B_A + B_R} , \qquad (1.34)$$

where B_A and B_R are, of course, the values of the fitted background in the same spectra.

Finally, in Fig. 1.20, the statistical significance of the cut for each value of the threshold, calculated as

$$S = \frac{\epsilon_S}{\sqrt{\epsilon_B}} , \qquad (1.35)$$

is plotted.

Chapter 2

Physics with CUORE

In this chapter the physics potential of CUORE will be analyzed. The main phenomena that can be studied with this powerful observatory are briefly described, focusing in particular on supernova neutrinos (whose detection will be the topic of Chapter 4 and Chapter 5.

CUORE is an observatory focused on the study of the so-called rare event physics, i.e. all the particle physics phenomena that are characterized by a low probability of observation. The particle that is probably mainly involved in rare event physics is the neutrino. Neutrino physics is not only a challange from the experimental point of view due to the fact that neutrinos only interact via weak force with tiny cross sections, but also from the theoretical point of view it is one of the most intriguing branches of particle physics. Some of the phenomena where neutrinos are involved, indeed, seem to be a proof of the need for a deep revision of the theoretical models that have been used to describe the properties of elementary particles and their interactions until few years ago. The debate on the nature of the neutrino, in particular, cannot be fully contained in the framework of the Standard Model from which it already departed with the discovery of flavour oscillation.

CUORE main goal is indeed the search for neutrinoless double beta decay (Section 2.1) which is considered one of the golden phenomena for the study of the nature and absolute mass scale of neutrinos.

Together with the possibility of discovering phenomena that cannot be explained by the Standard Model, the observation (and precision measurement) of phenomena that it forsees but have never been observed experimentally cannot be considered of no interest. It is, on the contrary, a mandatory step towards the developement of theories that aim to go beyond the Standard Model. One of these phenomena is the neutrino-nucleus neutral current coherent scattering (we will call it NCCS in the following, Section 2.3).

It's obsevation turns out to be of great interest for an additional reason: since the cross section for ν-nucleus NCCS is, in a given energy range, much larger than the cross sections for any other process involving neutrinos, this penomenon allows the use of neutrinos as messangers of information from other physical phenomena, like supernova explosions. In particular, detectors with a relatively small mass like CUORE could observe neutrinos from supernovae that are usually considered within the sensitivity of detectors three orders of magnitude larger. This thesis is focused exactly on this topic (Chapter 4 and 5).

Another branch of the physics of rare events that is evolving very fast in the last years is the search for the Dark Matter. Detectors with the characteristcs of CUORE can search for a Dark Matter signal via the direct detection of WIMPS interacting with nuclei in the detector material. The potential of CUORE for DM detection will be discussed in Section 2.2.

2.1 Neutrino mass and double beta decay

In the Standard Model of particle physics the neutrino is a massless particle. It is a lepton with no electric charge and hence interacts only via weak force. Since weak interactions maximally violate parity, only left-handed neutrinos are involved in the interactions and no right-handed component is present in the theory. In the Standard Model fermions get a mass through a Dirac-like term of the Lagrangian that arises from the coupling of the fermion to the Higgs boson. This term contains both left- and right-handed components of the massive fermion. For this reason a mass for the neutrino cannot be justified in the Standard Model and a right-handed component, if exists, has to be sterile, i.e. no interaction term is expected for it.

2.1.1 Neutrino oscillations

Neutrino oscillations has not only been observed, but some experiments (SNO[12], Borexino[13], SuperKamiokaNDE[14], KamLAND[15], DayaBay[16], OPERA[17] and others) have been able to perform high precision measurements of mixing angles and squared mass differences. The theory that explains the oscillations among the flavors is well known and strongly supported by experimental evidences but requires the neutrino to have a property that is incompatible with the Standard Model: the mass.

The oscillation among the flavours is efficiently explained in a picture where neutrinos have mass and the mass eigenstates and flavor eigenstates don't coincide. The neutrino is emitted in a weak interaction as a flavor eigenstate, i.e. with a definite flavor, but propagates as a mass eigenstate, thus behaving like a particle with a defined mass. When

the neutrino is absorbed in a new weak interaction its flavor is once again defined, but can be different from the emission one because the flavor isn't conserved by the free particle Hamiltonian which is responsible for the propagation of the particle. The probability that a neutrino, emitted with flavor α, is detected with flavor β is:

$$P_{\alpha\beta} = \delta_{\alpha\beta} + 2\sum_{i \neq j}^{n} \Im\left[U_{\alpha i}U_{\beta i}^{*}U_{\alpha j}^{*}U_{\beta j}\right] sin(2\,X_{ij}) - 4\sum_{i \neq j}^{n} \Re\left[U_{\alpha i}U_{\beta i}^{*}U_{\alpha j}^{*}U_{\beta j}\right] sin^2 X_{ij} \,.$$

(2.1)

$U_{\alpha i}$ are the element of the mixing matrix that accounts for the relative rotation between flavor (greek letters) and mass (latin letters) eigenstates:

$$|\nu_\alpha\rangle = \sum_{i=1}^{n} U_{\alpha i}^{*} |\nu_i\rangle \,.$$

(2.2)

The rotation matrix U can be parametrized, in a three-flavors neutrino model, with six angles as follows:

$$U = \begin{pmatrix} 1 & 0 & 0 \\ 0 & c_{23} & s_{23} \\ 0 & -s_{23} & c_{23} \end{pmatrix} \cdot \begin{pmatrix} c_{13} & 0 & s_{13}\,e^{-i\delta_{CP}} \\ 0 & 1 & 0 \\ -s_{13}\,e^{-i\delta_{CP}} & 0 & c_{13} \end{pmatrix} \cdot \begin{pmatrix} c_{12} & s_{12} & 0 \\ -s_{12} & c_{12} & 0 \\ 0 & 0 & 1 \end{pmatrix} \cdot U_{MAJ}$$

(2.3)

with:

$$U_{MAJ} = \begin{pmatrix} e^{i\eta_1} & 0 & 0 \\ 0 & e^{i\eta_2} & 0 \\ 0 & 0 & 1 \end{pmatrix}, \quad c_{ij} = \cos\theta_{ij} \quad and \quad s_{ij} = \sin\theta_{ij} \,.$$

In Eq. 2.3 the symbols s_{ij} and c_{ij} stand for $\sin(\theta_{ij})$ and $\cos(\theta_{ij})$ respectively, and the three angles θ_{ij} (with $i = 1, 2, 3$) are the mixing angles. The angle δ_{CP} is the CP violating phase and accounts for CP violation in the leptonic sector. The last two angles, η_1 and η_2 are the Majorana phases. If neutrino is a Dirac particle, as it is in the Standard Model, U_{MAJ} is the unity matrix.

Going back to Eq. 2.1, X_{ij} contains the remaining neutrino properties and the experimental variables that affect the oscillations:

$$X_{ij} = \frac{\Delta m_{ij}^2 L}{4E} \,.$$

(2.4)

L is the distance between the emission and absorption points of a neutrino with energy E while $\Delta m_{ij}^2 = m_i^2 - m_j^2$ is the difference between the squared masses of the neutrino

mass eigenstates. If Δm_{ij}^2 vanishes Eq. 2.4 vanishes too, and Eq. 2.1 is simply

$$P_{\alpha\beta} = \delta_{\alpha\beta} \tag{2.5}$$

meaning that no oscillation should be observed. The experimental observation of neutrino oscillations is considered a proof that (at least two out of three) neutrinos have non vanishing masses. New theories beyond the Standard Model are needed to explain this fact.

2.1.2   Majorana neutrinos

As we already stated, in the Standard Model fermions get a mass through a Dirac mechanism involving both right- and lef-handed components of the fermion spinor. In terms of the fields representing the particle in the Lagrangian, a Dirac mass term has the form

$$\bar{\psi}\psi \tag{2.6}$$

and it is a Lorentz invariant (scalar). All the Standard Model fermion masses can be described with this kind of term, but also other scalar (Lorentz invariant) combinations can be accepted. If we consider the operation of charge conjugation that takes ψ into ψ^C a scalar term that fulfils the requirement for becoming a mass term can be written as

$$\mathscr{L} = \frac{1}{2}(m_M\bar{\psi}\psi^C + m_M^*\bar{\psi}^C\psi) = \frac{1}{2}m_M\bar{\psi}\psi^C + h.c. \tag{2.7}$$

where m_M is a complex parameter.

Rewriting Eq. 2.7 in terms of chirality eignestates (and considering that chirality eigenstates transform under charge conjugation as $\psi_{L,R}^C = (\psi_{R,L})^C$) we obtain two independent mass terms

$$\mathscr{L}^L = \frac{1}{2}m_L(\bar{\psi}_L\psi_R^C + \bar{\psi}_R^C\psi_L) = \frac{1}{2}m_L\bar{\psi}_L\psi_R^C + h.c. \tag{2.8}$$

$$\mathscr{L}^R = \frac{1}{2}m_R(\bar{\psi}_R\psi_L^C + \bar{\psi}_L^C\psi_R) = \frac{1}{2}m_R\bar{\psi}_L^C\psi_R + h.c. \tag{2.9}$$

with m_L and m_R two real Majorana masses. If we define two Majorana fields as

$$\phi_1 = \psi_L + \psi_R^C \qquad\qquad \phi_2 = \psi_R + \psi_L^C$$

we can rewrite Lagrangians 2.8 and 2.9 as

$$\mathscr{L}_L = \frac{1}{2}m_L\bar{\phi}_1\phi_1 \qquad\qquad \mathscr{L}_R = \frac{1}{2}m_R\bar{\phi}_2\phi_2$$

While $\psi_{L,R}$ are interaction eigenstates, $\phi_{1,2}$ are mass eigenstates with eigenvalues $m_{L,R}$ respectively.

For a generic particle described by the field ψ, the more general mass term in the Lagrangian is a combination of Dirac- and Mjorana-like parts:

$$
\begin{aligned}
2\mathscr{L} &= m_D(\bar{\psi}_L\psi_R + \bar{\psi}_L^C\psi_R^C) + m_L\bar{\psi}_L\psi_R^C + m_R\bar{\psi}_L^C\psi_R + h.c. \\
&= (\bar{\psi}_L, \bar{\psi}_L^C)
\begin{pmatrix} m_L & m_D \\ m_D & m_R \end{pmatrix}
\begin{pmatrix} \psi_R^C \\ \psi_R \end{pmatrix} + h.c. \\
&= \bar{\Psi}_L M \Psi_R^C + \bar{\Psi}_R^C M \Psi_L
\end{aligned}
\tag{2.10}
$$

where the notation:

$$
M = \begin{pmatrix} m_L & m_D \\ m_D & m_L \end{pmatrix}
\qquad\qquad
\Psi_L = \begin{pmatrix} \psi_L \\ \psi_L^C \end{pmatrix} = \begin{pmatrix} \psi_L \\ (\psi_R)^C \end{pmatrix}
$$

$$
(\Psi_L)^C = \begin{pmatrix} (\psi_L)^C \\ \psi_R \end{pmatrix} = \begin{pmatrix} \psi_R^C \\ \psi_R \end{pmatrix} = \Psi_R^C
$$

have been used. If we now associate the field Ψ to the neutrino and define $\psi_L = \nu_L$ and $\psi_R^C = \nu_R^C$ the active neutrinos and $\psi_R = N_R$ and $\psi_L^C = N_L^C$ the sterile ones we get, from Eq. 2.10, the mass Lagrangian for the neutrino:

$$
\begin{aligned}
2\mathscr{L} &= m_D(\bar{\nu}_L N_R + \bar{N}_L^C \nu_R^C) + m_L\bar{\nu}_L\nu_R^C + m_R\bar{N}_L^C N_R + h.c. \\
&= (\bar{\nu}_L, \bar{N}_L^C)
\begin{pmatrix} m_L & m_D \\ m_D & m_R \end{pmatrix}
\begin{pmatrix} \nu_R^C \\ N_R \end{pmatrix} + h.c.
\end{aligned}
\tag{2.11}
$$

By diagonalizing the mass term matrix M we obtain the mass eigenstes

$$
\psi_{1L} = \cos\theta\,\psi_L - \sin\theta\,\psi_L^C \qquad \psi_{1R}^C = \cos\theta\,\psi_R^C - \sin\theta\,\psi_R
\tag{2.12}
$$

$$
\psi_{2L} = \sin\theta\,\psi_L + \cos\theta\,\psi_L^C \qquad \psi_{2R}^C = \sin\theta\,\psi_R^C + \cos\theta\,\psi_R
\tag{2.13}
$$

$$
\tag{2.14}
$$

with the rotation angle θ defined by

$$
\tan 2\theta = \frac{2m_D}{m_R - m_L}
\tag{2.15}
$$

and the eigenvalues

$$
\tilde{m}_{1,2} = \frac{1}{2}\left[(m_L + m_R) \pm \sqrt{(m_L + m_R)^2 + 4m_D^2} \right].
\tag{2.16}
$$

2.1 Neutrino mass and double beta decay

The final step to get positive values for the masses is

$$\tilde{m}_{1,2} = \epsilon_{1,2} m_{1,2} \qquad \text{with } m_{1,2} = |\tilde{m}_{1,2}| \text{ and } \epsilon_{1,2} = \{+1, -1\}.$$

Two Majorana fields[1] can be created by combining mass eigenstates

$$\phi_1 = \psi_{1L} + \epsilon_1 \psi_{1R}^C = \cos\theta(\psi_L + \epsilon_1\psi_R^C) - \sin\theta(\psi_L^C + \epsilon_1\psi_R) \qquad (2.17)$$

$$\phi_2 = \psi_{2L} + \epsilon_2 \psi_{2R}^C = \sin\theta(\psi_L + \epsilon_2\psi_R^C) + \cos\theta(\psi_L^C + \epsilon_2\psi_R) \qquad (2.18)$$

with masses $m_{1,2}$ and we can use them to rewrite the Lagrangian

$$2\mathscr{L} = m_1\bar{\phi}_1\phi_1 + m_2\bar{\phi}_2\phi_2 . \qquad (2.19)$$

The angle θ is a free paramter in the theory and represents the rotation of the mass eignestates with respect to the interaction eigenstates. Eq. 2.15 expresses its dependence on the values of Dirac and Majorana masses. The most important cases are:

- $m_L = m_R = 0$ ($\theta = 45°$) from which $m_{1,2} = m_D$ and $\epsilon_{1,2} = \pm 1$. Majorana fields are degenerate

$$\phi_1 = \frac{1}{\sqrt{2}}(\psi_L - \psi_R^C - \psi_L^C + \psi_R) = \frac{1}{\sqrt{2}}(\psi - \psi^C) \qquad (2.20)$$

$$\phi_2 = \frac{1}{\sqrt{2}}(\psi_L + \psi_R^C + \psi_L^C + \psi_R) = \frac{1}{\sqrt{2}}(\psi + \psi^C) \qquad (2.21)$$

and can be used to build the Dirac field

$$\frac{1}{\sqrt{2}}(\phi_1 + \phi_2) = \psi_L + \psi_R = \psi .$$

The corresponding mass term in the Lagrangian (considering that $\bar{\phi}_1\phi_2 + \bar{\phi}_2\phi_1 = 0$) is

$$\mathscr{L} = \frac{1}{2}m_D(\bar{\phi}_1 + \bar{\phi}_2)(\phi_1 + \phi_2) = m_D\bar{\psi}\psi .$$

Dirac neutrino is eventually a degenerate case of the more comprehensive Majorana neutrino. In the Standard Model, where the sterile component of the neutrino is completeley decoupled, the only possibility is that this mass term vanishes;

- $m_D \gg m_L, m_R$ ($\theta \simeq 45°$) the fields $\phi_{1,2}$ are very close to the previous case, and $m_{1,2} \simeq m_D$. In this case the neutrino is called *pseudo-Dirac* neutrino;

---

[1]As can be deduced from the property: $\phi_k^c = (\psi_{kL})^C + \epsilon_k\psi_{kL} = \epsilon_k(\epsilon_k\psi_{kR}^C + \psi_{kL}) = \epsilon_k\phi_k$
with $k = \{1,2\}$, $\epsilon_{1,2}$ is the CP eigenvalue of Majorana neutrino $\phi_{1,2}$

- $m_D = 0$ $(\theta = 0)$ in this case $m_{1,2} = m_{L,R}$ and $\epsilon_{1,2} = 1$ and

$$\phi_1 = \psi_L + \psi_R^C$$
$$\phi_2 = \psi_R + \psi_L^C ;$$

- $m_R \gg m_D$, $m_L = 0$ $(\theta = (m_D/m_R) \ll 1)$ from Eq. 2.16, with $\epsilon_{1,2} = \pm 1$, two eigenvalues are obtained

$$m_N \simeq \frac{m_R}{2}\left[1 + \frac{m_r^2}{m_R^2 - 2m_D^2}\right] \simeq m_R$$
$$m_\nu \simeq \frac{m_R}{2}\left[\frac{-2m_D^2}{m_R^2 - 2m_D^2}\right] \simeq \frac{m_D^2}{m_R} \ll m_N .$$

This last scenario is the so called *see-saw* model. A right-handed neutrino with a very large mass, and hence with practically no dynamics at ordinary energies, allows the left-handed neutrino to have its small mass.

2.1.3 Lepton number violation and double beta decay

The conservation of (family and total) lepton number was introduced to justify the lack of observation of phenomena that modify the number of leptons in the final state with respect to the number of leptons in the initial state. Unlike the conservation of other quantum numbers, the lepton number conservation doesn't proceed from a fundamental symmetry of the Lagrangian of the Standard Model but from an accidental symmetry, and hence a deep origin for it cannot be found in the structure of the theory. The oscillation of neutrinos is a proof that the non-vanishing mass of the neutrino leads to the violation of the conservation of family lepton number. A total lepton number violating phenomenon have never been observed until now. The introduction of the Majorana term for the neutrino mass in a Lagrangian with Dirac masses, however, makes total lepton number processes possible.

The scalar terms used to build the Lagrangian in Eq. 2.7 and the Dirac-like scalar $\bar{\psi}\psi$ behave differently under a global phase transformation. In fact

$$\bar{\psi}\psi \rightarrow (e^{-i\alpha}\bar{\psi})(e^{i\alpha}\psi) = \bar{\psi}\psi \qquad (2.22)$$

hence Dirac mass terms are invariant under global phase transformations. This corresponds to the conservation of the lepton number: in terms of quantum fields, ψ annihilates a lepton and creates an anti-lepton while $\bar{\psi}$ acts in the opposite way. When leptons described by these mass terms are involved the process does conserve the lepton

number.

On the contrary a scalar like the ones used to build the Majorana mass term transforms in the following way:

$$\bar{\psi}\psi^C \to (e^{i\alpha}\bar{\psi})(e^{-i\alpha}\psi^C) = e^{-2i\alpha}\bar{\psi}\psi^C \;. \tag{2.23}$$

This term allows transitions between initial and final states with a number of leptons that differs by two units. Adding Majorana mass terms to the Standard Model Lagrangian makes lepton number violating processes possible in the theory. On the other hand, since the lepton number is conserved in the Standard Model, the experimental observation of a process that violates the lepton number conservation would be a strong hint of the necessity of extending the model for example inserting Majorana mass terms to justify the neutrino mass. In this sense a golden process exists that many experiments in the world are looking for, because its observation would be the proof that lepton number conservation can be violated and a powerful tool for measuring the absolute scale and hierarchy of neutrino masses (oscillations provide only a measure of the differences between the masses) at the same time. This process is neutrinoless double beta decay (or $\beta\beta0\nu$ decay).

$\beta\beta0\nu$ decay is a forbidden decay channel alternative to $\beta\beta2\nu$ decay which is, on the contrary, allowed in the Standard Model. $\beta\beta2\nu$ decay is a nuclear decay that increases by two units the electric charge Z of the nucleus without changing the mass number A, hence occurring between isobaric nuclei. Weizsäcker [18] formula describes the dependence of nuclear mass on atomic number:

$$m(Z, A)|_{A=\text{const}} \propto \alpha Z + \beta Z^2 + \delta_P \tag{2.24}$$

where δ_P is called pairing energy and can be empirically parameterized as:

$$\delta_P = \begin{cases} -a_P A^{-1/2} & \text{even-even nuclei} \\ 0 & \text{even-odd or odd-even nuclei} \\ +a_P A^{-1/2} & \text{odd-odd nuclei} \end{cases}$$

with $a_P \sim 12\text{MeV}$. For nuclei with odd A Eq. 2.24 is a single parabolic curve, while even A nuclei lie on one of the two curves in which Eq. 2.24 is split by the presence of the pairing energy. As can be seen in Fig. 2.1, a even-even nucleus lying in the lower curve of the rightmost picture cannot undergo standard beta decay because the daughter nucleus, which is odd-odd, lies on the upper curve hence having a larger mass. Single beta transitions to the nearby odd-odd isobar are therefore often forbidden (in

some cases suppressed) and the only possible decay mode is the double beta decay that transforms the even-even nucleus in another even-even one lying on the same curve.
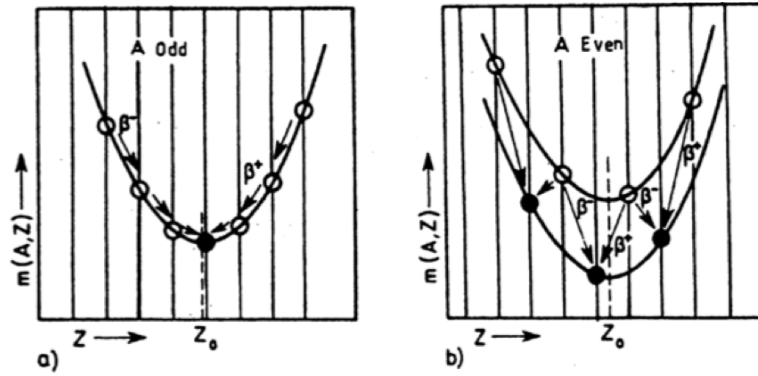
Figure 2.1: Relation between nuclear mass and atomic number, described by the Weizsäcker formula
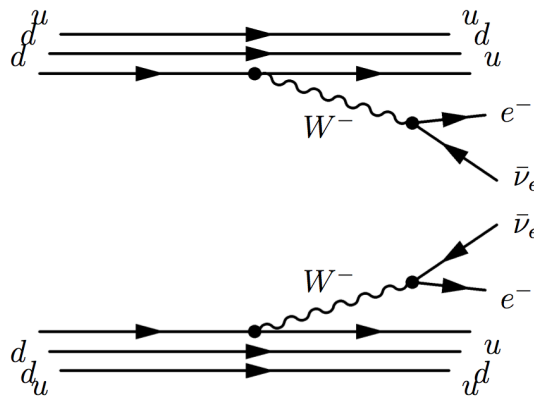
Figure 2.2: Feynman diagram of Standard Model allowed double beta decay.

By examining $\beta\beta2\nu$ decay

$$(Z, A) \rightarrow (Z + 2, A) + 2e^- + 2\bar{\nu}_e \tag{2.25}$$

Feynman diagram (Fig. 2.2) it's evident that $\beta\beta2\nu$ decay is allowed in the Standard Model, because it's simply a simultaneus beta decay of two neutrons in the nucleus, coupled by energy conservation. For the same reason, however, it is strongly suppressed:

since it contains two weak vertices, the process is second order in Fermi theory - or fourth order in GSW theory, hence the cross section is proportional to $(G_F \cos \theta_C)^{-4}$, roughly G_F^2 times smaller compared to single beta decay. $\beta\beta 2\nu$ decay can therefore be observed only for those even-even nuclei where any other decay mode is forbidden.

Nutrinoless double beta decay, on the contrary, isn't allowed in the Standard Model because two leptons are missing in the final state:

$$(Z, A) \rightarrow (Z + 2, A) + 2e^- \ . \tag{2.26}$$

Neutrinoless double beta decay can proceed through many different mechanisms; the simplest one is the exchange of a massive Majorana particle that is emitted as left-handed neutrino and absorbed like a right-handed (being massive it is not an helicity eigenstate) antinuetrino (being a Majorana particle it is identical to its antiparticle). This process is represented in the Feynman diagram of Fig. 2.3 and was firs devised by Racah in 1937.
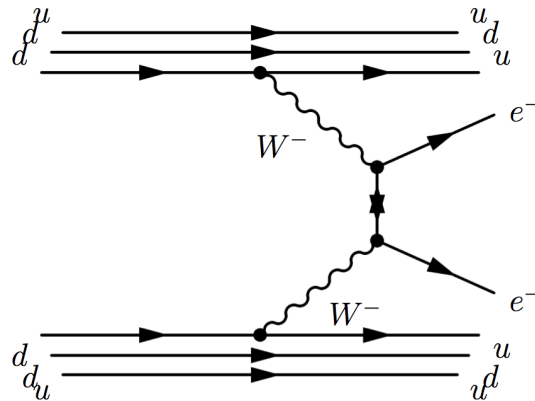
Figure 2.3: Feynman diagram of Standard Model forbidden neutrinoless double beta decay.

An important consequence of neutrinoless double beta decay, however, is that, no matter which is the mechanism that actually drives the process, its existence would imply the existence of a Majorana neutrino mass term[19]. This is shown in Fig. 2.4 where the internal unknown mechanism of double beta decay is represented as a "black-box". In the framework of a general gauge theory, the process can be manipulated to become the coupling between an antineutrino and a neutrino, i.e. a Majorana mass term like the ones in Eq. 2.8 an Eq. 2.9.
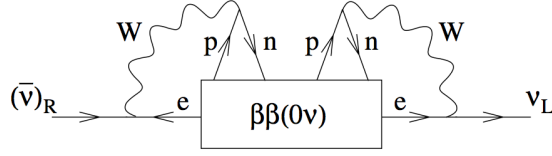
Figure 2.4: Feynman diagram that shows how the existence of neutrinoless double beta decay implies the existence of a Majorana mass term, by coupling a neutrino and its antiparticle.

The rate for neutrinoless double beta decay can be written as[20]

$$\left(T_{1/2}^{0\nu}\right)^{-1} = G_{0\nu}\,|M_{0\nu}|^2\,\frac{|\langle m_{\beta\beta}\rangle|^2}{m_e^2} \tag{2.27}$$

where:

- $G_{0\nu}$ is a phase space factor, it depends on the nucleus that undergoes $\beta\beta0\nu$ decay but can be calculated exacly;

- $M_{0\nu}$ is the nuclear matrix element (NME) for the $\beta\beta0\nu$ transition; it also depends on the nucleus, but its value must be calculated starting from a specific nuclear model and it is the main source of theoretical uncertainty. Nuclear matrix elements depend on the structure of the parent and daughter nuclei, as well as on intermediate ones; their calculation requires a detailed model for the distribution and interactions of nucleons inside the nucleus, and the solution of a multi-body problem that cannot be addressed analitically but requires numericals computations where approximations must be introduced. For this reason the spread in the results obtained by various groups is still rather large, with the values for the nuclear matrix of the same nucleus typically lying within a factor two (Fig. 2.5);

- $m_{\beta\beta}$ is called effective Majorana mass and depends on single neutrino mass eigenvalues and mixing matrix parameters:

$$m_{\beta\beta} = \left|\sum_{j=1}^{3} U_{ej}^2 m_j\right| = \left|\sum_{j=1}^{3} |U_{ej}|^2\, e^{i\phi_j} m_j\right| . \tag{2.28}$$

In contrast to single beta decay, the double beta decay rate is sensitive also to the two Majorana phases introduced in Eq. 2.3 and to the neutrino mass ordering (mass hierarchy), i.e. the fact that the smaller squared mass difference is between

the two lightest (normal hierarchy) or haviest (inverted hierarchy) neutrinos (see Fig. 2.7). Since the U_{ei} and the two squared mass differences are known from oscillation experiments, $m_{\beta\beta}$ can be written in terms of only three parameters ($m_{\beta\beta}$ and the two Majorana phases) obtaining the result shown in Fig. 2.6; the allowed values of $m_{\beta\beta}$ are plotted as a function of the lightest neutrino mass, both for normal and inverted hierarchy.
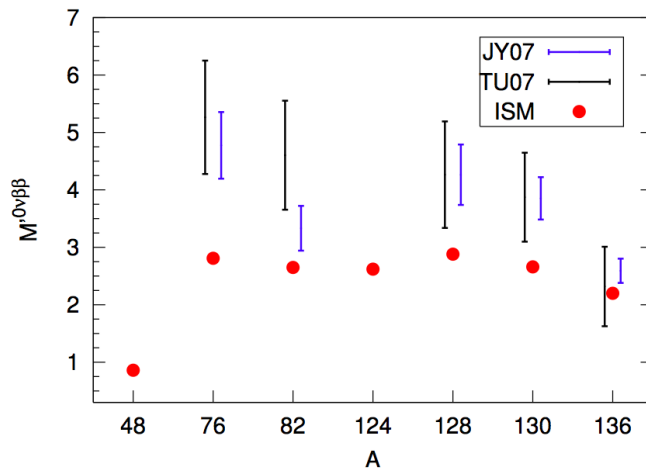
Figure 2.5: Values of nuclear matrix elements[21] for some $\beta\beta0\nu$ emitters calculated using QRPA (black and blue bars) and NSM (red dots) methods. In QRPA calculations the choice of some parameters of the model leads to uncertainties that are represented by the bars.

2.1.4 CUORE approach to double beta decay

From the experimental point of view, the search for double beta decay consists in the search for a signature of the occurrence of the process and the measurement of the half life of the decaying nucleus, from which (see Eq. 2.27) the $m_{\beta\beta}$ parameter can be derived. The total amount of energy released in a double beta decay, the Q-value of the process $Q_{\beta\beta}$, corresponds to the difference between the mass of the parent atom ($M_{A,Z}$) and the sum of the masses of the particles in the final state, i.e. the daughter atom ($M_{A,Z+2}$) and two electrons (neutrino masses are obviously neglected):

$$Q_{\beta\beta} = M_{A,Z} - (M_{A,Z+2} + 2m_e) . \tag{2.29}$$
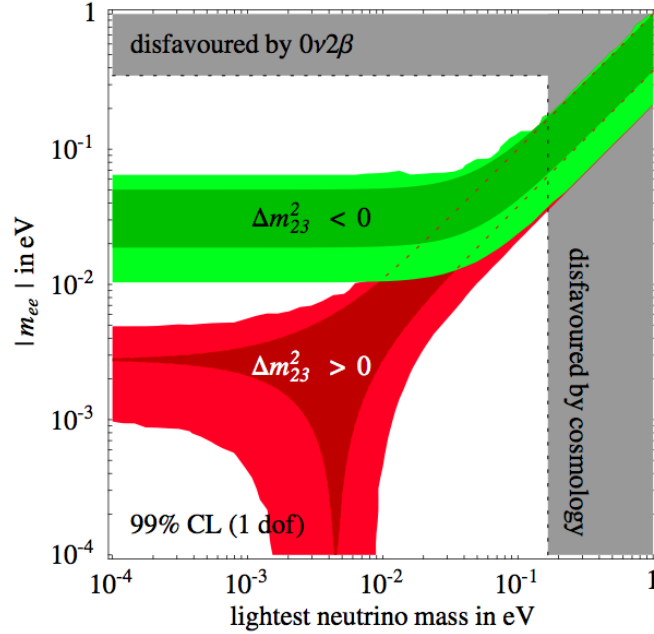
Figure 2.6: Allowed regions for $m_{\beta\beta}$ as a function of the lighest neutrino mass. The gray bands are the regions already excluded by double beta decay limits or cosmological observations. The green band corresponds to the inverted hierarchy while the red one to normal hierarchy. The region where green and red bands overlap is called degenerate hierarchy. In this region double beta decay observation wouldn't be conclusive about the hierarchy of neutrino masses. In both green and red bands the darker regions correspond to the allowed regions that would be obtained if the mixing matrix parameters and squared mass differences were known with infinite precision. In this case tho only source of theoretical uncertainty would be the Majorana phases.

In $\beta\beta2\nu$ decay this energy is shared among the two neutrinos and the two electrons. Since the probability of a neutrino interacting in the detector is completely negligible, only the fraction of the energy carried by the elctrons can be detected. A calorimetric detector, i.e. a detector designed to perform a precise measurement of the total amount of energy that is carried by the interacting particle, like CUORE can measure with high accuracy the kinetic energy of the electrons. In $\beta\beta2\nu$ decay the corresponding energy spectrum has a continuous shape due to the loss of the undetected neutrinos energy. If $\beta\beta0\nu$ decay occurs, on the contrary, no neutrinos are emitted and the sum of the kinetic energies of the two electrons must equal the Q-value of the decay (the energy of the daughter nucleus is, of course, negligible and anyway it's practically always detected). The signature of the neutrinoless double beta decay in a bolometer is therefore a monochromatic peak in the energy spectrum, at $Q_{\beta\beta}$ (Fig. 2.8).
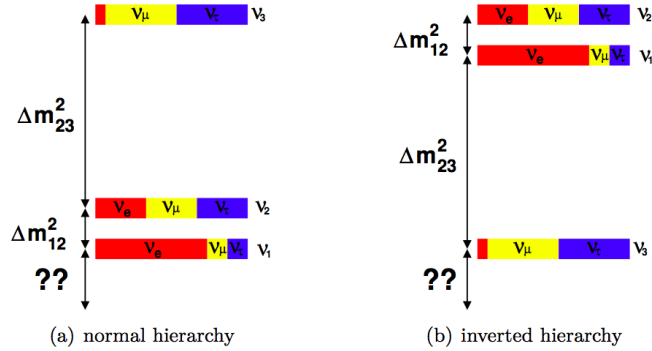
Figure 2.7: Graphical representation of neutrino mass hierarchies. In (a) the smaller squared mass difference (also known as solar mass difference because it is measured in solar neutrino experiments), Δm_{12}^2 is between the two lighest neutrinos; in (b) it lies between the two heaviest ones. It's worth noting that the absolute mass scale, i.e. the mass of the lighest neutrino, is still unknown and could, in principle, be vanishing.
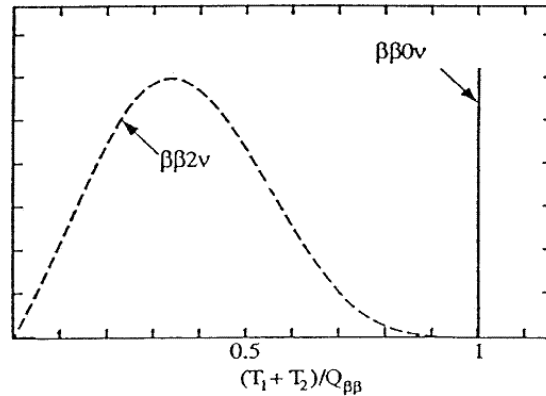
Figure 2.8: Spectrum of the sum energy of the electrons emitted in double beta decay. $\beta\beta2\nu$ spectrum is continuous because part of the Q-value energy is carried by the two undetected neutrinos. $\beta\beta0\nu$ spectrum is a monochromatic peak at the end-point of the spectrum: no undetected particle is emitted in the process and the bolometer collects all the kinetic energy of the particles in the final state.

It's worth noting here that the spectrum represented in Fig. 2.8 has the ideal shape that would be obtained by a detector with infinite energy resolution. The real case is a convolution of that same spectrum with the response function of the bolometer, usually a gaussian. The main consequence is that the sharp peak broadens into a gaussian width

a with given by the energy resolution of the detectors. The height of the peak decreases correspondingly because the same number of events is spread in a wider energy range. Eventually, with a bad energy resolution, the events that populate the $\beta\beta 2\nu$ spectrum can easily overlap with the ones from the $\beta\beta 0\nu$ peak strongly reducing the possibility of identify the peak itself (in Section 3.2 this problem is examined in more depth).

The sensitivity of an experiment is defined as the half-life corresponding to the minimum number of signal events that can be observed above the background at a given statistical significance. For experiments where the background counts scale as the mass of the detector (see Chapter 3) the sensitivity can be expressed as

$$S^{0\nu}(\text{C.L.}) = \frac{\ln 2}{\text{C.L.}/0.68} \epsilon N_a \frac{a}{A} \sqrt{\frac{M \cdot t}{b \cdot \Delta E}} \tag{2.30}$$

where C.L. is the statistical significance (or confidence level), ϵ is the detection efficiency, N_a is the Avogadro number, a is the isotopic abundance of the double beta emitter, A is the molecular weight, M the total detector mass, t the live time of the experiment, ΔE is the resolution and b the background expressed in counts/(keV $\cdot$ kg $\cdot$ year). In order to compare the discovery potential of experiments using different isotopes it is convenient to define the nuclear factor of merit F_N

$$F_N = G_{0\nu} \left| M_{0\nu} \right|^2 \tag{2.31}$$

which has dimension years^{-1}. Using Eq. 2.31 and Eq. 2.30 in place of the half life in Eq. 2.27 the effective Majorana mass that an experiment is able to measure is expressed as:

$$m_{\beta\beta} = \frac{m_e}{\sqrt{S^{0\nu} \cdot F_N}} \tag{2.32}$$

In Tab. 2.1 the most used double beta emitters are reported with nuclear factor of merits, Q-values, natural isotopic abundances and present limits for the $\beta\beta 0\nu$ half life.

Isotopes with higher Q-value are usually better candidates for different reasons: at energies above the highest natural γ radioactivity peak (2615keV of ^{208}Tl) the radioactive background is usually much lower and usually dominated by high energy alpha decays; the phase space term $G_{0\nu}$ is proportional to the fifth power of the Q-value ($G_{0\nu} \sim Q^5$) [29]; the fraction of $\beta\beta 2\nu$ decay events that falls in the region of $\beta\beta 0\nu$ (for a given energy resolution) scales as $1/Q^5$ [30].

Parent isotope	$T_{1/2}^{0\nu}$ [y]	F_N [y^{-1}]	$Q_{\beta\beta}$ [keV]	η [%]	Reference
^{48}Ca	$> 1.4 \times 10^{22}$	0.54×10^{-13}	4271	0.19	[22]
^{76}Ge	$> 1.9 \times 10^{25}$	0.73×10^{-13}	2039	7.4	[23]
^{82}Se	$> 1 \times 10^{23}$	1.7×10^{-13}	2995	8.7	[24]
^{100}Mo	$> 4.6 \times 10^{23}$	5.0×10^{-13}	3034	9.6	[24]
^{116}Cd	$> 1.7 \times 10^{23}$	1.3×10^{-13}	2902	7.5	[25]
^{130}Te	$> 3.0 \times 10^{24}$	4.2×10^{-13}	2527	34	[26]
^{136}Xe	$> 1.2 \times 10^{24}$	0.28×10^{-13}	2479	8.9	[27]
^{150}Nd	$> 1.8 \times 10^{22}$	57×10^{-13}	3367	5.6	[28]

Table 2.1: List of double beta decay candidates presently considered for the search for neutrinoless double beta decay.

2.2 Dark matter

The direct detection of dark matter candidates represents one of the main goals of the rare events physics in these years. A class of possible candidates to dark matter particles, the so-called WIMPs (*Weak Interacting Massive Particles*), are heavy particle that are supposed to interact with ordinary matter only through gravity and weak interactions, with tiny cross sections. The direct detection of these particles consists in the observation of the effects of the interaction with the matter that composes the detector. On the contrary, with indirect detection we usually refer to the detection of the products of phenomena involving the dark matter, like decay or interaction with the matter in environments different from the detector. Since the elementary forces to which WIMPs are subject are the same as neutrinos, also their detection mechanisms are likely to be similar. The technique that is considered the most promising is, in fact, the scattering of WIMPs on target nuclei in detectors that are sensitive to nuclear recoils. For this reason CUORE bolometers can be easily considered potentially sensitive also to dark matter interactions [31].

Unlike other bolometric detectors, TeO$_2$ bolometers are presently not able to discriminate energy released by a nuclear recoil (like the one induced by a WIMP or neutrino elastic scattering) from the energy released by beta or γ radiation; therefore, the latter can easily be a source of background. Nevertheless, the high mass and low background

achievable with CUORE detectors make it possible to search for an annual modulation of the counting rate in the energy region where WIMPs interactions are expected to give a signal. As will be also explained in Section 3.3, CUORE background at low energy (lower than about 25keV) is expected to be lower than CCVR2 background. As will be done in Chapter 4, a conservative estimation of the sensitivity of CUORE to the WIMP signal can be made assuming a background equal to the one measred in CCVR2 and an energy threshold of 3keV on all detectors.

By performing toy Montecarlo simulations of background and signal and including the dependence of the interaction rate on the time of the year, the sensitivity of CUORE (and CUORE-0, the presently running first tower of CUORE) can be calculated as a function of the WIMP mass. In Fig. 2.9 this sensitivity is plotted and compared to the one of other dark matter experiments.
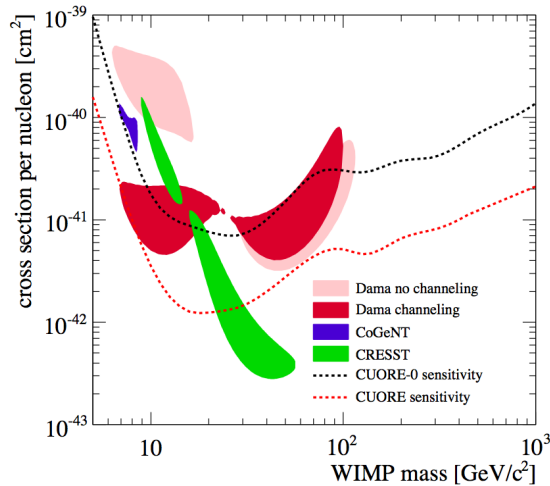
Figure 2.9: 90% Sensitivity of CUORE (5 years) and CUORE-0 (3 years) to WIMPs detection as a function of WIMP mass and interaction cross section. Evidences of DAMA-3σ, CoGeNT-90% and CRESST-2σ are reported for comparison.

2.3   Coherent scattering and supernova neutrinos

The theoretical basis of the main physics goal of this work is presented in this section: the known physics of core collapse supernovae is described along with the physics of the interaction mechanism that is foreseen to be used for the neutrino detection.

2.3.1   Core collapse supernovae

Supernovae [32] are powerful explosions which terminate the life of some stars of large mass. Tipically, some solar masses are ejected in the interstellar space with a kinetic energy of the order of 10^{51}erg and a similar energy is emitted in the form of electromagnetic radiation. The ejecta contain heavy elements that are produced during the explosion. Some supernovae produce a compact remnant, a neutron star or a black hole, depending on the star original mass, which may be observed. Many galactic supernovae have been observed in the history and, in recent times, supernovae in nearby galaxies have been also studied because their light emission is comparable to that of the an entire galaxy. Supernova SN1987A, which occurred on 23 February 1987 in the Large Magellanic Cloud, is the best studied of all SNe (see [33, 34, 35, 36]) and is the only one which was detected also through its neutrino burst ([37, 38, 39]).

Supernovae are historically divided in two types (see Fig. 2.10) characterized by their spectroscopic characteristics near the maximum luminosity and by the properties of the light curve, which depends on the composition of the envelop of the progenitor star.
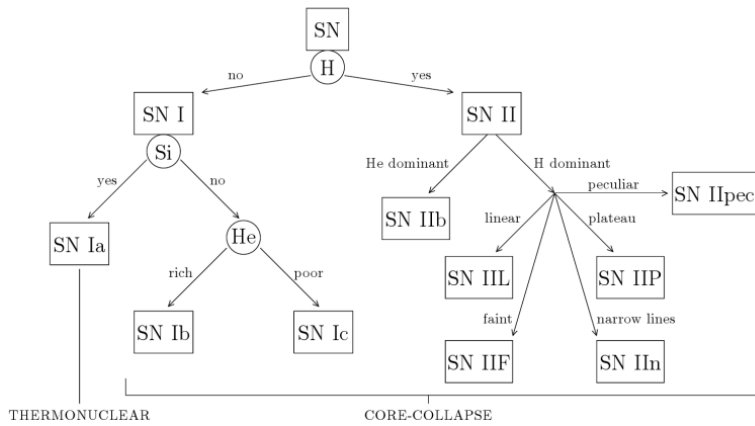
Figure 2.10: Scheme of the historical classification of supernovae and origin.

Type I supernovae are characterized by the absence of hydrogen lines in the emitted radiation, while type II supernovae show the hidrogen lines. However, the most important physical characteristic is the mechanism that generates the supernova, which distiguishes SNe of type Ia from all other types, Ib, Ic and II. This difference becomes noticeable in the light spectrum some months after maximum luminsity, when the ejecta

become optically thin and the innermost regions become visible: the spectrum of SNe Ia is dominated by Fe emission lines, whereas SNe Ib, Ic and II show O and C emission lines.

Type Ia SNe are thought to be generated by carbon-oxygen white dwarfs (stars which ended the thermonuclear fuel burning but with a mass below the Chandrasekhar limit, and thus not collapsing because of the pressure of degenerate electrons) that have a close companion star from which the white dwarf can accrate mass.

From the point of view of neutrino physics, type Ib, Ic and II SNe are much more interesting than type Ia SNe because they produce a huge flux of neutrinos of all types. These SNe are generated by the collapse of the core of massive stars ($M \gtrsim 8M_\odot$), which leaves a compact remnant. During the few seconds following the collapse, the compact remnant is very hot and neutrinos of all types are copiously produced. Since the remnant and the surrounding envelop are optically thick, about 99% of the gravitational binding energy liberated by the collapse (about 3×10^{53}erg) is carried away by neutrinos. The average energy of the emitted neutrinos is of the order of 10MeV (with a dependence on the neutrino flavor) and their number is about 10^{58}, one order of magnituuularger than the lepton number of the collapsed core.
The classification of core collapse SNe in type Ib, Ic and subtypes of II is based on the size and composition of the collapsing star envelop that leads to different behaviors of the light emission both in terms of spectral characteristics and time evolution. The neutrino emission, however, is quite independent on the characteristics of the light emission because the latter depends only on the features of the envelope which plays no role in the collapse of the core and neutrino production.

Collapse dynamics

Core collapse supernovae are the final explosion of single stars with mass between about 8-9 and 40-60 solar masses (Fig. 2.11). The explosion is due to the shock wave created when the core collapses to a proto-neutron star, which eject the stellar envelope. Stars with a mass in excess of about 10 solar masses are thought to undergo all the stages of nuclear fusion of hydrogen, helium, carbon, oxygen, neon, silicon, until the star has an onion-like structure shown in Fig. 2.12, with an iron core surrounded by shells composed of elements with decreasing atomic mass. At this point the iron core has a mass of about 1 solar mass, a radius of a few thousand kilometers, a central density of about 10^{10}g cm^{-3}, a central temperature of about 1Mev, and its weight is sustained by the pressure of degenerate relativistic electrons. Since iron is the most tightly bound nucleus, there remains no thermonuclear fuel to burn. In the very hot core, whose temperature and density is continuously increased by the iron falling from outer shells and contraction,
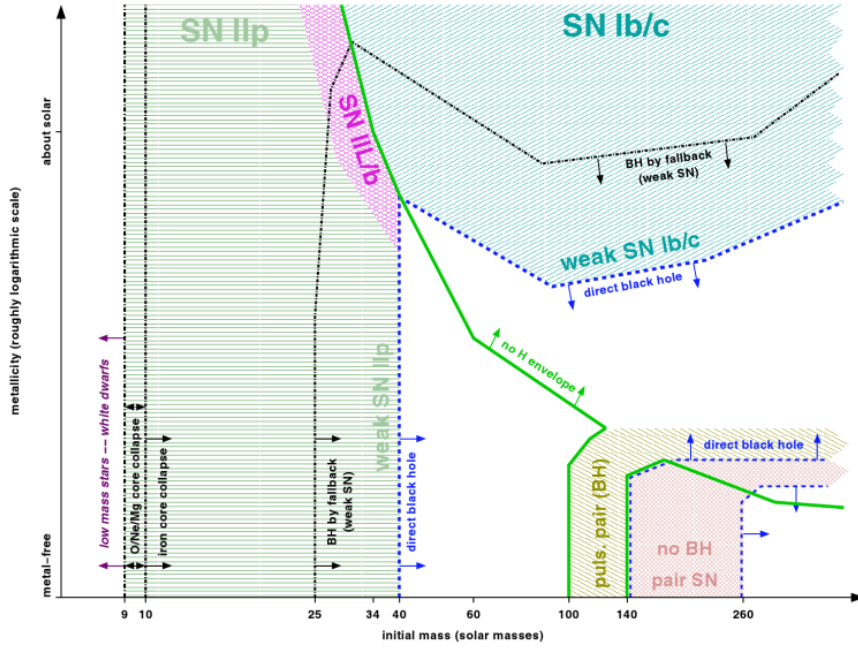
Figure 2.11: Remnants of massive single stars as a function of initial mass (x axis) and initial metallicity (y axis).

iron undergoes photodissociation through the process

$$\gamma +^{56} Fe \rightarrow 13\alpha + 4n \ . \tag{2.33}$$

Electron capture on nuclei and free protons

$$e^- + (Z, A) \rightarrow (Z - 1, A) + \nu_e \tag{2.34}$$

$$e^- + p \rightarrow n + \nu_e \tag{2.35}$$
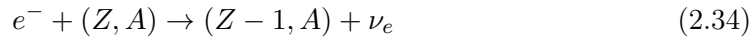
also occurs, favored by the high electron Fermi energy.

All the previous reactions reduce both the number and the pressure of the electrons by removing kinetic energy (the neutrino emission carries away about 10^{51}erg in less than 10ms), thus reducing the Chandrasekhar mass, until it becomes smaller than the core mass. At this moment the pressure of degenerate electrons can no longer sustain the weight of the core and the collapse commences. As the density and temperature increas,
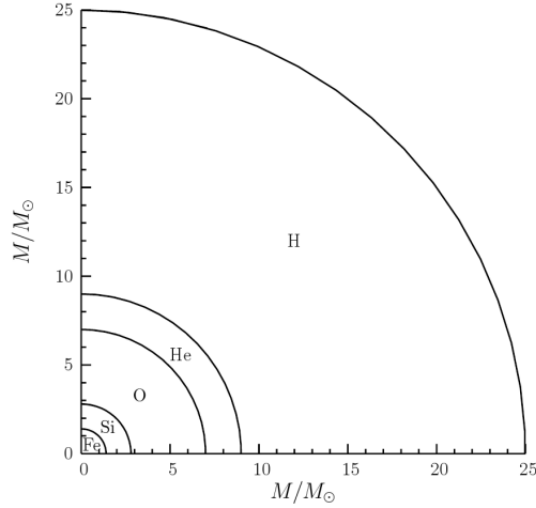
Figure 2.12: Onion-like interior structure of a typical star with mass in excess of 10 solar masses just before the collapse. Each shell can contain small quantities of elements with similar atomic weight.

the processes in Eq. 2.33, Eq. 2.34 and Eq. 2.35 proceed faster, lowering further the electron pressure and accelerating the collapse. The collapse of the core produces a neutron star and the huge liberated gravitational energy ($\sim 3 \times 10^{53}$erg) is released mainly as a flux of neutrinos, with a small fraction as electromagnetic radiation ($\sim 0.01\%$) and kinetic energy of the ejecta ($\sim 1\%$). Let's examine in more detail the mechanism of formation of the neutron star, neutrino production and supernova explosion. When, during the contraction, the inner part of the core reaches a density of about 3×10^{11}g cm^{-3}, the neutrinos produced by processes Eq. 2.34 and Eq. 2.35 become trapped in the collapsing material because their mean free path becomes smaller than the core dimension. From this point the collapse is adiabatic because the neutrinos cannot remove energy nor lepton number from the system anymore.

After about one second from the start of instability the density of the inner core reaches the density of nuclear matter, about 10^{14}g cm^{-3}, and the pressure of degenerate nonrelativistic nucleons abruptly stops the collapse. The inner core settles into hydrostatic equilibrium, forming a proto-neutron star with a radius of about 10km, while a supersonic shock wave caused by the halting and rebound of the inner core forms at its surface. The shock propagates outward through the outer iron core, which is still collapsing, with an initial velocity of the order of 100km msec^{-1}. The gas that is infalling at a velocity near free-fall is abruptly decelerated within the shock and start

falling again, much more slowly, on the surface of the proto-neutron star, accreting it. In this phase the proto-neutron star develops a inner core with the density of nuclear matter and a mantle, whose density decreases from the nuclear density down to 10^9g cm^{-3} proceeding towards the surface (whose radius is about 100km), where the shock wave propagates.

As the shock propagates through the infalling matter of the mantle, its energy is dissipated by the photodissociation of nuclei into protons and neutrons. Thus, the material behind the shock wave is mainly composed by free nucleons. Free protons have a high electron capture rate, leading to the transformation of most of them into neutrons, with a huge production of electron neutrinos. This neutrinos pile up behind the shock (which is still dense and opaque to them) until the shock reaches a zone with density lower than about 10^{11}g cm^{-3} (*shock breakout*). This happens few milliseconds after the bounce and the electrons neutrinos that piled up behind the shock are suddenly released (in a few milliseconds long burst). This first neutrino emission is usually called *prompt electron neutrino burst* or *neutronization burst* or *breakout pulse*. The neutronizatino burst carries away some 10^{51}erg in a few milliseconds. In spite of its name, it is too short to significantly reduce the lepton number of the proto-neutron star whose inner part is still opaque to neutrinos and thus not neutronized yet.

The energy loss due to photodissociation of the nuclei and neutrino emission weakens the shock. If the precursor star is small enough (less than about 10 solar masses, but the exact conditions that lead to this scenario are still controversial) the so-called *prompt SN explosion* scenario is tought to describe what happens next: the shock wave, although weakened, reaches the surface of the core and is able to expel the envelope of the star generating the explosion on a time scale of the order of 100ms. If, on the contrary, the core is too large, the shock loses all its energy and stalls about 100ms after the bounce, at a distance of about 200-300km from the core, before reaching the outer layers of the star. The fate of the remnant, in this case, depends on the amount of matter that falls on the proto-neutron star. If too much matter falls in the core, the nucleon degeneracy pressure is not enough to maintain the stability of the object that undergoes a further collapse into a black hole, presumably without a supernova explosion. If, on the contrary, a mechanism exists that is able to revive the shock quickly enough, the supernova explodes and the proto-neutron star begins to cool down. The mechanism which is currently thought to be able to revive the shock is the energy deposition by the huge neutrino flux produced thermally in the proto-neutron star ([40, 41]). It has recently been realized that the shock revival is helped by convection behind the shock, which can lead to an asymmetric explosion ([42]). Also acoustic power generated by oscillations of the accreting proto-neutron star may help the shock revival ([43]).

If the shock is revived, a so-called *delayed* supernova explosion is produced on a time scale of the order of 0.5s after the bounce.

Neutrinos of all flavors are produced in the hot core of the proto-neutron star ([44]), which has, after the adiabatic collapse, a temperature of about 40MeV, through different processes:

- electron-positron pair annihilation

$$e^- + e^+ \rightarrow \nu + \bar{\nu} \,; \tag{2.36}$$

- electron-nucleon bremsstrahlung

$$e^{\pm} + N \rightarrow e^{\pm} + N + \nu + \bar{\nu} \,; \tag{2.37}$$

- nucleon-nucleon bremsstrahlung

$$N + N \rightarrow N + N + \nu + \bar{\nu} \,; \tag{2.38}$$

- plasmon decay

$$\gamma \rightarrow \nu\bar{\nu} \,; \tag{2.39}$$

- photoannihilation

$$\gamma + e^{\pm} \rightarrow e^{\pm} + \nu + \bar{\nu} \,. \tag{2.40}$$

Electron neutrinos are also produced by the electron capture process in Eq. 2.35, and electron antineutrinos are produced by positron capture on neutrons ($e^+ + n \rightarrow p + \bar{\nu}_e$), both with much smaller rates. In spite of their weak interactions, these neutrinos are trapped in the SN core because of the very high matter density. Neutrinos can free stream out of the mantle of a proto-neutron star only at a distance from the center where the matter density is low enough (of the order of $10^{11}\mathrm{g\,cm^{-3}}$) so that the neutrino mean free path is larger than the radius of the core. The sphere from which neutrinos stream out freely is called *neutrinosphere*, and it lies within the mantle of the proto-neutron star. Since neutrino interactions depend on flavor and energy, there are different energy-dependent neutrinospheres for different flavor neutrinos. More precisely, since the medium is composed of ordinary matter, i.e. protons, neutrons and electrons, and the neutrino energy is not large enough to create muons and taus, the electron neutrinos and antineutrinos can interact with the medium through both charged-current and neutral-current weak processes, whereas the neutrinos ν_μ, $\bar{\nu}_\mu$, ν_τ, $\bar{\nu}_\tau$ can interact only through neutral-current weak processes, which are flavor independent. Therefore,

there are three neutrinospheres: one for ν_e, one for $\bar{\nu}_e$ and one for ν_μ, $\bar{\nu}_\mu$, ν_τ, $\bar{\nu}_\tau$ (that, from now on, will be denoted collectively as $\bar{\nu}_x$). Each neutrinosphere emits a black-body thermal flux of neutrinos at the considered energy. The estimated radii of the neutrinospheres lie between about 50 and 100km. The opacities of ν_e and $\bar{\nu}_e$ are dominated, respectively, by the charged-current reactions

$$\nu_e + n \rightarrow p + e^- \; , \tag{2.41}$$

$$\bar{\nu}_e + p \rightarrow n + e^+ \; . \tag{2.42}$$

Since the mantle of the proto-neutron star is neutron-reach (a partial neutronization occurred during the first non-adiabatic phase of the contraction), the opacity of ν_e of a given energy is larger than the opacity of $\bar{\nu}_e$ of the same energy, and the corresponding ν_e neutrinospehere has a larger radius than the $\bar{\nu}_e$ one. Therefore, $\bar{\nu}_e$'s are on average emitted by a deeper and hotter layer than ν_e's, leading to a $\bar{\nu}_e$ mean energy larger than the ν_e mean energy. For similar reasons the neutrinosphere of $\bar{\nu}_x$, whose interaction rate in the medium is the smallest one, has an even smaller radius and the mean energy of $\bar{\nu}_x$ is the largest among the three spectra. An estimation of the mean energies of the spectra, as well as the time evolution of the neutrino luminosity, is given by numercal simulations. The time integrated average energies are roughly

$$\langle E_{\nu_e} \rangle \simeq 10 \text{MeV} \; , \qquad \langle E_{\bar{\nu}_e} \rangle \simeq 15 \text{MeV} \; , \qquad \langle E_{\nu_x} \rangle \simeq 20 \text{MeV} \; . \tag{2.43}$$

The average energies and spectral shapes of neutrino emissions are calculated with numerical simulations by many groups and are affected by large uncertainties. In this work a simplified, but very diffuse in literature, approach from [45, 1] has been considered, with Boltzmann spectra at temperatures of $k_B T = 3.5$, 5 and 8 MeV for the ν_e, $\bar{\nu}_e$ and $\bar{\nu}_x$ respectively. An equal partition of the energy of a standard core-collapse supernova (3×10^{53} ergs) among the three components (ν_e, $\bar{\nu}_e$, ν_x) is assumed leading to a total number of radiated neutrinos of $N_{\nu_e} = 3.0 \times 10^{57}$, $N_{\bar{\nu}_e} = 2.1 \times 10^{57}$ and $N_{\nu_x} = 5.2 \times 10^{57}$. The spectral shape ($E$ beeing the neutrino energy and $i = \nu_e, \bar{\nu}_e, \nu_x$) is

$$\tilde{\phi}_i(E) = \frac{N_i}{2T_i^3} E^2 \exp\left(-\frac{E}{T_i}\right) \tag{2.44}$$

and the corresponding spectra are shown in Fig. 2.13 (for a distance from the supernova of 8.5kPc).

This simplified approach contains some important uncertainties, in particular about the validity of the equal partition of energy assumption and the temperature parameter
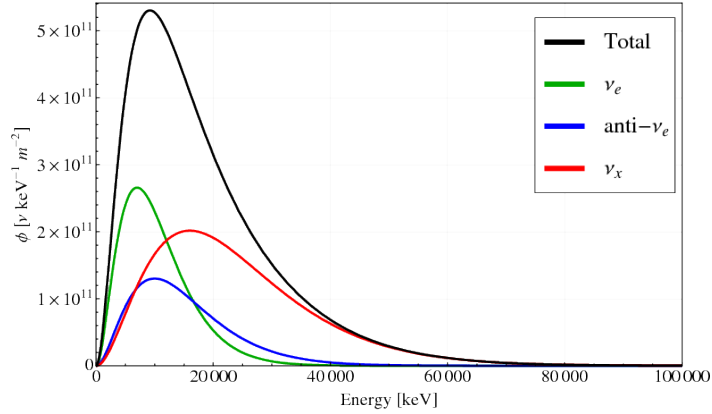
Figure 2.13: Time integrated neutrino spectra for a supernova distance of 8.5kPc. The Boltzmann distribution characteristic temperatures are $k_B T = 3.5$, 5 and 8MeV for electron neutrinos, electron antineutrinos and all other species respectively.

of the ν_x spectrum (whose measure is indeed an important goal of elastic-scattering detectors). Nevertheless, this simple model should provide order-of-magnitude estimates of neutrino fluxes to be used in the calculation of an experiment sensitivity.

Since the approximation that leads to energy spectra with the shape of Boltzman distributions actually consists in neglecting all neutrino production mechanisms but the cooling phase of the neutron star after the supernova explosion, the same approximation can be used to infer the time distribution of the events expected in the detector. The numerical simulations that are able to describe the supernova explosion (see Fig. 2.14 from [32]) predict fairly complicated time profiles for the neutrino emission. As already described, neutrinos are emitted in at least three different phases:

- an early few milliseconds long capture burst produced during the core collapse before the density reaches the critical point where the matter becomes opaque to neutrinos; these neutrinos are responsible for the removal of energy and lepton number from the core, accelerating the collapse;

- the neutronization burst, again few milliseconds long, emitted shortly after the bounce of the core, when the shock reaches the lower density external layers of the proto-neutron star mantle;

- the huge thermal emission of neutrinos during the new-born neutron star cooling; this phase lasts about 10 seconds.
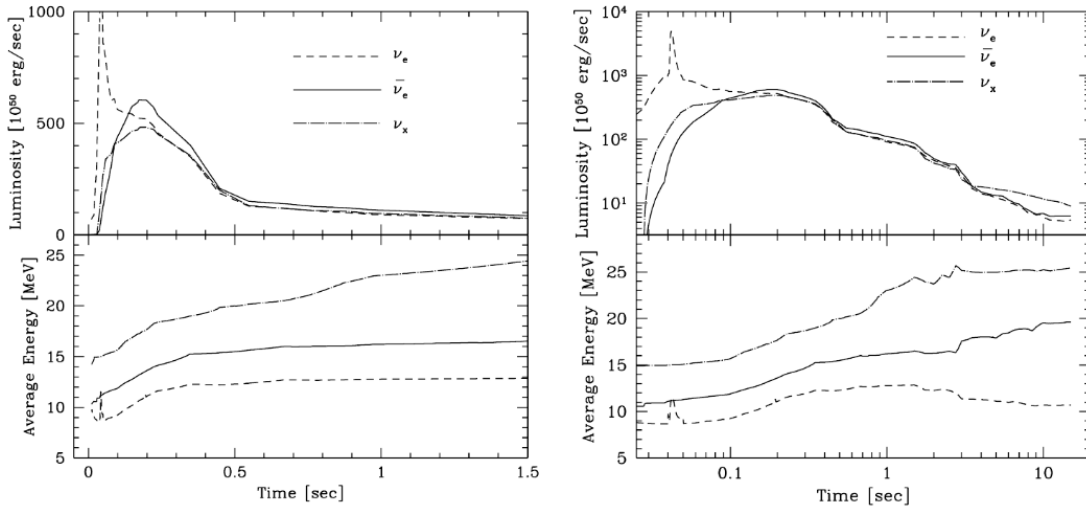
Figure 2.14: Time evolution of neutrino luminosity and average energy obtained with the numerisal SN model in [46]. The time starts at the onset of collapse. The left panel shows the early phase in a linear time coordinate. The right panel shows the time evolution until about 10s fater the onset of collapse using a logarithmic time coordinate. The dashed lines are for ν_e, the solid lines for $\overline{\nu}_e$ and the dot-dashed lines for ν_x. The neutronization burst is visible as a peak of luminosity and energy of electron neutrinos, which happens 40-50ms after the onset of collapse.

The neutrinos emitted during the first two bursts are almost exclusively electron neutrinos produced by electron capture processes in the very dense and hot matter of the proto-neutron star. The luminosity of these bursts is very high ($\sim 10^{53}$erg s^{-1} for the capture burst, $\sim 6 \times 10^{51}$erg s^{-1} for the neutronization burst), but they are too short to remove a consistent fraction of the gravitational energy of the collapsing system. Only about 10^{51}erg are carried away by these neutrinos, only about 1% of the total energy. Since the number of interactions that are expected to be detected in CUORE is of the order of few tens (see Chapter 4), the small fraction of events produced by these neutrinos can be safely neglected.

Therefore the only remaining contribution come from the thermal flux of the cooling phase. Simulations show fairly complicated profiles. Looking at the right panel of Fig. 2.14, however, it turns out that, starting from few hundreds of milliseconds after the onset of the collapse, all three neutrino species have a very similar behavior. If the oscillatory behavior (simulations show that it can depend on the initial structure of the star), that could hardly be observed due to statistical fluctuations of the number of events per time unit in the detector, is averaged out, the luminosity decays with an ex-

ponential law characterized by a time constant of ~ 3.5s ([47, 48]). This approximation (aswell as the one on the energy spectra) will be used in all the discovery potential and statistical significance calculations in this work, and this choice seems to be justified by the fact that the number of events expected in almost all the realistic cases is probably too small to perform a sensible observation of any other feature. If, in the case of a true observation, the number of events would turn out to be larger than expected, some additional information could be extracted by comparing the data with more complete and articulated models. This possibility is briefly discussed in Section 6.1.

Supernova spatial probability

A brief discussion over the probability of occurence of a galactic core collapse supernova as a function of its distance from the Earth can help in understanding some of the choices made in this work. Only galactic events are considered because, as will be shown in Chapter 4, the capabilities of CUORE will hardly extend beyond its limits. From [49] and contained references we know that the distribution of probability of supernova occurrence within the galaxy is strictly related to the distribution of supernovae precursors and can be extrapolated from the observation of the distribution of te phenomena that are known to be the remnants of a supernova explosion, like SNR nebulae, pulsar identified as rotating neutron stars, galactic CR sources, interstellar magnetic fields and regions of large star formation rate that can be associated to the matter expelled during the explosion. A rough approximation of the radial distribution of pre-SN stars is

$$\frac{\mathrm{d}\zeta(r)}{\mathrm{d}r} = f\delta(r) + (1-f)r\frac{e^{-\frac{r}{a}}}{a^2} \tag{2.45}$$

where $a \sim 3$kPc. In Eq. 2.45, r is the distance from the galactic center. The distribution of supernovae precursors in the galactic volume is reasonably well described, but the number of supernovae that could occur in the central part of the galaxy is much harder to evaluate and depends on the structure and distribution of the matter in the center. The parameter f, that is expected to range from 0 to about 50% depending on the model, accounts for the possibility that the galactic center contains a higher density of pre-SN objects.

In order to evaluate the distribution of pre-SN stars as a function of the more usefull distance from the Earth, L, Eq. 2.45 must be integrated performing a variable change, $r = \sqrt{L^2 + R^2 - 2LR\cos\theta}$, with $R = 8.5$kPc is the distance of the galactic center from the Earth:

$$\frac{\mathrm{d}\zeta(L)}{\mathrm{d}L} = L\int_0^{2\pi}\mathrm{d}\theta\frac{e^{-\frac{r(L,\theta)}{a}}\mathrm{d}\theta}{2\pi a^2} \ . \tag{2.46}$$

Here f was assumed equal to zero; the corresponding distribution is depicted in Fig. 2.15, taken from [49].
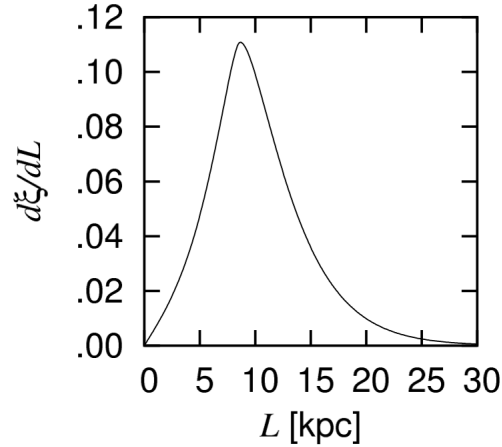
Figure 2.15: Distribution of core collapse supernovae precursors in our galaxy, assuming no extra density in the galactic center ($f = 0$).

2.3.2 Neutral Current Coherent Scattering

Coherent neutrino-nucleus elastic scattering is a neutral current weak interaction:

$$\overset{\scriptscriptstyle(-)}{\nu} + (Z, A) \to \overset{\scriptscriptstyle(-)}{\nu} + (Z, A) \,. \tag{2.47}$$

From a theoretical point of view, it is the same process of neutrino-nucleon neutral current scattering. If the momentum of the incoming neutrino is small enough, the single nucleon components (protons and neutrons) will not be distinguished and the nucleus will be scattered as a whole. The scattering amplitudes for the different nucleons then coherently sum to give the total cross section. This turns out to be enhanced by a factor of the order of the square of the neutron number compared to that of a single nucleon.

Neutral current coherent scattering (or NCCS) is a flavor independent process whose cross section doesn't depend on the neutrino flavor. It is reasonably well known because it's dynamics is a straightforward extension of the neutrino-nucleon elastic scattering one. The cross section can be written as ([1])

$$\frac{\mathrm{d}\sigma_{\mathrm{NCCS}}}{\mathrm{d}\Omega} = \frac{G_F^2}{4\pi^2} E^2 (1 + \cos\theta) \frac{Q_w^2}{4} F(Q^2)^2 \tag{2.48}$$

where G_F is the Fermi constant and θ is the angle between the original and the scattering direction of the neutrino. Q_w is the weak charge of the nucleus. This factor accounts for the enhancement of the cross section due to the coherent superposition of single-nucleon amplitudes and is

$$Q_w = N - (1 - 4\sin^2\Theta_W)Z \qquad (2.49)$$

where N and Z are respectively the number of neutrons and protons within the nucleus and Θ_W is the weak mixing angle. Since $\sin^2\Theta_W \simeq 0.231$, almost only neutrons contribute to the weak charge.

The coherent behaviour of the interaction will depend on the actual momentum transfer between the scattering particles (neutrino and nucleus). The higher the momentum transfer, the higher the capacity of the neutrino to distinguish the single components of the nucleus, and hence the smaller the cross section. The term $F(Q^2)$ in Eq. 2.48, called nuclear form factor, is the parameter that accounts for this dependence of the cross section on the momentum transfer. The form factor is specifically the Fourier transform of the density distribution of neutrons and protons within the nucleus. If the distribution of protons is well known from electron scattering ([50]), an experimental measure of the neutrons density distribution can proceed only through the observatino of neutrino-nucleus NCCS itself, hence only theoretical models of the distribution of nucleons waveforms within the nucleus can provide estimations of the nuclear form factors for neutral current interactions. In [51] an extensive discussion on analytical descriptions of the nuclear form factor is presented. A realistic analytic approximation of the nucleon density (partially derived from a reasonable extension of the charge distribution measured with electron scattering) can be obtained by writing the density in the form

$$\rho(r) = \int \mathrm{d}^3r' \rho_0(r')\rho_1(r - r') , \qquad (2.50)$$

where ρ_0 is constant inside a sphere of radius $R_0^2 = R^2 - 5s^2$ (with $s \simeq 0.5\mathrm{fm}$ and $R = (1.2 \times A^{1/3})\mathrm{fm}$) and

$$\rho_1(r) = \exp\left[-\frac{1}{2}\left(\frac{r}{s}\right)^2\right] . \qquad (2.51)$$

The function ρ represents a nearly constant interior density and a surface of thickness $\sim s$ where the density drops gradually. Its Fourier transform is

$$F(Q) = \frac{3j_1(QR_0)}{QR_0}\exp\left(-\frac{(Qs)^2}{2}\right) \qquad (2.52)$$

Numerical integration of distributions considered even more realistic yields very similar results. Inserting the explicit form of the spherical bessel function j_1 in Eq. 2.52 the

form factor reads

$$F(Q) = \frac{3\left(\frac{\sin(QR_0)}{(QR_0)^2} - \frac{\cos(QR_0)}{QR_0}\right)}{QR_0} \times \exp\left(-\frac{(Qs)^2}{2}\right) . \tag{2.53}$$

In Fig. 2.16 the form factors for tellurium and oxygen (the target nuclei in CUORE experiment) are plotted. The different behavior of Te and O form factors reflects the
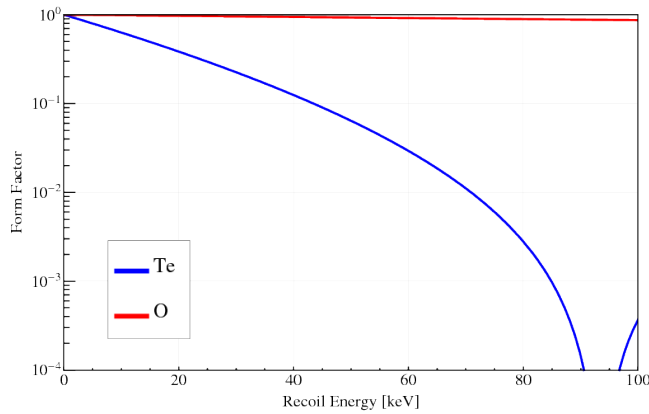
Figure 2.16: Form factors for tellurium (blue) and oxygen (red) nuclei for recoil energy up to 100keV.

fact that the larger is the nucleus the smaller is the energy (or, better, the transferred momentum) that the neutrino is allowed to have in order to interact via coherent scattering. Increasing from few to about 50keV the tellurium nucleus recoil energy the form factor drops by an order of magnitude, while oxygen form factor remains almost unchanged. This is an important issue for its experimental implications: heavy nuclei, like tellurium, are favored target for coherent scattering because of the large number of neutrons, but the corresponding recoil energy spectrum will be strongly suppressed at energies higher than few keV; the performance of the detector at low energy, in particular its energy threshold, assume a fundamental role if coherent scattering has to be exploit for neutrinos detection.

Chapter 3

Background in CUORE

In this chapter the background of the CUORE experiment will be analyzed. For a rare event experiment the reduction of the background is mandatory, and usually represents the greatest challenge and requires the greatest efforts. Background is, in general, any event that can be recorded by the detector, and that shows the same features of an event generated by the physics that the experiment is studying. The most dangerous backgrounds are, of course, the ones that cannot be recognized and tagged by means of any feature, mimicking exactly the searched signal.

The fact that a given physics event is a background or not depends both on the physics that is being studied and the detector properties and performance; the simplest example is the detector energy resolution: if the signature of the phenomenon that is searched for is a monochromatic peak in the energy spectrum, a good energy resolution will help in recognizing the real events from the events generated by different phenomena but characterized by a similar energy deposition in the detector. A similar argument is valid for the events topology, timing, the particle identification capabilities, the energy deposition density, etc.

In the following a general discussion on the CUORE background sources will be addressed, with some attention on the background that affects the main physical goal of the experiment, i.e. the neutrinoless double beta decay. This background can be defined "high energy background" because it affects the higher part of the energy spectrum of CUORE bolometers. In the last sections more attention will be devoted to the background relevant for the detection of supernova neutrinos that can be defined "low energy background" because it contributes to the counting rate just above the detector threshold. The sources of the two backgrounds are, as natural, often common or at least strongly correlated. In the very last section a recent R&D project for the tagging of degraded alpha particles-induced background is described.

3.1 High energy background

For the purpose of the discussion that will be presented in the following of this chapter (and essentially because of the different nature and/or criticality of the background sources involved) it is useful to identify three different regions of the experimental setup, one outside the cryostat (in the normal atmosphere) and two inside the cryostat (both in vacuum):

- the near region, namely the volume occupied by the bolometer array and its external copper covering consisting in the 10 mK shield and the top and bottom copper plates. All the elements belonging to this region face directly the detectors. As already described in Section 1.2, the array consists in a cylindrical matrix of 19 towers, each containing 13 planes of four crystals. The 988 TeO_2 crystals are secured – with small PTFE spacers – inside a copper skeleton made of frames and columns, the cabling system will be located inside copper wire-trays disposed on the lateral side of each tower, only the terminations of the cabling system (PEN-Cu cables) will be directly faced to the detectors. None of the copper parts of the holder will touch the crystals. The amount of materials different from copper or TeO_2 in the near region will be reduced to a minimum. It will consist in the elements of the detector: the thermistor (used for the bolometric signal read-out), the Si resistor (used to measure the bolometer thermal gain), the epoxy used to attach the two chips on each crystal, the gold wires bonded on the two chips for the electrical connection and the PTFE spacers. We will refer to these components as *small parts* of the detector. Finally, all the copper used in the near region will be of the NOSV type.

- the far region, namely all the remaining cryostat volumesi. Indeed they are sufficiently far from the detector, so that only their gamma emission is relevant. Elements contained in this region are the internal lead shield and the thermal shields from the 50 mK to the 300 K outwards. The far region includes all the volumes delimited by two thermal plates: V2 is the volume between the 300 K and the 40 K, followed by V3, V4, V5 and V6 as indicated in Fig. 3.1. These volumes are in vacuum and are partially taken by the refrigerator system (the dilution unit and its pumping line) and the cabling system. All the copper used in the far region will be of the OFE type.

- the external region, labeled V1 and corresponding to the volume external to the the cryostat (mainly above the top plate) as indicated in Fig. 3.1. Here the electronics, the pulse-tubes and the pumping lines will be installed.
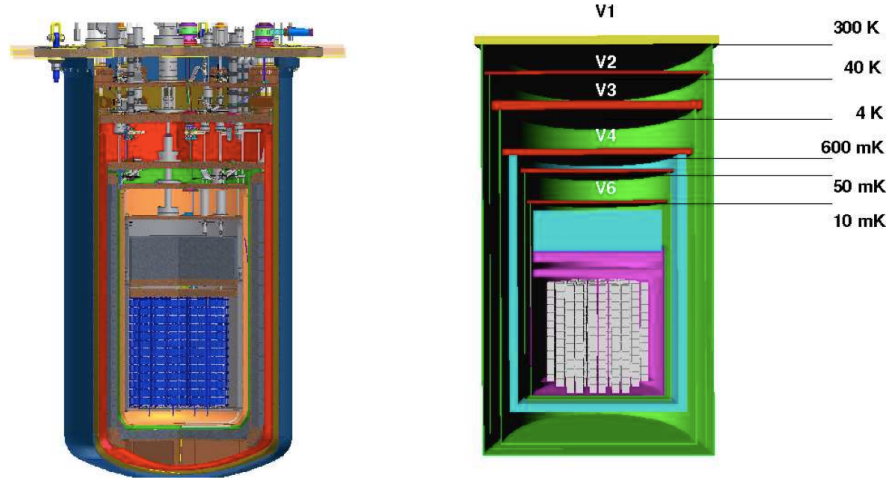
Figure 3.1: Left: 3D view of the CUORE apparatus. Right: geometry implemented in the MC simulation.

3.1.1 CUORE background sources

^{130}Te decays with a Q-value that is definitely larger than the energies of the most common environmental gamma lines. In the case of the natural radioactive chains, there is only one isotope emitting a photon with an energy higher than the ^{130}Te Q-value and a B.R. > 1%: the 2615 keV line of ^{208}Tl (^{232}Th chain). In this respect, the choice of the $\beta\beta0\nu$ candidate can be considered as the first step towards background suppression. Indeed, only a limited number of sources can mimic a $\beta\beta0\nu$ event, contributing to the background counting rate in the ROI (Region Of Interest). These can be grouped into the following three classes:

1. in the external region: environmental muons, neutrons and photons (these only if sufficiently hard);

2. in the far region: gamma emission from ^{208}Tl;

3. in the near region: alpha, beta and gamma emissions from the ^{232}Th and the ^{238}U chains, as well as from few cosmogenically activated isotopes.

A remark is here important. Bolometers are characterized by a fully sensitive volume, including their surface (no dead layer is present) therefore also alpha and beta emissions

can provide relevant contributions to the counting rate. Obviously – given the short range of these particles – the effect is important only for elements directly facing the bolometers (or in the bolometer themselves). Two examples are useful to appreciate the effect of surface contaminations:

1. Fig. 3.2 illustrates how ^{238}U or ^{232}Th surface contaminations in TeO$_2$ crystals influence the background counting rate in the ROI. The peaks produced by the alpha particles emitted in the decay chain are characterized by low energy tails that extend down into the ROI. These tails are due to alpha particles that loose only a fraction of their energy in the crystal and a fraction outside it: either in the inert material surrounding the crystal or in the nearby bolometer. In the former case these events are an irreducible background that can be quite relevant in the ROI. In the latter, they can be rejected by the so-called coincidence analysis since two bolometers (the crystal containing the decaying isotope and the crystal receiving the emitted alpha particle) simultaneously record a signal (*double-hit event*). From the point of view of the identification of background sources, crystal surface contaminations have a strong and clear signature provided by double-hit events: when the source of this coincidence signal is an alpha decay, the energy associated to the double-hit event (namely the sum of the energies recorded by the two detectors that records the signals) is the decay Q-value.

2. Fig. 3.3 illustrates the effects of ^{232}Th and ^{238}U surface contaminations of the copper structure holding the TeO$_2$ crystals. In both cases a large fraction of the background counting rate in the ROI is due to degraded alphas. This kind of impurities produces a background with a very weak signature. Generally, the region between the highest gamma peak (2615 keV) and the lowest alpha peak (4 MeV) is dominated by these contaminants and can be used to quantify the impurity concentration (we will refer to this region as the *3-4 MeV region*). When alpha and beta particles are efficiently shielded, the contribution of surface contaminations is indistinguishable from that of impurities present in the material bulk (see Fig. 3.3). For this reason we analyze the problem of surface contaminations only for elements directly facing the crystal.

The relevance of surface contaminations was already recognized in the two TeO$_2$ bolometric experiments precursors of Cuore: MiDBD ([52, 53]) and CUORICINO ([54, 55, 56]). As an example, the study performed on a partial statistics of CUORICINO data [57, 58] allowed to identify three main contributions to the flat background that characterizes the CUORICINO counting rate in the ROI (see Fig. 3.4):
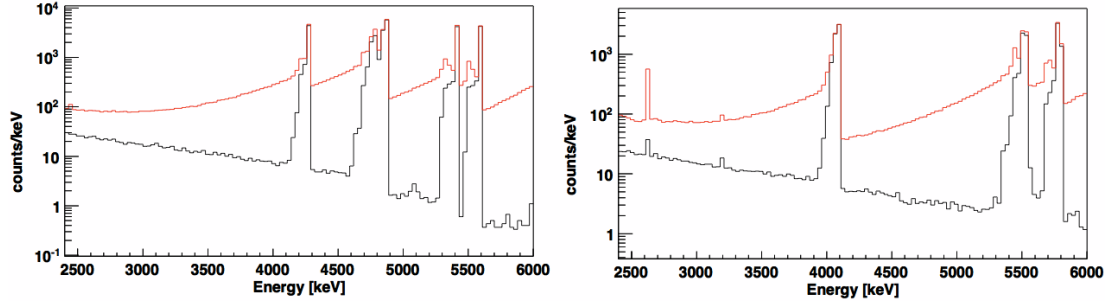
Figure 3.2: The plot illustrates the effect of ^{238}U (left panel) and ^{232}Th (right panel) alpha contaminations in CUORE crystal. The spectra have been obtained simulating a 1 μm deep contamination (exponential density profile) on the surface of the CUORE array. The effect of a single-hit cut (black histogram) is to reduce the counting rate by about 1 order of magnitude in the $\beta\beta0\nu$ ROI.
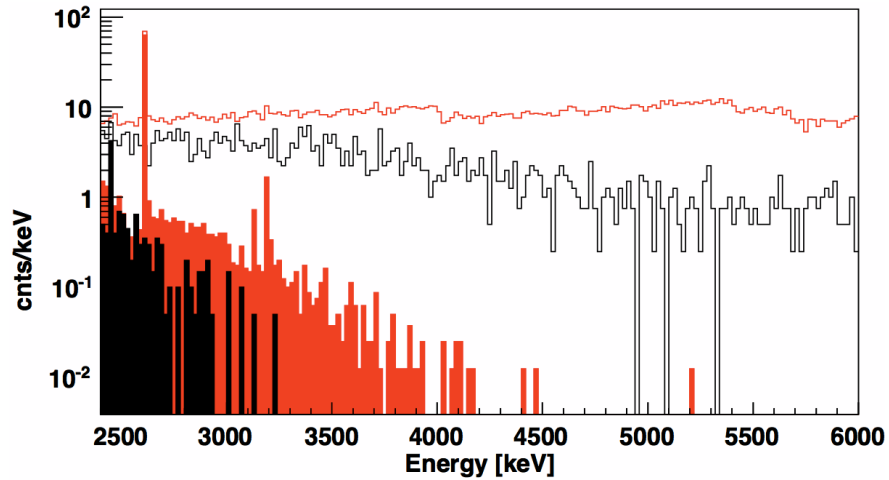
Figure 3.3: The plot illustrates the effect of ^{232}Th (red spectra) and ^{238}U (black spectra) contaminations in the copper used for the bolometer holder. The spectra have been obtained by simulating a surface contamination with an exponential density profile ($\lambda = 10$ μm) with a dedicated montecarlo tool for a 12-crystal array made of 3 CUORE-like planes, closed in a copper box. If the copper is covered with a 70 μm thick layer of polyethylene (filled histograms) almost all the alpha particles are stopped before reaching the bolometers. The spectra change drastically and results dominated by gamma and betas (responsible also of the few events above the 2615 keV line).

1. $(10 \pm 5)\%$ of the measured rate is ascribed to surface contaminations of the TeO$_2$ crystals in ^{238}U and/or ^{232}Th;

2. $(30 \pm 10)\%$ to multi-Compton events of the ~ 2615 keV gamma ray originated from a ^{208}Tl (^{232}Th chain) contamination of the cryostat or of its shields;

3. $(50 \pm 20)\%$ to surface contaminations of inert materials surrounding the crystals, most likely copper.

CUORE will benefit of a completely new set-up that has been designed to reduce to negligible levels the background induced by environmental and material radioactivity (and in particular of the 2615 keV multi-Compton). The main construction materials (copper and lead) were selected in order to be able to reach this goal and the radioactivity of any object installed in the external or far regions of the cryostat has to satisfy specific (integral) limits. The radioactivity of the detector (and of any other material included in the near region) is therefore expected to be the one that will determine the final background figure of merit of the experiment.

The detector structure was designed in order to minimize the impact of all the known background sources. This is achieved both by minimizing the mass of the materials facing the detectors (and thus the amount of radioactive sources) and reducing the dead space between the crystals because this increases the likelihood that unwanted cosmics and radioactive decays produce simultaneous hits in more detectors. As mentioned above, multi-hit events are easily identified and rejected (*single-hit* cut), reducing in this way the background counting rate without a relevant reduction of the $\beta\beta0\nu$ signal detection efficiency. Figure 3.2 shows how this cut can be effective. As in the case of the near and external regions, for any object that will be located in the near region specific studies were performed in order to verify its bulk and surface contamination and the impact on the CUORE counting rate.

3.1.2 Simulation tools

QSHIELDS is the GEANT4-based Monte Carlo simulation code used for CUORE. In the simulation the geometry of the detector, of the cryostat and of the internal and external shields is reproduced (see Fig. 3.1). The code is maintained and continuously updated upon changes of detector and of the set-up details. Elements of the set-up included in this simulation are the crystals, the copper structure that holds the array, the different thermal shields and other cryostat parts, the internal and external lead and polyethylene shields. Each of them can be studied as an active source whose bulk or surface contamination is simulated independently, in order to evaluate its impact
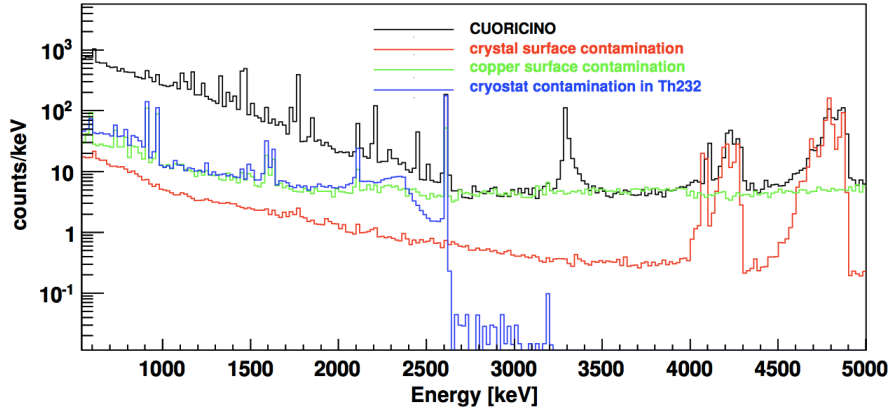
Figure 3.4: The plot illustrates the CUORICINO background model: the black histogram is the single-hit spectrum recorded by CUORICINO $5 \times 5 \times 5$ cm^3 crystals. The counting rate above ~ 2.5 MeV is explained on the basis of three different sources, whose effects are here reproduced by a MonteCarlo simulation. The first is a crystal surface contamination in ^{232}Th and ^{238}U (red histogram) that accounts for the visible alpha peaks. The second is a surface contamination of the crystal copper holder, in this plot ascribed to ^{232}Th (green histogram). The third is a ^{232}Th contamination of the cryostat and/or its shields, (blue histogram). Below 2.5 MeV other contributions, mainly ^{238}U contamination of the cryostat and/or its shields are needed to explain the observed background. The peak appearing at ~ 3.3 MeV is ascribed to an internal contamination in ^{190}Pt of the crystals, producing the clearly visible peak as only contribution.

on the observed data, in particular in the ROI. With the exception of few elements (the detector *small parts* and the copper frames and columns) the effects of radioactive contaminations can be studied for the whole detector. For the missing parts, a dedicated GEANT4-simulation based on a multipurpose code named ARBY is used. QSHIELDS and ARBY include the propagation of photons, electrons, alpha particles and heavy ions (nuclear recoils from alpha emission) as well as neutrons and muons. All the simulations discussed in this section are based on the *Livermore GEANT4 Physics List*, unless differently indicated. The generation of nuclear transitions and the reproduction of the detector operating features are based on two dedicated packages (GENDEC and G2TAS) that have been developed to correctly simulate chains of radioactive decays in secular equilibrium (GENDEC) and to fully exploit and reproduce the capability of bolometer arrays in terms of coincidence analysis (G2TAS). These two packages are described in detail in [53]. ARBY is used also for the simulation of HPGe and Si surface barrier measurements, as well as the bolometric measurements carried out with small test arrays.

3.1.3   Simulation inputs

The simulation uses as input the contamination levels assumed or measured for all the CUORE materials. These measurements are shortly summarized in the two following sections. The techniques used are:

- <u>bolometric</u>, used only when other techniques fail in reaching the required sensitivity ([53, 58, 9]). These measurements are carried out in the cryogenic facility installed at LNGS in the underground experimental Hall C or in the cryostat used for the CUORICINO experiment in Hall A using small TeO_2 arrays. In particular:

  1. for TeO_2 crystals a single-floor 4-crystal array (CCVR for CUORE Crystal Validation Run) is used to periodically check the internal and surface contamination of crystals coming from the different CUORE production batches ([9]);

  2. a two-plane 8-crystal array (RAD detector [59]) was used to check the bulk contamination of Si heaters and Au bonding wires;

  3. a 3-tower detector (TTT for Three Towers Test [60]) was used to analyze the copper surface contamination level, comparing different surface treatments techniques. The TTT detector consisted in three 3-floor arrays (12 crystals for each array) each closed in its own copper box (Fig. 3.5). The first tower (T1) was realized covering all the copper parts (frames, columns and copper box) with several layers of polyethylene film, for a total thickness of $\sim$70 μm. The second (T2) and third (T3) towers were identical to the first but the surface of all the copper detector elements was processed with two different cleaning techniques and no polyethylene was used. The towers showing the best results – total spectra must be compared because coincidence analysis could be applied only to T1, whose total rate in the 3-4MeV region was 0.068 ± 0.006counts/(keV kg y) – were the T3 detector, realized with copper treated with the TECM technique (a complex cleaning procedure developed at LNL and hereafter chosen as the baseline for CUORE, TECM here stands for Thumbler, Electropolishing, Chemical-etching and Magnetron plasma cleaning [60]) and T1, with compatible counting rates. This measurement presently provides also the best results on the background contribution coming from PTFE-spacers surface contamination;

- <u>HPGe</u>, Hyper-Pure Germanium diode gamma spectroscopy. These measurements are performed in the Radioactivity Laboratories of LNGS and Milano-Bicocca;

- <u>NAA</u>, Neutron Activation Analysis. The measurements are done by the Milano-Bicocca Radioactivity Laboratory in collaboration with the LENA reactor in Pavia;

- <u>Si diodes</u>, alpha spectroscopy with Si surface barrier detectors. These measurements are performed in the Radioactivity Laboratories of Milano-Bicocca and LNGS, they are used to study surface contamination of various components, most often with a pre-screening purpose.

In the case of environmental radiation, the fluxes of muons, neutrons and gamma rays in the laboratory environment - as reported in literature - have been used.
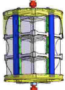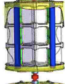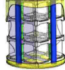
TTT	Detector	3-4 MeV rate cnts / (keV kg y)	Sources
	T1 - copper wrapped with polyehtylene film	0.052 +/- 0.008 with single-hit cut	TeO$_2$ crystals (partially subtracted) PTFE spacers polyehtylene film
	T2 - copper treated with an etching procedure	0.120 +/- 0.012 no coincidence cut	TeO$_2$ crystals PTFE spacers copper
	T3 - copper treated with TECM procedure	0.072 +/- 0.008 no coincidence cut	TeO$_2$ crystals PTFE spacers copper

Figure 3.5: Left: the Three Tower Test detector. The three arrays differ only in the treatment of copper parts: T1 has all the copper covered with polyethylene film, T2 and T3 use naked copper treated with two different chemical procedures; an etching was done on T2 copper parts while the TECM procedure was applied to T3 copper (see text for a more comprehensive explanation). Right: a summary of the main detector features (column 1), the resulting background in the 3-4 MeV region (column 2) and the sources that more likely contribute to the 3-4 MeV background (column 3). Crystal and PTFE-spacers contamination are common contributions to the three detectors. However, crystal contribution to 3-4 MeV background is partially rejected in T1 which is the only tower where all the detector were active, allowing an efficient use of the single-hit cut (removing coincidences between two crystals).

3.1.3.1 Bulk contaminations

In the case of bulk contamination we limit our analysis to ^{238}U and ^{232}Th chains and few cosmogenically activated isotopes. All the other radio-isotopes typically contributing to the environmental radioactivity are neglected because they have either a much lower activity (this is the case of ^{235}U when compared to ^{238}U) or a too soft radiation

to contribute in the ^{130}Te ROI. A special case, where isotopes other than those typically contributing to the environmental radioactivity can be present, is that of the Ge thermistors (namely the temperature sensors glued on the TeO$_2$ crystals). These thermistors are obtained doping a Ge wafer through neutron irradiation (the technique is called NTD for Neutron Transmutation Doping) in a nuclear reactor. Several different radioactive isotopes can be there produced. According to our measurement ([61]) all these isotopes have very low Q-values if compared to the ^{130}Te transition energy, therefore this kind of radioactivity will not be considered here. Moreover, different signal shapes are forseen for events generated by particles that release at least a fraction of their energy inside the thermistor.

Cosmogenic activation. The interaction of cosmic rays on the materials present in the largest amount in the experiment, i.e. copper, lead and TeO$_2$, can produce potentially dangerous radioactive isotopes. Copper and Tellurium are the nuclei with the largest cross sections, therefore we restrict our analysis to them. The activation takes place before the underground storage of the materials and is evaluated on the basis of the cosmic ray flux at sea level (indeed none of the mentioned materials is transported by air), the material exposure and cooling times and the measured or calculated activation cross sections. To be able to mimic a $\beta\beta0\nu$ decay these isotopes need to have a Q value larger than $\sim$2.5 MeV and a reasonably long half-life (in order to survive with a relevant activity after the storage in the underground cavern). The isotopes that match these criteria are:

- ^{60}Co ($\tau_{1/2}$= 5.27 years) that is produced by cosmic ray interaction on both Copper and Tellurium nuclei. ^{60}Co beta decays with a Q-value of 2.8 MeV with the contemporary emission of two photons and an electron. To mimic a $\beta\beta0\nu$ event it is necessary that both the photons and the electron deposit energy in the same crystal, that means that this isotope produces a dangerous background only when it is present inside TeO$_2$ crystals or in a shallow layer of the copper directly facing the bolometers.

- ^{110m}Ag ($\tau_{1/2}$= 249.8 days, Q-value=3.0 MeV) that is produced by cosmic ray interaction on Tellurium nuclei. This isotope beta decays to ^{110}Ag ($\tau_{1/2}$= 24.6 seconds, Q-value=2.9 MeV) that successively beta decays to the stable ^{110}Cd. Both the decays can mimic a $\beta\beta0\nu$ event (with the exception of the 10% cases where ^{110}Ag decays by EC to the stable ^{110}Pb).

In order to ensure that the activation level be compatible with CUORE requirements, both the TeO$_2$ and the copper exposures to cosmic rays were reduced to a minimum:

∼3 months from crystal growth to the underground storage at LNGS for TeO$_2$ (and a cooling time of about 2.5 years on the average), ∼4 months from cast to the final storage at LNGS for the copper used for the production of detector parts (the cooling time is in this case difficult to evaluate since it depends on the history of the different pieces, namely when they are machined in the above ground workshop). On the basis of the known cross sections of Copper and Tellurium the following activities are expected at Spring 2014 (start of CUORE):

- < 50 μBq/kg of ^{60}Co in the copper of the detector mounting structure (the exact activation level will be different for the various detector parts according to their history, the ^{60}Co contamination in the procured copper was measured with HPGe and is < 25 μBg/kg);

- ∼15 nBq/kg of ^{60}Co in the TeO$_2$ crystals (this level is far below the HPGe sensitivity, and also bolometric measurements like CCVR ones are not sufficiently long to set an useful upper limit);

- ∼0.4 μBg/kg of ^{110m}Ag in the TeO$_2$ crystals, and the same activity for its daughter ^{110}Ag in secular equilibrium.

^{238}**U and** ^{232}**Th contaminations.** In Tab. 3.1 we report results for ^{238}U and ^{232}Th bulk contaminations of the most important CUORE materials (those contained in larger quantity or those used for the construction of the detector). The measurements are done with different techniques, according to the required sensitivity, the available mass and the material properties. Breaks in secular equilibrium are investigated - whenever possible - for each sample. In Tab. 3.1, however, only values corresponding to the chains in secular equilibrium are reported.

When procurement of the material is still to be completed, results obtained with similar materials (mainly used in past experiments) are presented – as a reference – in order to demonstrate the radiopurity levels attainable for that item. Few remarks on Tab. 3.1 are important:

- for the NTD Ge thermistor the contamination refers to Ge bulk and is obtained from the Ge-wafer producer specifications. After doping, a metallic deposition is realized on the Ge surface, its contamination is analyzed as a surface contamination in the next paragraph. It is worth to note that the study of the contamination of NTD Ge thermistors should take into account that in most cases signals originating from nuclear decays inside the Ge are deformed in their shape and therefore rejected with high efficiency by the analysis.

- for the polyethylene film (which was used to wrap the detector copper parts in T1 and is an alternative solution to the TECM copper cleaning, to be used for wrapping the detector copper shield at 10mK in CUORE) we present two evaluations, one obtained with HPGe spectroscopy on new material, the other obtained from the T1 bolometric measurement. In both cases the bulk contamination obviously account also for surface contaminants, since several layers of film are used (the surface to volume ratio is extremely high). As a consequence this can be converted into a highly sensitive determination of surface contamination levels. One difference exists between the two measurements: in HPGe spectroscopy the exposure to normal air after production was extremely short. In the case of the T1 measurement it was much longer;

- for the wiring system, consisting in PEN tapes on which copper strips have been deposited to form the wires, the substrate have been investigated with gamma spectroscopy while the surface deposition is investigated with Si barrier detectors.

3.1.3.2 Surface contaminations

Materials show very often contaminations on their surfaces that are in excess with respect to the bulk ones. Impurities are added to a material during its machining, cleaning and its exposure to "contaminated" air. In this case, the effect of breaks in the secular equilibrium can be relevant, in particular for the ^{210}Pb isotope in the ^{238}U chain. Indeed, ^{222}Rn emanation from the materials contaminated in ^{238}U produces excess concentrations of ^{210}Pb (the only long living isotope in ^{222}Rn progenies) in air and dust. This can induce contamination and re-contamination of the materials that have to be investigated.

When studying surface contaminations for CUORE, two different approaches are applied. For elements in the far region, surface contaminations are checked with Si surface barrier detectors, in this case surface contaminations generally do not constitute a real problem and accurate cleaning and storage with standard techniques are enough to ensure a negligible level of background. For materials in the near region also specific bolometric measurements are often required and carried out. Indeed, as discussed in Section 3.1.1, these contaminants are extremely dangerous and all the bolometric detectors operated so far have shown important background contributions ascribed to them.

Neglecting the detector *small parts* – mainly because of their extremely reduced surface area – the elements that are likely to give a relevant contribution to surface induced background and that were included in our analysis are:

BULK CONTAMINATIONS OF CUORE CONSTRUCTION MATERIALS

Material	Sample	^{232}Th [Bq/kg]	^{238}U [Bq/kg]	Technique
TeO$_2$ crystals	CUORE	$<8.4 \cdot 10^{-7}$	$<6.7 \cdot 10^{-7}$	bolometric (CCVR)
glue (Araldit Rapid)	CUORICINO	$<2.7 \cdot 10^{-3}$	$<8.2 \cdot 10^{-3}$	HPGe
PTFE spacers	CUORE	$<6.1 \cdot 10^{-6}$	$<2.2 \cdot 10^{-5}$	NAA
Au wires	CUORICINO	$<1.2 \cdot 10^{-1}$	$<9.8 \cdot 10^{-2}$	bolometric (RAD)
Si heaters	CUORE	$<3.3 \cdot 10^{-4}$	$<2.1 \cdot 10^{-3}$	bolometric (RAD)
NTD Ge thermistors	test sample	$<4.1 \cdot 10^{-3}$	$<1.2 \cdot 10^{-2}$	producer spec.
PEN cables	CUORE	$<1.0 \cdot 10^{-3}$	$<1.3 \cdot 10^{-3}$	NAA(Th)+HPGe(U)
polyethylene film	test sample	$<1.2 \cdot 10^{-3}$	$<1.4 \cdot 10^{-3}$	HPGe
wrapped polyethylene film	test sample	$<2.1 \cdot 10^{-1}$	$<1.6 \cdot 10^{-1}$	bolometric (T1)
NOSV Cu	CUORE	$<2.0 \cdot 10^{-6}$	$<6.5 \cdot 10^{-5}$	NAA(Th)+HPGe(U)
Roman Pb	CUORE	$<4.3 \cdot 10^{-5}$	$<4.6 \cdot 10^{-5}$	HPGe
OFE Cu	CUORE	$<6.4 \cdot 10^{-5}$	$<5.4 \cdot 10^{-5}$	HPGe
COMETA Pb	CUORE	$<1.2 \cdot 10^{-4}$	$<1.4 \cdot 10^{-4}$	HPGe
Stainless steel 300 K plate	CUORE	$<1.0 \cdot 10^{-2}$	$<5.0 \cdot 10^{-3}$	HPGe

Table 3.1: 90% C.L. upper limits (if not otherwise indicated) on bulk contamination of detector and cryostat materials. Activities are expressed in Bq/kg (1 Bq/kg = 246·10^{-9} g/g for ^{232}Th and 81·10^{-9} g/g for ^{238}U). The label "CUORE" in the second column indicates a direct measurement of the material procured for CUORE; the label "CUORICINO" indicates that the measurement refers to the material used in CUORICINO; the label "test sample" stands for a material not jet procured for CUORE. In the last column the measurement technique is indicated, as described in the text.

- the detector holder (frames and columns);

- the two plates that close the tower array on the top and on the bottom (support plates);

- the detector cabling system consisting in the copper wire-trays and the flat PEN cables that are only partially covered by the wire-trays;

- the innermost (close to the detector) thermal shield (10 mK shield) that closes the detector on the side;

- the PTFE-spacers that, although listed among the detector *small parts*, have a not negligible area facing the bolometers;

- the crystals themselves.

The measurement of the surface contamination concentration is not trivial. A prescreening is done with Si surface barrier detectors whose sensitivity, however, often happens to be poorer than needed. Consequently, the measurement on the final samples for CUORE is performed with small bolometric arrays, able to reach a sensitivity of few nBq/cm^2. Whatever the technique adopted, the real difficulty is the quantification of the contamination. It is done – as in the case of bulk contamination measurements – by comparing experimental and simulated data. Bulk contaminations are described with a single parameter model: a uniform distribution of impurities in the contaminated volume. Surface contamination, on the contrary needs to be described in terms of the thickness of the contaminated layer and of the density distribution of contaminants in it. Both are unknown and experimental data are usually too poor to infer all the needed information without ambiguity. For this reason the data are interpreted on the basis of a fixed model for the density profile of impurities distribution. This model is reasonable from the point of view of the mechanisms that could give rise to surface contamination (namely diffusion of impurities) and appears to be capable of providing a good description of the measured data ([53]). A surface contamination is described by an exponential density profile for the impurities concentration inside the contaminated layer

$$\rho = \rho_0 \times exp(-d/\lambda) \,. \tag{3.1}$$

When needed, the distribution is truncated at 1 mm. Since in most cases experimental data are not enough to measure both the characteristic depth of the contamination (λ) and its intensity (ρ_0), for each λ – the maximum contamination compatible with experimental data is evaluated. The surface activity (measured in Bq/cm^2) is obtained as the total activity of the contaminated layer divided by the emitting surface area. ARBY is

SURFACE CONTAMINATIONS OF CUORE CONSTRUCTION MATERIALS

Material	Sample	Depth [μm]	^{232}Th [Bq/cm^2]	^{238}U [Bq/cm^2]	^{210}Pb [Bq/cm^2]	Tecnique
TeO$_2$ crystals	CUORE	0.01	$<1.6 \cdot 10^{-9}$	$<6.3 \cdot 10^{-9}$	$<9.8 \cdot 10^{-7}$	bolometric (CCVR)
		0.2	$<2 \cdot 10^{-9}$	$<7.6 \cdot 10^{-9}$	$<2.2 \cdot 10^{-8}$	"
		1	$<1.9 \cdot 10^{-9}$	$<8.9 \cdot 10^{-9}$	$<9.2 \cdot 10^{-9}$	"
		5	$<1.0 \cdot 10^{-9}$	$<5.4 \cdot 10^{-9}$	$<5.6 \cdot 10^{-9}$	"
		10	$<8.3 \cdot 10^{-10}$	$<4.4 \cdot 10^{-9}$	$<4.9 \cdot 10^{-9}$	"
Copper	TECM	0.1-10	$<7 \cdot 10^{-8}$	$<7 \cdot 10^{-8}$	$<9 \cdot 10^{-7}$	bolometric (T3)
PEN cables	CUORE	0.1-30	$<4 \cdot 10^{-6}$	$<5 \cdot 10^{-6}$	$<3 \cdot 10^{-5}$	Si diode
PTFE spacers	CUORE	0.1-30	$<6 \cdot 10^{-7}$	$<5 \cdot 10^{-7}$	$<7 \cdot 10^{-6}$	bolometric (T1)
NTD Ge thermistors	test sample	0.1-10	$<8 \cdot 10^{-6}$	$<5 \cdot 10^{-6}$	$<4 \cdot 10^{-5}$	Si diode

Table 3.2: 90% C.L. upper limits on surface contaminations of TeO$_2$ crystals and copper. Different contamination depth are considered. In the case of copper the results here presented refer to materials that have been cleaned with the TECM technique.

used for the simulation of both Si spectroscopy or bolometric tests. The minimum considered depth is 0.01 μm for TeO$_2$ crystals and 0.1 μm for any other material. Indeed, these are the most shallow distributions whose effects can be experimentally identified. The maximum depth is $\sim$10 μm for copper and TeO$_2$ (the range of 5 MeV alpha particles in these materials is $\sim$10 and $\sim$15 μm respectively) and 30 μm for polyethylene and PTFE (where the range of 5 MeV alpha particles is $\sim$34 and $\sim$23 μm respectively). Thicker depths are almost indistinguishable from a bulk contamination. In Tab. 3.2 we report the results obtained for different materials. Few remarks are important to clarify the meaning of the results here discussed.

- in the case of TeO$_2$ the reported results are obtained with crystals belonging to the final CUORE production in CCVR measurements ([9]). For the crystals, the signature of a surface contamination – when operating an array of TeO$_2$ bolometers – can be very strong and easily identifiable, allowing the distinction of ^{232}Th and ^{238}U contaminations and the study of their secular equilibrium. Nonetheless in Tab. 3.2 we only quote upper limits on U and Th surface contamination, mainly because of the low statistics collected in the CCVR measurements. For this same reason we are not able to identify the unique depth of the contamination and different models are considered, each being able to account for the measured spectrum.

- for what concerns the inert materials (we analyze here the copper cleaned with the TECM technique, the PEN cables, the NTD thermistors and the PTFE) the signature used to investigate a surface contamination is extremely weak. This is reflected in the upper limits of Tab. 3.2 that exceed by at least one order of magnitude those obtained for TeO$_2$ crystals. In particular, we are interested to a contamination deep enough ($>$0.1 μm) to account for the continuous background that all our bolometers record in the 3-4 MeV region. The contamination levels reported in Tab. 3.2 are obtained assuming that the whole counting rate of the detector in the 3-4 MeV region is due to the surface contamination of the sample under study. For example, in the case of TECM copper the upper limit reported in Tab. 3.2 is extrapolated from T3 result, assuming the whole 3-4 MeV counting rate as due to a surface contamintion of the copper mounting structure (frames+columns+box), therefore neglecting the other sources that could contribute to this rate, namely crystals and PTFE. Similarly, the PTFE surface contamination is extracted from T1 result (assuming negligible any contribution different from PTFE). In the case of measurements done with Si surface barrier detectors, the intrinsic background of the Si diode and that of its vacuum

chamber is assumed negligible. Contaminations with depths lower than 0.1 μm can't account for the background mentioned above. Even when their presence is sure, the corresponding contribution is always extremely low and not worrisome for CUORE. Finally, due to the weakness of the signature used in this analysis, ^{238}U, ^{232}Th and ^{210}Pb "deep" contaminations produce undistinguishable effects. Therefore the upper limits quoted in Tab. 3.2 are mutually exclusive since they have been obtained ascribing the whole 3-4 MeV counting rate to one of the three sources at a time.

3.1.4 Simulation outputs

Once the simulation is performed with the inputs discussed in the previous section, the resulting simulated data can be used to extract the expected background counting rate in the ROI. Few remarks are important:

- in the external and far regions and for the inner lead shield, gamma induced background is analyzed considering only the 2615 keV line of ^{208}Tl. The intensity of this line is based on the ^{232}Th contamination of the element under analysis. In the simulation a single 2615 keV photon is generated;

- in the near region we consider ^{238}U, ^{232}Th and ^{210}Pb bulk and surface contaminations. For bulk contamination we use the upper limits reported in Tab. 3.2, for surface contaminations we use upper limits from Tab. 3.1.

- for cosmogenically activated isotopes we use the initial activity discussed in Section 3.1.3.1.

In all cases we assume to operate the CUORE array in anticoincidence (only single-hit events are accepted), with an energy threshold of 50 keV on each detector. We have used this kind of cut in the simulated spectra because of its simplicity. It is on the other hand very likely that the single-hit cut (or anticoincidence cut) in CUORE will consider only nearest neighbor crystals, in order to avoid the introduction of a high dead time due to accidental coincidences. However, in the cases discussed here, the difference between a global single-hit cut and a local one (considering only nearest neighbor crystals) is expected to be negligible. This is not true for the case of neutron and muon interactions, as discussed in Section 3.1.4.3.

CUORE ROI - ^{238}U AND ^{232}Th BULK CONTRIBUTIONS IN THE NEAR REGION

Element	ROI rate from ^{232}Th [cnts/(keV·kg·y)]	ROI rate from ^{238}U [cnts/(keV·kg·y)]
TeO$_2$ crystal bulk	<1·10^{-4}	<2·10^{-6}
glue (Araldit Rapid) *	<2·10^{-7}	<8·10^{-7}
PTFE*	<4·10^{-5}	<9·10^{-5}
Au wires*	<1·10^{-3}	<1·10^{-3}
Si heater*	<5·10^{-6}	<3·10^{-5}
Ge NTD thermistors	<1·10^{-4}	<8·10^{-4}
PEN cables	<1·10^{-7}	<9·10^{-8}
Cu columns and frames	<2·10^{-5}	<5·10^{-4}
Cu upper and lower plates	<3·10^{-6}	<4·10^{-5}
Cu wire-trays	<2·10^{-6}	<3·10^{-5}
Cu 10 mK shield	<2·10^{-5}	<1·10^{-4}

Table 3.3: 90% C.L. upper limits on CUORE counting rate in the ROI as obtained from bulk contaminations of elements belonging to the near region. Elements labeled with a * were simulated with **ARBY**, the effect of the anticoincidence cut is therefore not included.

3.1.4.1 The near region

Background contribution due to ^{232}Th and ^{238}U bulk contaminations in the elements belonging to the near region are summarized in Tab. 3.3. The weakest limit is that obtained for the Au bonding wires, and is a consequence of the poor sensitivity reached in the corresponding measurement. It is worth noting that the way the bulk contamination of gold was obtained is similar to the procedure adopted for surface contaminations (namely a normalization on the 3-4 MeV counting rate, see discussion in the next section). For this reason ^{232}Th and ^{238}U limits exclude each other (or the global limit is the same).

Background contribution due to cosmogenic activation are:

- for ^{60}Co in the TeO$_2$ crystals $\sim 1 \cdot 10^{-4}$ cnts/(keV·kg·y);

- for ^{110m}Ag+^{110}Ag in the TeO$_2$ crystals $\sim 1 \cdot 10^{-3}$ cnts/(keV·kg·y);

- for ^{60}Co in the copper of the detector holder $< 5 \cdot 10^{-4}$ cnts/(keV·kg·y).

Results for surface contaminations are summarized in Tab. 3.4. Few remarks are important:

- in the case of TeO$_2$ crystals an exponential density profile with a depth ranging from 0.01 μm to 10 μm has been considered. Using the upper limits on the contamination intensities listed in Tab. 3.2 we obtain that the most dangerous contamination is that corresponding to a depth of 5 μm. The corresponding upper limit on the CUORE counting rate is evaluated;

- for copper two configurations are analyzed: the use of naked copper parts treated with the TECM procedure and the use of copper parts wrapped in a polyethylene film. In both cases the results obtained in the TTT measurement are extrapolated to CUORE, taking into account the different geometry (in CUORE the bolometers face about 2 times less copper area than in TTT) and the different energy region (the 3-4 MeV in the case of TTT and the ROI in the case of CUORE). While doing that, we ascribe to copper the whole 3-4 MeV counting rate recorded in the TTT measurement (as discussed in Section 3.1.3.2). For T1 (copper covered with polyethylene) this rate was obtained after the application of a single-hit cut to the data, that means that a fraction of crystal-induced events was removed. The same was not possible for T3 (since few detectors were active) and could be the reason for the slightly higher counting rate (see Fig. 3.5). Finally, in both cases we quote an upper limit because we are not able to disentangle the contribution given by crystals and/or PTFE spacers;

- for the PTFE, the PEN cables and the NTD thermistors, we apply a procedure similar to the one described for copper. Namely, we extrapolate to CUORE the 3-4 MeV counting rate recorded by detectors facing these components. In the case of PTFE the best measurement of PTFE-spacer induced background comes from TTT data. PTFE is expected to contribute in CUORE in the same amount as in TTT. Therefore the T1 result can be used to define an upper limit on PTFE-spacer contribution in CUORE. However in this case the extrapolation to CUORE does not take advantage of a sizably different geometry (as in the copper mounting structure case), therefore the limit on PTFE is poor. A higher sensitivity measurement of PTFE surface contamination is planned in the next future.

3.1.4.2   The far region: outside the Roman lead shield

Background contribution due to bulk contaminations in cryostat elements are summarized in Tab. 3.5.

QSHIELDS has been used for the study of the impact of cryostat parts on the detector counting rate. In this case a detailed description of the entire geometry of the cryostat, the dilution unit, the cables and all the ancillary parts is almost impossible. The geometry was simplified to include just the thermal shields, their plates and the inner lead shield. Only critical elements such as the calibration source insertion system were actually introduced in the simulation while for the other parts the simulation relied on the definition of the maximum integral activity allowed in the different volumes, see Tab. 3.6.

3.1.4.3   External background

The impact of environmental sources (muons, neutrons and gamma rays) on CUORE is discussed in [62]. In this case the LBE (Low Background Experiment) physics list was used. Results are summarized in Tab. 3.7. While dealing with external background it becomes important to consider the real feasibility of a global anticoincidence cut without introducing a too high dead time. Table 3.7 shows the different efficiencies of a global anticoincidence cut (the one used for all the sources discussed in previous sections) and a weaker cut based on nearest neighbor. In the case of external sources the difference is clearly important. However this is a peculiar characteristic of the sources here considered. The anticoincidence cut is extremely efficient for sources near to the detector, however for these sources near neighbor coincidences are dominating.

CUORE ROI - SURFACE CONTRIBUTIONS IN THE NEAR REGION

Element	ROI rate	Notes
	[cnts/(keV·kg·y]	
TeO$_2$ crystal surface	$<4 \cdot 10^{-3}$	upper limit due to poor statistics
Cu - TECM cleaning	$<3 \cdot 10^{-2}$	no crystal background subtraction (T3 data)
Cu - polyethylene wrapping	$<2 \cdot 10^{-2}$	partial crystal background subtraction (T1 data)
PTFE	$<6 \cdot 10^{-2}$	new measurement in progress
PEN cables	$<1 \cdot 10^{-3}$	new measurement in progress

Table 3.4: 90% C.L. upper limits on CUORE counting rate in the ROI from surface contamination. In the case of TeO$_2$ crystals, the real crystal surface contribution to the measured background is evaluated (the upper limit is due only to the low statistic collected in the CCVR measurement used to evaluate TeO$_2$ crystal surface contamination). In the case of copper, the evaluation of the surface contamination comes for the TTT data.. There it was not possible to disentagle the copper induced background from othe contributions like those due to crystal or PTFE. Only in the case of the copper wrapped with polyehtylene (T1) crystal surface contribution is partially removed thank to the use of the single-hit cut in T1 data analysis.

CUORE ROI - BULK CONTRIBUTIONS IN THE FAR REGION

Element	Material	ROI rate [cnts/(keV·kg·y)]
Cu TSP	NOSV Cu	$<4\cdot10^{-5}$
Cu 50 mK shield	OFE Cu	$<6\cdot10^{-4}$
Cu 600 mK shield	OFE Cu	$<6\cdot10^{-4}$
Cu 4 K shield	OFE Cu	$<1\cdot10^{-4}$
Cu 40 K shield	OFE Cu	$<4\cdot10^{-5}$
Cu 300 K shield	OFE Cu	$<1\cdot10^{-4}$
Cu plates from 10 mK to 40 K	OFE Cu	$<2\cdot10^{-5}$
inner Pb vessel	Roman Pb	$<4\cdot10^{-3}$
Pb top disk	Cometa Pb	$<5\cdot10^{-5}$
Fe 300 K plate	stainless Steel	$<3\cdot10^{-4}$

Table 3.5: 90% C.L. upper limits on CUORE counting rate in the ROI as obtained from bulk contaminations of elements belonging to the far region. In all these simulations only the 2615 keV line has been generated. This leads to an overestimation of the ^{232}Th contribution in the ROI since most of the coincidences are lost (therefore the single-hit cut has in the simulation an efficiency much lower than what expected).

3.2 Irreducible background

A background common to most calorimetric experiments for the search of neutrinoless double beta decay is the one generated by standard (two neutrinos) double beta decay. This phenomenon is always present when a double beta emitter is used, and it can be discriminated by the more rare and ineresting neutrinoless counterpart only based on topological features, that cannot be measured in a standard bolometric experiment. Due to neutrinos missing energy, the electrons summed spectra of the two neutrino double beta decay is continuous, starting from 0 and ending at the Q-value of the transition. For this reason, the high energy tail of the spectrum would partially overlap with the neutrinoless decay peak at the Q-value, generating an irreducible background whose importance depends on the energy resolution. Similarly, the low energy part of the spectrum generates a background for the phenomena with a low energy signature. In both cases, however, the extremely low decay rate and the fact that only the tails of the spectrum are considered make this background negligible.

CUORE MAXIMUM ACTIVITIES ALLOWED IN DIFFERENT REGION OF THE CRYOSTAT

Element	ROI rate for 1 Bq [cnts/(keV·kg·y)]
V1 (above the 300 K plate)	$<3 \cdot 10^{-11}$
V2 (between the 300 K and the 40 K plates)	$<3 \cdot 10^{-11}$
V3 (between the 40 K and the 4 K plates)	$<3 \cdot 10^{-11}$
V4 (between the 4 K and the 600 mK plates)	$<3 \cdot 10^{-11}$
V5 (between the 600 mK and the 50 mK plates)	$3 \cdot 10^{-11}$
V6 (between the 50 mK and the 10 mK plates)	$9 \cdot 10^{-7}$
Surface of the 40 K shield (superinsultation)	$1.4 \cdot 10^{-3}$
Surface of the 4 K shield (superinsultation)	$1.9 \cdot 10^{-3}$

Table 3.6: Background counting rate in the ROI for a 1 Bq activity of any material introduced in one of the 6 volumes indicated in Fig. 3.1 and for the two thermal shields that will be covered with the superinsulation. For the most external volumes (V1 to V4) only upper limits on the rate are available. In the two lowest row we report the rate induced by a 1 Bq activity on the surface of the two shields that will be covered with the thermal superinsulation.

CUORE ROI - BULK CONTRIBUTIONS FROM EXTERNAL SOURCES

Source	Total	Anti-coinc. (Global)	Anti-coinc. (Near neighbor)
Gamma	<0.390	<0.390	<0.390
Neutron	0.270 ± 0.022	$(8.56 \pm 6.06) \times 10^{-3}$	0.0642 ± 0.0442
Muon	17.3 ± 0.3	0.104 ± 0.022	1.850 ± 0.049

Table 3.7: Background in the ROI obtained by simulations of the evaluated gamma, neutron and muon fluxes at LNGS. Quoted errors are statistical only. Units are: $(counts \cdot 10^{-3})/(kg \cdot keV \cdot y)$. Limits are given at 90% C.L. Table from [62]. Note that here the ROI is 40 keV wide.

3.3 Low energy background

As the main goal of the CUORE experiment is the search for neutrinoless double beta decay in the energy region around 2.5MeV, the largest efforts have always been addressed to the reduction the background in this region of the spectrum. Moreover, the low energy region (below few tens of keV) of TeO_2 bolometers has never been studied until very recent times because the high level of thermal and elecronic noise prevented the trigger threshold from being lowered. Starting from the last few runs of CUORICINO ([56]) experiment, however, the new DAQ and analysis hardware and software tools, developed for CUORE (see Section 1.4), have been applied to all the data of the bolometric runs with TeO_2 performed both in Hall A and in test facility in Hall C of LNGS. This tools, together with the development of a new PTFE holders design that reduced the vibrational noise in the detectors, pushed the energy threshold of some bolometers down to few keV. This improvement of the performance opened the possibility of studying the background also at low energy.

The data from which most of the information can be extracted are the CCVR2 test run, in the Hall C test facility at LNGS ([9, 31]) and the ones from the last months of CUORICINO ([31]).

In Fig. 3.6 the energy spectra – between threshold and 40keV – of CUORICINO and CCVR2 are compared. Some features are worth being commented:

- both spectra are scaled for the mass and live time of the measure and thus can be directly compared; the only difference is that CCVR2 data are corrected for the detection efficiency that is estimated by means of a pulser signal at low energy,
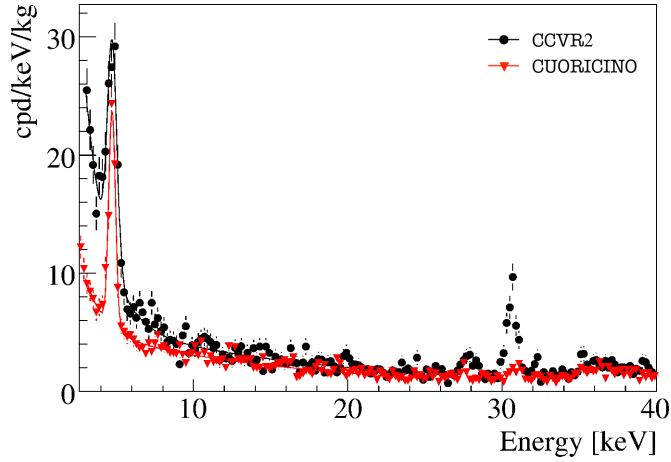
Figure 3.6: Comparison of CCVR2 (black circles) and CUORICINO (red triangles) data.

which was not present in CUORICINO; CUORICINO spectrum should, then, be reduced by a factor between 0.8 and 0.9 (assuming the same efficiency measured in CCVR2);

- CCVR2 spectrum shows a peak at 30.5keV that is not present in CUORICINO data; it is associated with the K-line emission of the Sb which is produced by ^{121m}Te and ^{121}Te decaying via EC with half-lives of 154 and 17 days respectively. ^{121m}Te and ^{121}Te, like other Te metastable isotopes with shorter half-lives, are produced within the crystals by cosmogenic activation during production and shipment outside the underground laboratories. In CUORICINO the peak disappeared because all the nuclei decayed away during the 5-year underground data taking;

- both CCVR2 and CUORICINO data show a peak caracterized by a compatible activity and an energy of 4.7keV. Even if this energy corresponds to the L_1 atomic shell of Sb, its intensity is much higher than what could be explained considering this source only. Moreover, its rate proved to be constant during more than 20 days of measurement, excluding any link to short-lived metastable isotopes of cosmogenic origin. The origin of this peak is still unknown ([31]). Although a very interesting puzzle, the presence of this peak has little to no effect on the background for what concerns the present study, where the global rate of background events is of greater interest than their energy distribution; the fraction of the total

number of background events between the threshold and some tens of keV that is contained in the peak is, in fact, small, and can be safely neglected;

- compared to CUORICINO, the background rate in CCVR2 has the same behavior at energies greater than 10keV, but is considerably higher at lower energies. This difference is not yet completely understood, but a possible explanation resides in the fact that the Hall A cryostat, where CUORICINO was run, features a lower background compared to Hall C cryostat at high energy. The following interpretation is then possible. If one considers that the continuous components of the high energy background are usually associated with degraded alpha or multi-compton events, a plausible argument is that single hit events with small energy can be generated when it is the high energy counterpart that is missing. In this case, a relation is very likely to exist between the low energy counting rate and the activity of higher energy background sources. For this reason, the CUORE background is assumed, whith high confidence, not to be higher than the CCVR2 one, that can be fitted, neglecting the 4.7keV peak, by a double exponential model.

3.4 Active background rejection in TeO$_2$ bolometers: the ABSURD project

As already discussed in the previous section, the low energy background is likely to be strongly correlated to the background at higher energy (namely in the double beta decay ROI). For this reason strong efforts are constantly made in the monitoring and suppression of the radioactive contaminations in the detector. In the previous section the fact was also discussed, that the low energy events laying in the continuum at low energy can be associated to higher energy particles that, after loosing almost all their energy in active or passive elements of the detector, interact with the bolometers releasing only few keV. This very same events are dangerous in the $\beta\beta$ ROI if the original energy of the particle is larger than the $\beta\beta0\nu$ Q-value. As explained before in this same chapter, a strong signature of a degraded background arising from crystal contaminations is the simultaneous firing of two facing detectors (a double-hit event); an anticoincidence cut, that considers an event only if a single crystal at a time is involved, is therefore very effective in reducing the effect of all the contaminations in the bulk or on the surface of a crystal when the radiation releases energy in at least two crystals. Whenever the radioactive contamination resides in – or on the surface of – a passive element of the detector, however, the anticoincidence cut turns out to be ineffective. This makes any radiation with an energy larger than the ROI a potential

source of background: if the $\beta\beta$ ROI is considered, this corresponds to the degraded alpha background already described; if the low energy ROI for the study of supernova neutrinos is considered, any radiation is virtually a candidate as background source (see Fig. 3.7).
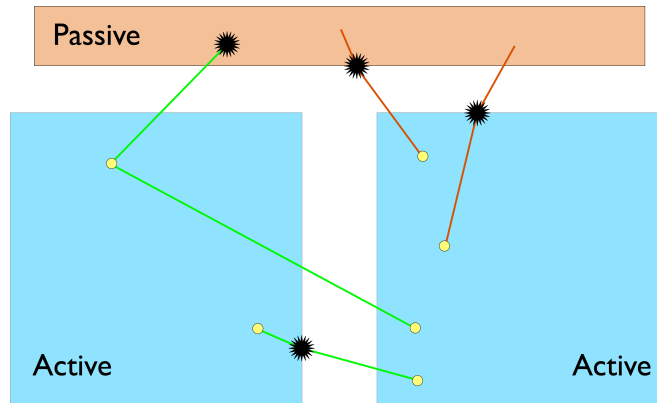
Figure 3.7: Sketch of the possible configurations leading to a degraded background. Green: two (or more) crystals are involved and the event can be rejected with an anti-coincidence cut. Red: only one crystal is hit by the particle, but only a fraction of the energy is deposited; depending on the amount of energy lost in the passive element, the event will fall in a different region of the energy spectrum; only radiation with a starting energy larger than the ROI is dangerous. This background cannot be rejected by means of an anticoincidence operation mode of adjacent crystals.

A possible solution to this double-faced problem is investigated by the ABSURD (A Background SUrface Rejection Detector) project. ABSURD main goal is to demonstrate the feasibility of an ibrid TeO$_2$ bolometric detector that exploits a foil of scintillating plastic material that surrounds the crystal to tag, through the light emission, any ionizing radiation that hit the detector, generated outside the sintillating layer itself. A sketch of the concept is reported in Fig. 3.8.

A thin layer of light scintillating material surrounds the TeO$_2$ crystal, defining a volume that, ideally, should contain only the active elements of the detector. Any passive element (copper, PTFE holders, cabling system) should lay outside this volume. In this way, any radiation produced on the surface of a passive element is forced through the scintillating material before hitting the bolometer. Any energy deposition in the scin-
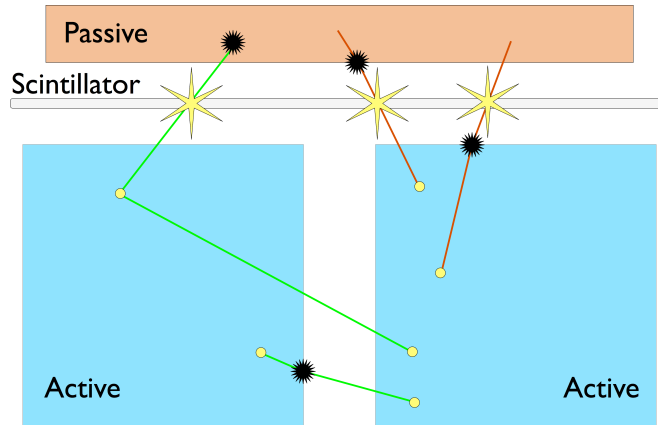
Figure 3.8: The same background sources configurations of Fig. 3.7 are depicted, but the ABSURD scintillator foil is added; the red trajectories now intercept the scintillator that is optimized for highly ionizing alpha particles; the scintillation light, detected by a bolometric light detector, replace the passive element in the double-hit cut.

tillating layer induces the emission of scintillation light, whose amount is proportional to the amount of deposited energy and largely depends on the particle type, namely on its stopping power (dE/dx). If a light detector is added to the setup, the external background can be suppressed by rejecting any event where both the TeO$_2$ bolometer and the light detector fired simultaneously.

3.4.1 Scintillating foil

The light yield of scintillating materials is, in almost the totality of the cases, inversely proportional to the stopping power, meaning that more ionizing particles, like alphas pr heavy ions, produce less scintillation light for a given amount of energy released in the scintillator compared to electrons. For this reason scintillators are usually considered well suited for the detection of γ/β radiation. The most dangerous background that should be reduced by ABSURD is, however, generated by degraded α particles. This means that the choice of the scintillating material is critical and commercially available products are, in general, not the optimal solution. Moreover, the behavior of plastic scintillators in the mK temperature range has never been extensively studied. For these reasons two research lines presently exist on this topic within the ABSURD project:

- the study of custom-made plastic scintillators, to be produced in thin foils with spinning method ([63]), optimized for alpha particles, is being performed in collaboration with a Brookhaven National Laboratory specialized group. Some preliminary results are available: thin films of THV (a terpolymer of Tetrafluoroethylene-Hexafluoropropylene-Vinylidene Fluoride) with PC (1,2,4-trimethylbenzene, or Pseudocumene) scintillator and PPO (2,5-diphenyloxazole) wavelength shifter have been produced with thickness up to 60μm and their optical and mechanical properties have been tested to liquid nitrogen temperature, showing that they remain almost unchanged;

- the study of scintillator foils optical properties, light yield and emission spectrum at cryogenic temperature, down to few Kelvin. For this purpose two setups are being prepared: at LNGS a cryogenic-free cryostat has been designed and built; it will be able to host scintillator samples, alpha sources and silicon photo-multipliers to study the light yield down to about 20K. At Milano-Bicocca a cryostat based on helium pumping with an optical window will perform the same measurements, on pre-selected samples, between 4K and 1K.

In order to estimate the target light yield of the studied materials, few considerations are needed. As already stated, the most important background to be rejected are alpha particles that release a fraction of their energy in passive materials and hit the crystal with an energy of about 2.5MeV, i.e. in the double beta decay ROI. As widely studied and discussed (Section 3.1.1), the main alpha sources that are ususally measured with cryogenic detectors generate alphas with an energy of at least 4MeV (lowest peaks in the ^{232}Th chain). This means that, to fall in the ROI, they have to loose about 1.5MeV in passive elements of the detector setup. This is, therefore, the minimum amount of energy that should be detected by the scintillator/light detector system. As a first consequence, the scintillating foil must be thick enough to let an alpha particle release 1.5MeV when flying through it; this corresponds, given alpha particles range and plastic scintillators density (that is very close to water density), to a thickness much smaller than 50μm. For what concern the light yield, let's assume to use a light detector with a threshold, $E_{\text{threshold}}$, of 100eV (that have been reached with more than one germanium light detector in R&D tests). Considering the total efficiency ϵ (Eq. 3.4), the minimum amount of produced light that can be detected is

$$E_{\text{min}} = \frac{E_{\text{threshold}}}{\epsilon} \, , \tag{3.2}$$

91

from which we deduce that the light yield of the scintillating foil must not be smaller than

$$LY_{\min} = \frac{E_{\min}}{1.5\text{MeV}} = \frac{100\text{eV}}{\epsilon \times 1.5\text{MeV}} \tag{3.3}$$

or $\sim (67/\epsilon)$eV per MeV. It is worth noting that this value is very reasonable and conservative: commercial scintillators (BC-400 from Saint-Gobain, for example) produce $\mathcal{O}(1000)$ photons per MeV for alpha particles, corresponding to ~ 2.5keV, a value that would guarantee the detection even with small light collection and detection efficiencies.

3.4.2 Light detector

A critical element of the ABSURD setup is the light detector. It is responsible for the detection of the light produced by the background-producing particle that interacts in the scintillating foil. It should feature the following properties:

- working temperature – the scintillator will be mounted as close to the TeO$_2$ detector as possible, meaning that the light source is located in a low temperature environment. Two possibilities exist: the light is propagated outside the cryostat by means of a light guide or the light detector is also operated at the base temperature. The latter solution is in general preferred and already used in a number of hybrid bolometric experiments ([64, 65]). By putting the detector sensitive element close to the light source, the detection efficiency is maximized and any loss of light due to absorption in the light guide or reflection at the interface between elements of the system can be avoided. Moreover, the heat load that would be induced on the cryogenic system by the presence of bulky light guides running from ambient to base temperature is also eliminated. The drawback is that the light detector must work at the same temperature of the TeO$_2$ bolometer, i.e. it must be a bolometer itself;

- detection efficiency – the ratio between the number of the detected photons and the number of the ones produced by the light source (the scintillator) defines the total efficiency of the light detection system. It can be expressed as the product

$$\frac{N_{\text{detected}}}{N_{\text{produced}}} = \epsilon = \epsilon_C \epsilon_D \tag{3.4}$$

where ϵ_C is the collection efficiency, while ϵ_D is the detection efficiency. The former is the probability that a photon, emitted where the particle trajectory intercepts the scintillating foil, reaches the light detector surface without being absorbed when reflecting or propagating through the different detector elements surfaces. ϵ_C can be maximized by carefully designing the relative position of the various

elements, eventually adding reflecting surfaces outside the volume defined by the scintillating foil and maximizing the transimission of the light, also shifting its wavelength, if necessary, depending on the scintillation light spectral properties. ϵ_D is the probability that a photon that reaches the surface of the light detector is actually absorbed in it, depositing its energy, and not reflected or transmitted. This parameter depends on the matching between the scintillator emission and detector absorption spectra. They can be, within certain limits, adapted to obtain a maximum overlap. For what concerns the light detector, the absorption specrum mainly depends on the material; for a given material, however, surface treatments can be applied to maximize ϵ_D given the emission spectrum of the scintillator.

- energy threshold – a critical point for the effectiveness of the ABSURD concept is the minimum amount of light that can be detected. It fixes, given the already cited efficiencies and the scintillator light yield, the minimum amount of energy that the α particles must release in the scintillator to be tagged; the lower the light detector threshold is, the less stringent will be the requirements on the efficiencies and the light yield. A suitable light detector must therefore tipically feature an energy threshold of the order of 100eV.

An effective combination of these features is found in small bolometers, that are often used as light detectors for low temperature applications. These bolometers are usually thin disk-shaped slabs to minimize the mass and the heat capacity thus increasing the sensitivity. Typical materials used for the construction of bolometric light detectors are germanium, silicon or sapphire. They usually feature a read-out system similar to the one used in all bolometric detectors with a thermometer that measures the temperature variation induced by the interaction of photons.

A part of ABSURD R&D activity consists in the development of a new kind of bolometric light detectors featuring improved performance in terms of energy threshold and reproducibility. One of the main issues with bolometric detectors is the fact that the energy threshold is a hardly reproducible parameter. This is true also for light detectors, where the reproducibility of the energy threshold is a key element. This problem is connected with the reproducibility of the method used to couple the bolometer absorber and the temperature sensor.

In CUORE this coupling is provided by epoxy glue, but the actual volume of glue and the shape of glue spots are parameters that can vary from one detector to the other. To overcome this problem a new concept was developed: the basic idea is to remove the coupling element (the glue) between the absorber and the sensor. The temperature sensitive element must be a part of the absorber itself. In other words, the sensitive

element is a part of the absorber volume that has been modified to feature a dependence of its resistance on the temperature. This condition can be achieved if the absorber is a semiconductor; temperature sensitive elements used in bolometric detectors are in fact (see Section 1.1.2) semiconductors (usually germanium or silicon) whose doping level is tuned in order to keep their conductive properties in a range where the resistence strongly depends on the temperature. If germanium is used, the best tuning is achieved using neutron transmutation doping at nuclar reactors. This technique allows a fine control on the doping levels; among the drawbacks, however, there is the fact that the whole volume is exposed to the neutron flux and therefore reaches the same doping level. If silicon is used, on the contrary, the needed doping is obtained by ion implantation. This process allows to control the spatial features of the implant, that can be localized in a defined region of the silicon substrate. For this reason, the ABSURD light detectors will be developed based on high resistivity silicon substrate. The sketch of the working principle is depicted in Fig. 3.9.
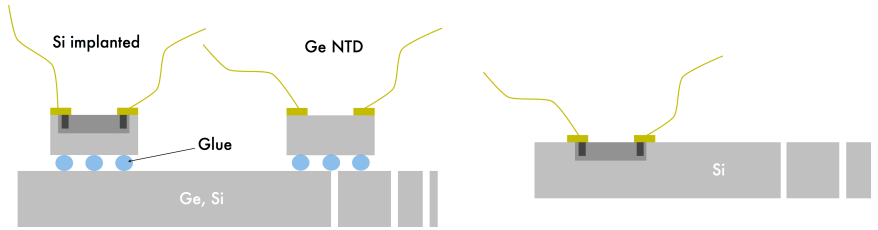
Figure 3.9: Left: classical termistor+absorber configuration of bolometric light detectors. Right: concept of monolithic light detectors for ABSURD. The sensitive element is directly implanted in the silicon absorber lattice.

By means of a ion implantation process, one or more small regions of the silicon slab can be doped to the desired level and superconductive contacts and trays can be deposited on the surface to ensure the readout of the thermistors. With the same technique the heater can also be implanted directly in the absorber lattice.

Since the implantation is a well known industrial process widely used in semiconductor industry, its reproducibility is much higher than any glue-based coupling between sensor and absorber. The effects of having the sensitive element embedded directly into the absorber lattice are still under study; the main difference between a classical system and this *monolithic* detector is the lack, in the latter, of any interface between the sensor and the absorber. In standard bolometers, the glue, while providing the mechanical

coupling, also ensures the thermal coupling and is responsible for the propagation of the heat form the absorber to the sensor. Since it is an amorphous material, only thermal signals can propagate through it, while any non-thermal component of the phonon spectrum is quickly thermalized in an amorphous element. On the contrary, in the monolithic bolometer there is no mechanical discontinuity between the sensor volume and the absorber because they share the same crystalline lattice. A non-thermal phonon has therefore the same probability of thermalizing in the sensor or in any equivalent volume of the absorber. Moreover, any thermal component is immediately sensed by the thermistor without the need of heat propagation through the amorphous interface. Therefore, the main effects that are expected from the point of view of the detection capabilities are:

- lower energy threshold; in mechanically coupled absorber-sensor systems, the amplitude of the signal recorded by the sensor directly depends on the ratio between the strength of the coupling between the sensor and the absorber and the strenght of the coupling of the absorber to the heat bath: it is demonstrated that a smaller sensor-absorber impedence (that can be obtained, for example, by increasing the surface of the glue spots interface) ensures larger signals for a given energy deposition. In a monolithic light detector, this impedence is completely removed because the thermistor lattice and the absorber lattice are the same, thus always sharing the same thermal phonon spectrum and temperature. It is therefore expected that the amplitude of the signal induced by the thermal component of the phonon spectrum is maximum in this configuration;

- strong dependence of the signal on the position of interaction; as already said, there is, in this case, the possibility that a non-thermal phonon interacts in the sensor lattice because of the lack of a coupling that ensures the thermalization of the phonon spectrum. The interaction of a non-thermal phonon in the sensitive volume generates a pulse whose amplitude and shapes are expected to be completely different from the thermal pulses. Moreover, the probability of detecting a non-thermal photon geometrically depends, given the mean free path of the non-thermal phonon in the lattice, on the distance between the sensor and the point where the particle interacted producing the non-thermal phonons. The amplitude of the pulse generated by non-thermal phonons is therefore expected to contain information on the position of the interaction. The simultaneous reading of multiple implanted sensors should allow the reconstruction of the interaction position. It is worth noting that, in general, a light detector is supposed to detect a light signal that is composed by multiple photons (see Section 3.4.1 for an estimation

of their number); in this case the effect of the position dependence is expected to be averaged out and the differences among the signal amplitudes on different sensors should be reduced.

The development of the light detectors for ABSURD is responsability of Milano-Bicocca Physics Department in collaboration with the FBK (Fondazione Bruno Kessler) foundation in Trento, specialized in the research on semiconductor technological applications. The development, production and test is divided in various phases. The first phase, consisting in the selection of the substrate, and the second phase, consisting in the study of different surface coatings to maximize the detection efficiency of scintillation photons, are presently in progress at Milano-Bicocca cryogenic laboratory. The third phase of the project will consist in the production of silicon slabs with the selected coating and implanted thermistors with different doping levels in order to select and tune the best performing parameters, and better understand the behavior of this monolithic solution.

3.4.3 Demonstrator run

In order to study the feasibility of the ABSURD concept, a demonstrator cryogenic run has been projected and realized and is taking data in the Hall C test facility at LNGS. The main goal of the run is to show, with a non-optimized scintillating foil and light detector, the potential of the system in tagging and rejecting ionizing particles (α) that are generated outside the volume, defined by the scintillating surfaces, containing the detector. In the demonstrator run the main detector is a $3 \times 3 \times 3\text{cm}^3$ TeO$_2$ crystal equipped with an NTD thermistor and a Si heater. It is held in position by four PTFE holders inside a box-shaped structure made of copper foils. The top face of the box is replaced by a germanium light detector with a standard NTD thermistor and Si heater. In this run each one of the five copper faces is covered with commercial scintillating foil (Saint-Gobain BC400 series), but the structure is designed to host any scintillating foil that will be produced and will need to be tested in the future. The four lateral copper faces are connected to the copper base of the structure by means of four grooves; at their upper end, the lateral faces are held in position by a square frame that also contains the copper connectors for the thermistors and heaters read-out/bias. The technical drawings of the assembly are reported in Fig. 3.10.

In this run an alpha source was prepared to test the effectiveness of the background rejection by relaying on a known source that should mimic the most dangerous background, i.e. degraded alpha particle that hit the TeO$_2$ crystal with an energy smaller than the emission one. A source of uranium in liquid acid solution (containing both ^{238}U and ^{235}U, with alphas energies of 4.198MeV and 4.398MeV respectively) was deposited
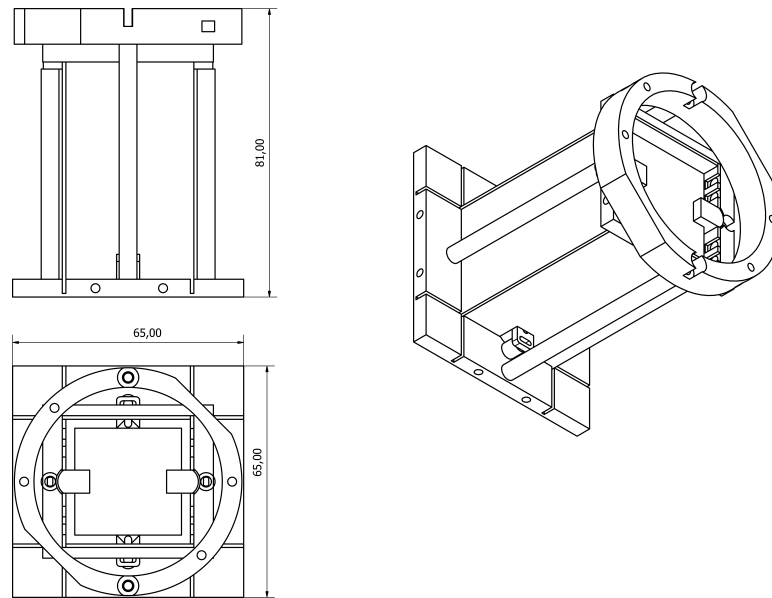
Figure 3.10: Drawings of the ABSURD first demonstrator run with $3 \times 3 \times 3 \text{cm}^3$ TeO$_2$ crystal; the circular frame on top of the detector is the holder of the Ge light detector, not represented in this drawings.

on the surface of the crystal, facing the scintillating foil. Since the solution containing the source is slightly acid, it partially diffuses inside the crystal. The emitted alpha thus releases a fraction of its energy in the crystal before leaving it and hitting the scintillating foil. The relative fraction of energy deposited in each element depends on the depth at which the alpha is emitted in the crystal that, in turn, depends on the diffusion profile of the source.

The main goal of the measurement is to show that those alphas that release only about 2.5MeV in the crystal produce enough light in the scintillating foil to be detected and tagged with the light detector, and measure the efficiency of this rejection system. The ABSURD roadmap foresees that the system is then upgraded with an optimized scintillator and more sensitive and reproducible light detectors.

Chapter 4

Supenova signal calculation

In order to evaluate the potential of CUORE as an observatory for supernova explosions, the expected number of detectable events induced by supernova neutrinos in the detector has to be calculated. From the knowledge of the models describing the physics phenomena that occur during a supernova explosion (Section 2.3) the properties of the neutrinos emitted by a supernova can be extrapolated. The mechanism of interaction of these neutrinos in the detector is also known: the neutrino interacts via neutral current coherent scattering with a nucleus in the target material transferring part of its energy to the nucleus itself. In the bolometer lattice the kinetic energy of the recoiling nucleus, whose recoiling movement is completely negligible both from space and time point of view, is quickly converted into heat and a rise in the absorber temperature is measured. Since the ultimate phenomenon that is detected is simply the recoil of the nucleus, a NCCS neutrino interaction is indistinguishable from any other particle interaction in the bolometer (unless a method for the discrimination of the interacting particle is developed for TeO_2 crystals, see Section 3.4). The number of detectable supernova neutrinos is then equal to the number of neutrino interactions in which enough momentum was transferred to the nucleus to make it recoil with enough energy to be triggered by the acquisition system. The performance of the detector in terms of energy threshold is therefore as important as many other experimental parameters like the total target mass, the target composition, the pile-up rejection capability and, of course, the background the signal has to be compared with.

The ingredients that are needed to calculate the neutrino events yield, i.e. the above mentioned number of nuclear recoils induced by a NCCS neutrino interaction, are:

- the neutrino time-integrated flux, i.e. the number of neutrinos produced by a supernova explosion that flow through a surface of unit area once they reach

the Earth integrated over the emission time (this is used to calculate the total number of events that can be associated to a supernova explosion, even if the trigger algorithm will exploit the time distribution of the events to increase the sensitivity). It depends, of course, on the distance between the emission point (the supernova) and the detector with the simple inverse squared distance law:

$$\phi(E) = \frac{\tilde{\phi}(E)}{4\pi d^2} \tag{4.1}$$

where $\tilde{\phi}(E)$ is the time-integrated flux emitted at the source and is simply the total number of neutrinos emitted during the whole explosion in all directions, while d is the distance of the supernova. In the numerical calculations that are reported in the following a distance $d = 8.5\text{kPc}$ is used. This choice is justified by the probability distribution of a supernova explosion occurence within our galaxy and is shown in more detail in Section 2.3. A detailed study of the sensitivity of CUORE as a function of the supernova distance is performed in Section 4.3 and Chapter 5.

Since the mechanisms that are responsible for the emission of the different neutrino species (Section 2.3.1) are different and can occur in regions of the supernova where the temperature is different, at least three different spectra should be considered and the flux $\tilde{\phi}$ can actually be expressed in terms of three different quantities $\tilde{\phi}_i$, where i can be electron neutrinos, ν_e, electron anti-neutrinos, $\bar{\nu}_e$, or all the other families, i.e. muon and tau neutrinos and antineutrinos that all interact with the same processes with the standard (electronic) matter which composes the supernova (ν_x). From Section 2.3.2

$$\tilde{\phi}_i(E) = \frac{N_i}{2T_i^3} E^2 \exp\left(-\frac{E}{T_i}\right) ; \tag{4.2}$$

- the neutral current coherent scattering cross section $\mathrm{d}\sigma_{\mathrm{NCCS}}/\mathrm{d}\Omega$ already derived in Section 2.3.2; it depends on the scattering angle θ between the direction of the incoming neutrino and the direction of the neutrino after the interaction and can be written as:
$$\frac{\mathrm{d}\sigma_{\mathrm{NCCS}}}{\mathrm{d}\Omega} = \frac{G_F^2}{4\pi^2} E^2 (1 + \cos\theta) \frac{Q_w^2}{4} F(Q^2)^2 ; \tag{4.3}$$

- the form factor $F(Q^2)$ that appears in the cross section and accounts for the dependance of its magnitude on the momentum transfer Q, as explained in Sec-

100

tion 2.3.2, where it is also defined as:

$$F(Q^2) = \frac{3 \left(\frac{\sin(QR_0)}{(QR_0)^2} - \frac{\cos(QR_0)}{QR_0} \right)}{QR_0} \times \exp \left(-\frac{(Qs)^2}{2} \right) \qquad (4.4)$$

where R_0 is the nuclear radius defined as

$$R_0^2 = R^2 - 5s^2$$

$$R = (1.2 \times A^{1/3}) \text{fm}$$

and s the skin thickness (0.5fm).

4.1 Signal derivation

The above mentioned ingredients are put together to obtain the event yield, i.e. the number of neutrino interactions in the detector, as a function of the recoil energy of the scattered nucleus only. The dependance on the scattering angle and the neutrino energy are removed by integrating over these variables:

$$Y(T) = \frac{\mathrm{d}N}{\mathrm{d}T} = N_t \iint \mathrm{d}\Omega \mathrm{d}E \frac{\mathrm{d}\sigma_{\mathrm{NCCS}}}{\mathrm{d}\Omega} (Q^2, F(Q^2), Q_W^2, A) \, \phi(E) \, \delta \left(T - \frac{Q^2}{2M} \right) \qquad (4.5)$$

By inserting the explicit form of the cross section of Eq. 4.3 and $\mathrm{d}\Omega = \sin(\theta)\mathrm{d}\theta\mathrm{d}\varphi$ we get

$$Y(T) = N^{\mathrm{tot}} \int \mathrm{d}\varphi \iint \mathrm{d}\theta \mathrm{d}E \sin(\theta) \frac{G_F^2}{4\pi^2} E^2 (1 + \cos(\theta)) \frac{Q_w^2}{4} F(Q^2)^2 \phi(E) \delta \left(T - \frac{Q^2}{2M} \right) . \qquad (4.6)$$

It is easy to demonstrate that the relation between the incoming neutrino energy, the momentum transfer of the interaction, the scattering angle, the target mass and the recoil energy of the scattered nucleus is

$$2MT = Q^2 = 2E^2(1 - \cos(\theta)) , \qquad (4.7)$$

and that, using the composition rule of the delta distribution[1] we can write the equality

$$
\begin{aligned}
\delta\left(T - \frac{Q^2}{2M}\right) &= 2M\delta\left(2MT - Q^2\right) \\
&= 2M\delta\left(2E^2(1 - \cos(\theta)) - Q^2\right) \\
&= 2M\left[4\frac{Q}{\sqrt{2(1 - \cos(\theta))}}(1 - \cos(\theta))\right]^{-1}\delta\left(E - \sqrt{\frac{MT}{1 - \cos(\theta)}}\right)(4.8)
\end{aligned}
$$

By using Eq. 4.8 in Eq. 4.6 we can rewrite the cross section as

$$
Y(T) = N^{\text{tot}}\int \mathrm{d}\varphi \iint \mathrm{d}\theta\mathrm{d}E \sin(\theta)\frac{G_F^2}{4\pi^2}E^2(1 + \cos(\theta))\frac{Q_w^2}{4}F(Q^2)^2\phi(E) \times
$$
$$
\times 2M\frac{\sqrt{2(1 - \cos(\theta))}}{4Q(1 - \cos(\theta))}\delta\left(E - \sqrt{\frac{MT}{1 - \cos(\theta)}}\right) \qquad (4.9)
$$

that, using the kinematics equivalences of Eq. 4.7 and removing the constants from the integrals, becomes

$$
Y(T) = \frac{N^{\text{tot}}G_F^2 Q_w^2}{32\pi^2}\sqrt{\frac{M}{T}}F(2MT)^2\int \mathrm{d}\varphi \iint \mathrm{d}\theta\mathrm{d}E \sin(\theta)\frac{1 + \cos(\theta)}{\sqrt{1 - \cos(\theta)}} \times
$$
$$
\times E^2\phi(E)\delta\left(E - \sqrt{\frac{MT}{1 - \cos(\theta)}}\right) . \qquad (4.10)
$$

The integration over φ is trivial because the cross section doesn't depend on it, leading to a 2π factor. The integration on E is also simple thanks to the delta function:

$$
Y(T) = \frac{N^{\text{tot}}G_F^2 Q_w^2}{16\pi}M\sqrt{MT}F(2MT)^2 \times
$$
$$
\int \mathrm{d}\cos(\theta)\frac{1 + \cos(\theta)}{(1 - \cos(\theta))\sqrt{1 - \cos(\theta)}}\phi\left(\sqrt{\frac{MT}{1 - \cos(\theta)}}\right) . \qquad (4.11)
$$

To summarize, the elements composing the constant part of the event yield are: the Fermi constant G_F, the weak charge Q_w, the target nucleus mass M and the total number of target nuclei present in the detector N^{tot}. Since the material used as a target can in general - and is in the case of CUORE - be composed by several different atomic species, a more general notation can be used to take into account the fact that

---

[1] If $g(x)$ is a continuously differentiable function with a real root at x_0, then it holds

$$
\delta(g(x)) = \frac{\delta(x - x_0)}{|g'(x_0)|} .
$$

an event yield can be calculated for each different element composing the detector:

$$Y_\alpha(T) = \frac{N_\alpha^{\text{tot}} G_F^2 Q_{w_\alpha}^2}{16\pi} M_\alpha \sqrt{M_\alpha T} F(2M_\alpha T)^2 \times$$

$$\int d\cos(\theta) \frac{1 + \cos(\theta)}{(1 - \cos(\theta))\sqrt{1 - \cos(\theta)}} \phi\left(\sqrt{\frac{M_\alpha T}{1 - \cos(\theta)}}\right). \qquad (4.12)$$

In Eq. 4.12 the index α runs over the different elements composing the detector; in the case of CUORE the target is tellurium dioxyde, therefore $\alpha = O, Te$. N_α^{tot} is the total number of nuclei of the element α that are present in the meterial, hence:

$$N_\alpha^{\text{tot}} = \frac{m_{\text{detector}}}{\sum_\alpha A_\alpha \eta_\alpha} N_A \eta_\alpha \qquad (4.13)$$

with A_α the atomic mass (the weighted average over the various isotopes can be considered without loosing generality), η_α the stoichiometric ratio of the corresponding atom and N_A Avogadro's number. As already shown (Eq. 4.2) a different spectral shape should be considered for the flux of each neutrino specie; a further index i should therefore be added to the yield to account for the number of events that are ascribable to a specific kind of neutrino, obtaining

$$Y_{\alpha,i}(T) = \frac{N_\alpha^{\text{tot}} G_F^2 Q_{w_\alpha}^2}{16\pi} M_\alpha \sqrt{M_\alpha T} F(2M_\alpha T)^2 \times$$

$$\int d\cos(\theta) \frac{1 + \cos(\theta)}{(1 - \cos(\theta))\sqrt{1 - \cos(\theta)}} \phi_i\left(\sqrt{\frac{M_\alpha T}{1 - \cos(\theta)}}\right). \qquad (4.14)$$

Finally, the total number of interacting neutrinos can be expressed as the sum of the yields for the single elements and neutrino species:

$$Y(T) = \sum_{\alpha = \text{O,Te}} \sum_{i = \nu_e, \bar{\nu}_e, \nu_x} Y_{\alpha,i}(T). \qquad (4.15)$$

$Y(T)$ still contains the integrals of the neutrino fluxes over the angular variable θ; even if for some shapes of the neutrino spectrum the integral can be calculated analytically, a numerical integration is much more flexible and allows the calculation of the total yield with any possible spectral shape, even if an analytical form cannot be derived. For the numerical integration the software *Mathematica* has been used; the specific method used for the integration turned out to be irrelevant when the results were compared. Performing the integration with the fluxes of Eq. 4.2 the results shown in Fig. 4.1 were obtained: the differential spectra are reported as a function of the energy of the recoiling

nucleus, which is all the energy released in the detector by the interacting neutrino and hence the signal recorded by the bolometer.
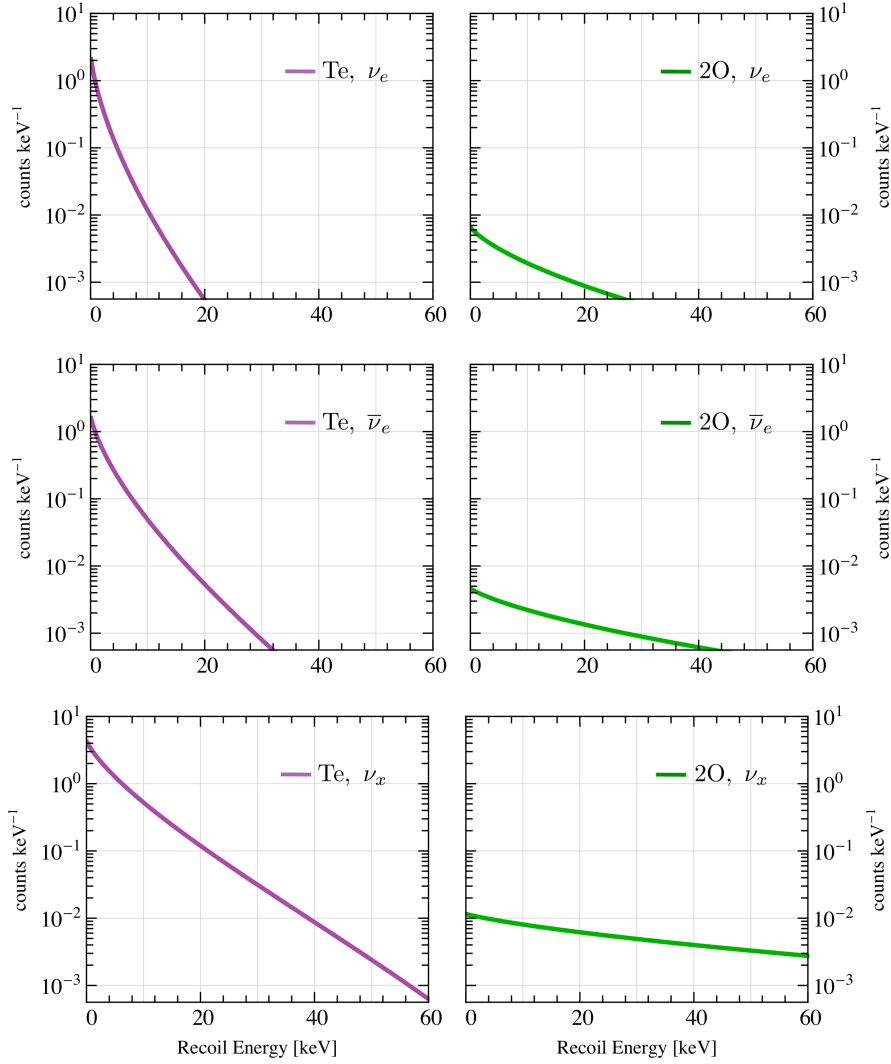

Figure 4.1: Energy spectra of nuclear recoils induced on the different target nuclei (tellurium and oxygen) by the three different neutrino species.

The differences between the specra corresponding to the recoil of tellurium or oxygen nuclei are evident: the number of events in the oxygen spectra is much smaller, due to the smaller cross section. As it is explained in Section 2.3.2 the NCCS cross section depends on the square of the weak charge Q_w of the nucleus, which is

$$Q_w = N - (1 - 4\sin^2\Theta_W)Z \;. \tag{4.16}$$

Since $\sin^2\Theta_W \approx 0.231$, Eq. 4.16 is almost

$$Q_w \sim N \tag{4.17}$$

and therefore the cross section depends almost only on the squared number of neutrons in the nucleus. Since the number of neutrons in the tellurium nucleus is about a factor 10 larger than the number of neutrons in oxygen, the cross section for coherent scattering will be roughly two orders of magnitude larger.

Another effect that can be clearly seen in Fig. 4.1 concerns the spectral shape: the oxygen spectra show a larger fraction of the events at higher energy compared to the tellurium spectra. This is ascribable to two different factors: the first is, once again, one of the terms that compose the cross section, the nuclear form factor $F(Q^2)$. It accounts for the resolving power of the incoming neutrino; for the scattering to involve coherently all the nucleus components, the de Broglie wavelength associated to the momentum transferred during the interaction must be comparable or larger than the dimension of the target nucleus. Since tellurium nuclei are larger than oxygen ones the coherent interaction happens only for smaller momentum transfers and therefore the spectrum of tellurium recoils lacks in high energy events.

The other factor that contributes to the shift of the tellurium spectra towards lower energies compared to the oxygen ones is kinematic and trivially derives from Eq. 4.7 that can be written as

$$T = \frac{Q^2}{2M} \;; \tag{4.18}$$

the larger is the mass of the recoiling nucleus, the smaller is the kinetic energy that it acquires for a given momentum transferred during the interaction.

In Fig. 4.2 the total spectra for the two nuclei composing tellurium dioxyde are reported, obtained summing the spectra in the same column of Fig. 4.1.

In a similar way in Fig. 4.3 the two spectra coerresponding to tellurium and oxygen are summed to obtain the total spectrum. This is the spectrum that the experiment would observe: the flavour of the interacting neutrino cannot be identified in coherent scattering, indeed, and TeO_2 bolometers are not able to distinguish between a tellurium
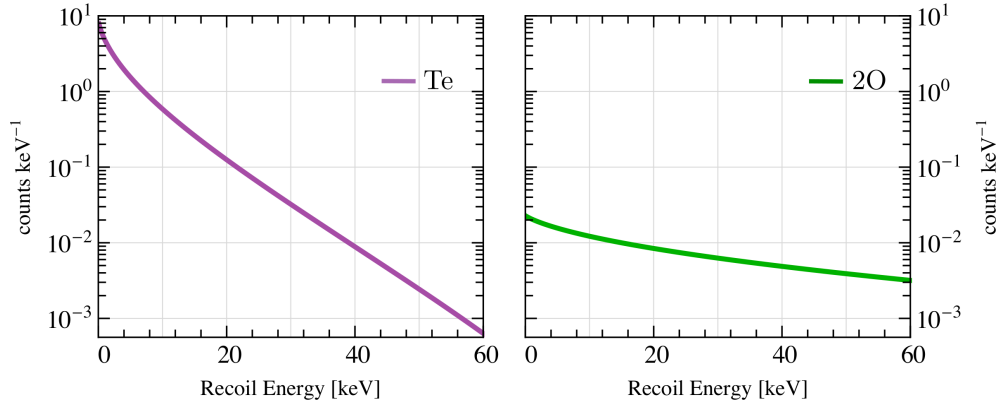
Figure 4.2: Energy spectra of nuclear recoils induced on tellurium and oxygen target nuclei by all the neutrino species summed up.

or an oxigen nuclear recoil because the thermal signal that is generated is identical in both cases. What is expected to be observed is therefore the sum of the spectra corresponding to different neutrino species and different target nuclei.
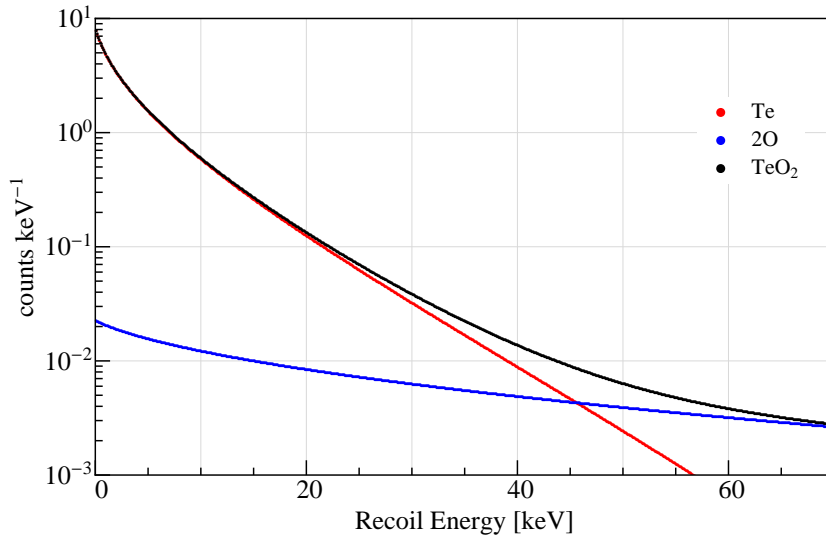
Figure 4.3: Total energy spectrum of recoiling nuclei scattered by all neutrino species emitted during a supernova explosion at 8.5kPc.

As the neutrino interactions are few but concentrated in a short time period (typically of the order of ten seconds), a significative value is the total number of interactions that are expected to be observed in the detector when the neutrino flux emitted by the supernova reaches it. This number is given by the integral of the spectrum of Fig. 4.3. All the spectra reported so far include events down to zero recoil energy. In a real detector this is, of course, a goal which is impossible to reach. The energy threshold of the detector is, however, a crucial parameter when the sensitivity has to be calculated. The signal, in fact, corresponds to the number of events whose energy is above the threshold, i.e. the spectrum of Fig. 4.3 has to be integrated with a lower bound equal to the energy threshold. The upper bound could, in principle, be infinite, but practically it is limited by the shape of the background the signal has to be compared with. Since the signal spectrum decreases monotonically, there will surely be an energy starting from which the integral of the background is much larger than the integral of the signal that vanishes increasing the energy. The integral of the total spectrum of Fig. 4.3 is reported in Fig. 4.4 as a function of the lower bound of the integral, i.e. the energy threshold of the detector [2].

4.2   Background comparison

To understand if the number of events, calculated in the previous section, that are expected to be observed in CUORE in case of a supernova explosion represents a signal that can be really and effectively recognized, it has to be compared with the background that can mimic it. In the context of this work the background is represented by any signal that is generated by the detector/electronic chain system, is triggered by the DAQ system and has an amplitude that corresponds to an energy in the region of interest (ROI); this ROI can be defined as the region of integration of the neutrino events yield described in the previous section. This wide definition of background collects a series of different sources, some of them being of some relevance only when events whose energy is very close to the threshold are searched for:

- particles that interact in the bolometer absorber, releasing a small amount of energy compared to the energy of typical events for which CUORE detector is mainly designed, i.e. the double beta decay events at few MeV. This background, that will be called *particle background* and abbreviated with B when necessary in the following, originates from a series of sources that are described in Section 3.3;

---

[2]The behaviour of the detector at its energy threshold has been considered ideal, i.e. the threshold function is an ideal step function. This is, of course, an approximation, but since the number of observed recoils is always small and no spectral shape analysis is performed, no corrections should be needed.
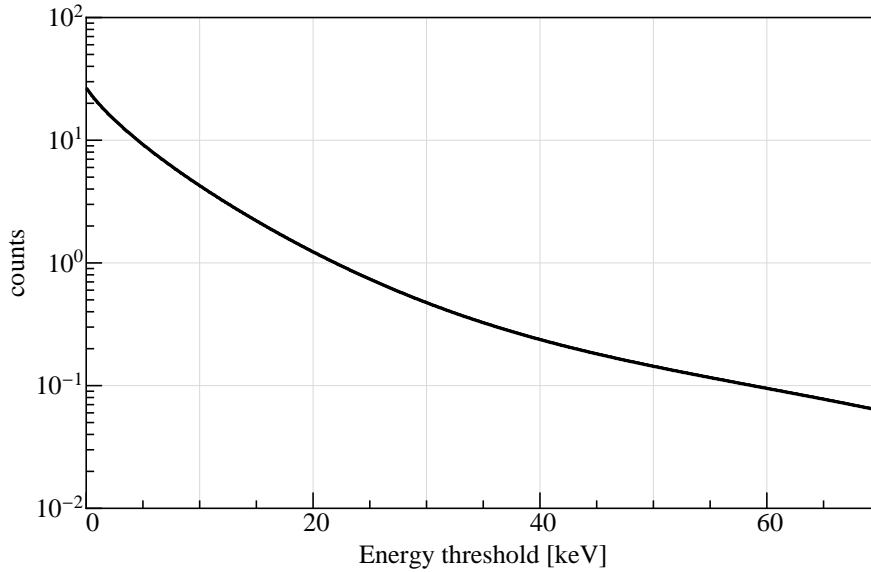
Figure 4.4: Integral of the total energy spectrum of recoiling nuclei scattered by all neutrino species, plotted as a function of the energy threshold of the detector, i.e. the lower bound of the integral.

this sources can directly emit low energy radiation or radiation with higher energy that is partially lost before reaching the active part of the detector;

- radiation that interacts in a part of the detector different from the absorber generating a pulse of small amplitude but whose shape differs from the expected one;

- thermal noise fluctuations, characteristic of any thermal detector, that can be generated by any kind of vibration or movement of the bolometers or the supporting structures;

- electronic noise, often spike-like, generated by the non-ideal behavior of the electronic chain components (ambient noise pick-up, cross talk between channels, mass loops).

With the only exception of the first item of the list above, all the other phenomena usually generate pulses with a shape different from the one expected from a particle interaction. This is, in principle, a powerful tool that can be used to reject those events and prevent them from contributing to the background. This is, in fact, the reason why the OptimumTrigger (see Section 1.4.3) is used for the data acquisition: it provides,

together with the selection of those pulses that (after the application of the optimum filter) are still above the threshold, a pulse shape parameter that can be used for a further suppression of those events whose shape is different from the expected one. Like every cut that selects or discards events based on the value of a parameter whose probability distribution has a shape different from an ideal Dirac-delta, the selection of the particle events performed by the OptimumTrigger has a non vanishing probability of including events that are not particle-induced. At the end of Section 1.4.3 this problem has been described in some detail. This is the reason why also the last three items of the list, that will be called *non-particle background* or N, contribute to the low energy background in CUORE. Some features of non-particle background, and in particular the fact that it can be non stationary, will impose some constraint on the development of trigger algorithm aimed at the detection of supernova neutrinos.

Since the contributions to the low energy background are so various, no analytical model or Montecarlo simulation has hitherto been developed that can describe it thoroughly. For this reason the background measured in CCVR2 [31] (Section 3.3) is used as a model for CUORE background. Since the experimental setup of CCVR2 and CUORE are relatively similar for what concern the elements of the detector that are expected to contribute to the low energy background, a simple scale factor based on the ratio between the two experiments active masses has been used to extrapolate the background to CUORE. This approach is considered conservative for two reasons: because many improvement in the material and environment purity has been forseen for CUORE detector, and because the low energy background in CUORICINO proved to be even lower than CCVR one (see, again, [31]). In Fig. 4.5 CCVR2 low energy background fit function is depicted. The background reported in Fig. 4.5 is a differential spectrum both in time and energy: it represents the number of pulses that would be recorded in 1kg of active detector mass every second, in 1keV wide bins. To actually compare this background with the expected signal a convenient extrapolation has to be made: the scale multiplicative factor is given by:

- the mass of CUORE detector in kilograms; it is $0.750kg/crystal \times 988crystals = 741kg$;

- a reduction factor, if present, that accounts for the improvements of CUORE background with respect to CCVR2 run; it is conservatively assumed to be equal to one;

- the integration time, i.e. the width of the time window where the pulses generated by supernova neutrinos are expected to fall.
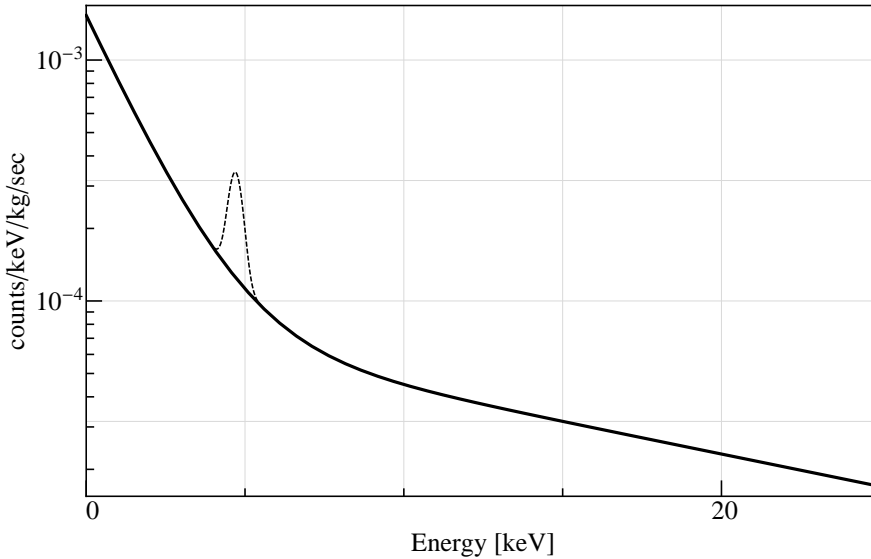
Figure 4.5: CCVR2 low energy data fit function. The function is used as model for low energy CUORE background, with the exception of the 4.7keV peak whose origin is still not clear. The bakground is expressed in number of counts detected every second in a 1keV energy bin by 1kg of active detector mass. It is the sum of the contributions that, in the text, have been defined B and N.

The last item is worth being analyzed a little deeper. The simplest assumption is that the integration time is 10 seconds, as it has been already assumed in the previous section, where the signal is defined as the integral of all the nuclear recoils induced by the neutrinos, the bulk of which is forseen by the theoretical models to be emitted precisely in a 10 seconds time lapse. During this interval, however, the probability of a neutrino interaction is not uniformly distributed, because the time profile of the emission is not flat. Instead, as described in Section 2.3.1, it has an exponential profile with a time constant of ~ 3.5 seconds.

The background events, on the contrary, are produced by phenomena that, on time scales of the orders of few seconds, can be considered to be well described by poisson statistics; thus background events have a uniform time distrbution in time.

As a consequence of this difference in the time behavior of the signal and the background, the statistical significance Σ of their comparison, that is being defined as the ratio between the first and the square root of the latter, depends on the integration time window t_{int}, either, as

$$\Sigma(t) \propto \frac{1 - \exp(-t_{\text{int}}/\tau)}{t_{\text{int}}} . \tag{4.19}$$

The function of Eq. 4.19 has a maximum in $t_{\text{int}} \simeq 1.2\tau \simeq 4s$. This means that, for a given total number of neutrinos interations, the window where the maximum significance is reached is different from the one that contains all the signal events.

4.3 Statistical significance

Now that the signal and background have been presented and discussed, a first, rough extimation of the statistical significance of the observation of a supernova can be done. The purpose of this estimation is providing a tool to evaluate if CUORE can really manage to detect a supernova explosion or, once the event is confirmed, carry out an analysis of it. The calculations that follow are made under the simpler and more conservative assumption: no optimized algorithm is applied to identify the supernova event, but a simple counting experiment is imagined. All the pulses with an amplitude greater than the energy threshold, but smaller than 25keV (the actual upper limit is in practice irrelevant once it is larger than about 10keV because the fraction of both signal and background pulses at higher energy is negligible compared to the total) in a 4 seconds window starting from the first event generated by a supernova neutrino interaction are counted.

In the previous sections the differential spectrum of signal events, integrated over the whole 10 seconds time window, has been called $Y(T)$; the particle background differential (both in energy and time) spectrum was $B(T)$ and the non-particle background $N(T)$; their sum is given by the CCVR2 spectrum and is assumed to be stationary over time periods of the order of few seconds. The total number of signal events that are considered is therefore

$$\text{signal[cts]} = \int_{T_{\text{threshold}}}^{T_{\text{max}}} \mathrm{d}T \, Y(T)[\text{cts/keV}] \times (1 - \exp(-4/3.5)) \tag{4.20}$$

while the total number of background events is

$$\text{background[cts]} = \int_{T_{\text{threshold}}}^{T_{\text{max}}} \mathrm{d}T \, (B(T) + N(T))[\text{cts/keV/kg/sec}] \times 741[\text{kg}] \times 4[\text{sec}] \,. \tag{4.21}$$

Since, as already explained, the upper limit of the integral is almost irrelevant in the calculations, both the signal and the background defined in Eq. 4.20 and Eq. 4.21 are function of the energy threshold $T_{\text{threshold}}$ alone. The statistical significance Σ is defined as the ratio between the signal and the statistical fluctuation of the background. Since we are working under the assumption of a counting experiment, the number of background events is described by the poisson statistics; for a background large enough

(of the order of 10 events) the average fluctuation of the background is therefore the square root of the background itself, hence

$$\Sigma(T_{\text{threshold}}) = \frac{\text{signal}}{\sqrt{\text{background}}} \tag{4.22}$$

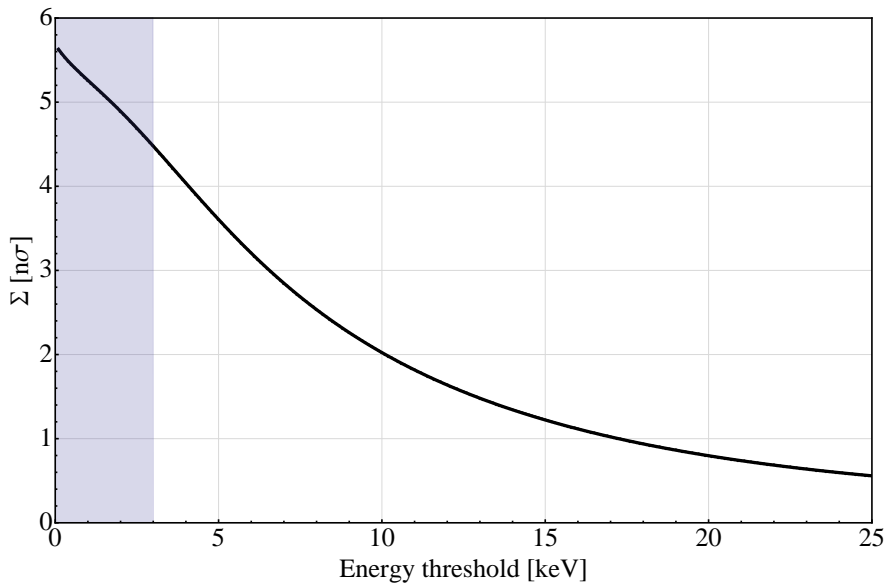is again a function of the energy threshold. In Fig. 4.6 this function is plotted.

Figure 4.6: Statistical significance of the observation of the signal described in this chapter, compared to the background observed in CCVR2 and renormalized to CUORE size.

In Fig. 4.7 the same data are shown in a different format: the background is depicted in red while the blue line is the sum of background and signal. The colored bands are one, two and three sigma fluctuations of the background, to be considered correct where the number of events is still large enough, indicative (but conservative) elsewhere because they have been calculated in the normal distribution approximation of the poisson statistics. Tab. 4.1 is useful to understand the order of magnitude of the number of events we are talking about; it summarizes the relevant quantities used in the calculation of the significance, and the statistical significance itself, for some reasonable values of the energy threshold.
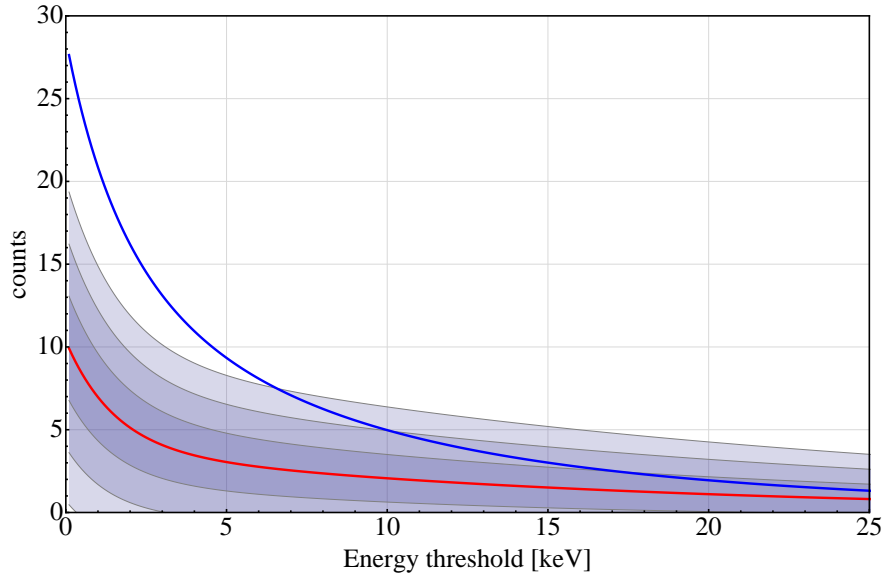
Figure 4.7: Direct comparison between signal (blue line is the total observed spectrum, i.e. signal plus background) and background (red line) with its statistical fluctuations (shadowed bands for 1, 2 and 3σ).

energy threshold [keV]	signal [cts]	background [cts]	$\Sigma[n\sigma]$
0	17.7	9.9	5.6
3	9.0	4.1	4.5
5	6.3	3.0	3.6
10	2.9	2.1	2.0
20	0.8	1.1	0.8

Table 4.1: Comparison between the number of signal and background events that are expected to be observed for different values of the energy threshold. For each threshold the corresponding statistical significance of the observation is reported.

The importance of the energy threshold is striking: the statistical significance of the observation drops quickly as the detector loses the capacity of triggering events at low energy bacause the energy spectrum of the nuclear recoils also drops rapidly with increasing energy.

To complete this chapter, it's worth analysing the statistical significance as a function of the supernova distance. Assuming an energy threshold of 3keV, the analysis performed until now is repeated varying the neutrino fluxes in order to simulate supernova explosions at different distances. The result is shown in Fig. 4.8 and it's easy to understand: the significance depends on the inverse squared distance because the signal is directly proportional to the total flux of neutrinos seen by the detector, whose dependence on the distance is expressed by Eq. 4.1. A significance of 3σ is achieved at a distance greater than 10kPc while a supernova at more than 12.5kPc should still be detected with 2σ significance.
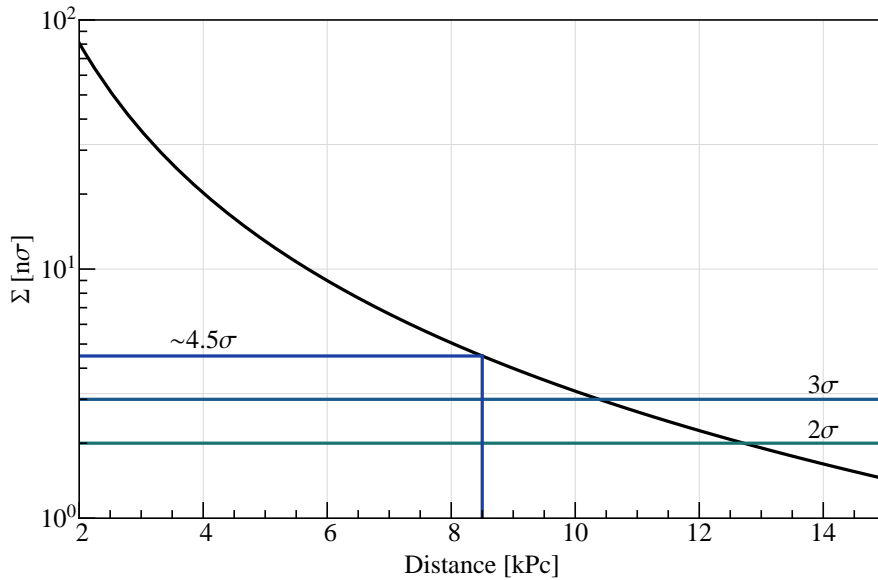

Figure 4.8: Significance as a function of the distance of the supernova once the detector threshold is fixed at 3keV.

Chapter 5

Dedicated supernova trigger and analysis

In the previous chapter the signal expected in the case of a 8.5kPc distant supernova explosion has been calculated and the statistical significance of an observation has been evaluated taking into account the background the signal has to be compared to, and its statistical fluctuation. This simple but naive method gives a useful idea of the potential of CUORE, but neglects some important factors that must be taken into account when addressing the problem of understanding the real potential of the experiment for the detection of the neutrino signal:

- an algorithm for the detection of the signal from a supernova can be developed and optimized; this algorithm can be, in general, more complicated and efficient than a simple event counting procedure and can extract more information from the data;

- not only the number of background events in a time window fluctuates, but also the number of detected signal events is affected by a statistical fluctuation that is described by the poisson statistics; the simple method used in the previous chapter does not consider this fluctuation but assumes a fixed number of signal events;

- if the algorithm that identifies the supernova signal is meant to be applied online on the continuous data flow, a maximum rate of false positive must be considered as a limiting parameter to the sensitivity of the algorithm itself.

In this chapter two different approaches to the development of a trigger algorithm are presented, and the advantages of the two are stressed out. The first algorithm is a

development of the simple counting technique in which the problem of the rate of false positives is taken into account, while the second one is a more sophisticated maximum likelihood fit-based algorithm whose discovery potential has been studied by means of a toy Montecarlo simulation.

5.1   Fixed false positive rate poisson-based trigger

A trivial supernova trigger is an algorithm that continuously monitors the rate of physical (particle generated) events in the whole detector comparing it with a fixed threshold. The rate is evaluated counting how many events are recorded within a time window before each event. The length of the window should be chosen in such a way that the signal to noise ratio is minimized. Since the noise is simply the statistical fluctuation of the number of events generated by all the other phenomena but the supernova (the sum of what we have called B and N at the beginning of Section 4.2), the optimum window has already been defined by maximizing Eq. 4.19; the optimal integration window will be called w hereafter.

If the background rate is constant throughout a measure, the threshold can be defined in terms of the number of standard deviations of the background counts in the integration window w. If this number is large enough, the square root of the number of events can be considered as a good estimator of the standard deviation and, given a number of standard deviations as threshold, the probability that a background fluctuation exceeds this threshold is easily calculated. If the number of $B + N$ events is small, the Poisson statistics has to be used. The probability that, given an average number of counts in the integration window $B + N$, x events are recorded in the same window is

$$P(x, B + N) = \frac{(B + N)^x e^{-(B+N)}}{x!} \ .$$ (5.1)

The probability that a fluctuation of the background $B + N$ induces a number of counts x that exceeds a given threshold x_{th} equals the integral of the Poisson distribution of Eq. 5.1, calculated from the threshold up to infinite:

$$P(x \geq x_{\text{th}}, B + N) = \sum_{x=x_{\text{th}}}^{\infty} P(x, B + N) = 1 - \sum_{x=0}^{x_{\text{th}}} P(x, B + N) \ .$$ (5.2)

This number represents the probability that, if one of the recorded events is randomly chosen, the number of events in a window w preceding that very event exceeds the threshold simply because of a random fluctuation. Therfore, the product of this probability times the average rate of background events $(B + N)/w$ gives the frequency at

which a false positive happens, i.e. the frequency at which a fluctuation of the background is confused with a signal because it passes the threshold. This frequency, or false positive rate, R_{FP}, is therefore expressed as:

$$R_{\mathrm{FP}}\left(x_{\mathrm{th}}, \frac{B+N}{w}\right) = P(x \geq x_{\mathrm{th}}, B+N) \times \frac{B+N}{w} , \tag{5.3}$$

that, using Eq. 5.2, reads:

$$R_{\mathrm{FP}}\left(x_{\mathrm{th}}, \frac{B+N}{w}\right) = \left(1 - \sum_{x=0}^{x_{\mathrm{th}}} P(x, B+N)\right) \times \frac{B+N}{w} . \tag{5.4}$$

The false positive rate is a function of two parameters: the threshold on the number of counts in the time window w that must be exceeded to make the trigger fire, and the average rate of background counts. If the latter is (as we have assumed until now in the discussion) constant, the former can be also assigned a constant value in order to fulfill the condition

$$R_{\mathrm{FP}}\left(x_{\mathrm{th}}, \frac{B+N}{w}\right) = R_{\mathrm{allowed}} , \tag{5.5}$$

where R_{allowed} is a reasonable maximum number of false positives that can be accepted.

5.1.1 Algorithm development

A more realistic description of the background can be introduced in the algorithm. There's no reason that prevents the particle-induced background B from beeing considered constant over very long time scales, but the same is usually not true for the component N that is associated to the non ideal behavior of the detector. A period of time with a particularly high level of noise, for example, can generate an increase in the value of N. Since bolometers (and a large array of bolometers in particular), especially at low energy, are very sensitive and complicated detectors, some non-statistical low frequency variations of the noise level can be expected, and consequent fluctuations of the number of non-rejected noise events N as well.

Under these conditions, a running background rate, $R_{B+N}(t)$, must be used instead of the fixed one, $(B+N)/w$. The running background rate is calculated as the ratio between the number of events detected in a window of length W and the length of the window itself. The choice of the legth W is crucial. It must be long enough to average over the statistical fluctuations of the number of background events, in such a way that, if the true value of the background rate is constant, the fluctuations in $R_{B+N}(t)$ would also be negligible. Even more important, the length W must be so large that the number of events generated by a supernova, whenever it occurs, is much smaller than

the number of background events in the large window; since w is optimized exactly in the opposite sense, this is usually realized as long as $W \gg w$. At the same time, the length of the window must be comparable with the time scale of the variation of N to reflect them. Assuming the background rate from CCVR2, whose value is $\sim 1\text{Hz}$, as a reference, a 1 minute window should contain, on average, 60 events. The corresponding statistical fluctuation is about 10%. It corresponds to a fluctuation of much less than 1 event on the number of events that fall in the four seconds optimal window, four, and is therefore negligible. If the CUORE background proves to be lower, the integration window used to evaluate of the running average background rate should probably be enlarged to include a larger number of events.

By replacing, in Eq. 5.4, the fixed background rate, $(B + N)/w$, with the running one, $R_{B+N}(t)$, the false positive rate also becomes a function of the time because it depends on the background level in the previous W seconds:

$$R_{\text{FP}}(x_{\text{th}}, R_{B+N}; t) = \left(1 - \sum_{x=0}^{x_{\text{th}}} P(x, R_{B+N}(t)w)\right) \times R_{B+N}(t) \,. \tag{5.6}$$

By replacing the explicit Poisson distribution of Eq. 5.1, Eq. 5.6 becomes

$$R_{\text{FP}}(x_{\text{th}}, R_{B+N}; t) = \left(1 - \sum_{x=0}^{x_{\text{th}}} \frac{(R_{B+N}w)^x e^{-(R_{B+N}w)}}{x!}\right) \times R_{B+N}(t) \,. \tag{5.7}$$

Again, x_{th} is implicitly defined by Eq. 5.5; this time, however, x_{th} is also a function of time. In this way an adaptive threshold has been defined: in a moment where the background rate increases, the threshold will also increase in order to keep constant the probability that a fluctuation of the (increased) background is triggered. Vice versa, if the background rate drops, the threshold can be lowered without increasing the rate of false positives.

In practice, the trigger condition is simply that the number of events x in the window w must be larger than the threshold $x_{th}(t)$; since the latter is defined implicitly, also the trigger condition is implicit and can be written as

$$R_{\text{FP}}(x_{\text{th}}, R_{B+N}; t) \leq R_{\text{allowed}} \tag{5.8}$$

that becomes, using Eq. 5.7, dividing by R_{allowed} and inverting:

$$TV_1 = \left[\left(1 - \sum_{x=0}^{x_{\text{th}}} \frac{(R_{B+N}w)^x e^{-(R_{B+N}w)}}{x!}\right) \times \frac{R_{B+N}(t)}{R_{\text{allowed}}}\right]^{-1} \geq 1 \,. \tag{5.9}$$

This expression is the one that is directly implemented in the algorithm that is applied to the data; let's summarize the steps of the algorithm:

1. events in the whole detector are triggered with the OptimumTrigger algorithm described in Section 1.4.3; the pulse shape parameter is used to reject with the highest theoretical efficiency non-physical pulses; only events with an energy between the threshold and about 25keV are considered;

2. for each event selected in the previous step, occurring at time t, all the events (also selected in the previous step) that fall in a time window $[t - w; t]$ before the considered event are counted. The obtained number is x;

3. for each event the number of events in the larger window $[t - W, t]$ is also computed; this number, divided by W, gives the average rate of background events $R_{B+N}(t)$ at the time of the considered event; this rate times the window w gives the expected number of background events at the time t of the considered event;

4. the quantity on the left side of Eq. 5.9 is computed; it represents the trigger value at time t and it is compared with 1.

5.1.2 Discovery potential of fixed false positive rate poisson-based trigger

We study, in this section, the discovery potential of the described algorithm. The most efficient way to estimate the performance of a trigger algorithm is usually considered to be the application of the algorithm in its full complexity to Montecarlo generated events. The simulation should include a background built on the model of the expected real background, and a signal, that the algorithm is supposed to identify, of known magnitude. The possibility of varying the strength of the signal with respect to the background allows to evaluate the minimum signal that can be discriminated from the background with a given probability and background rate and, at the same time, provides an estimation of the behavior of the algorithm when no signal is present, thus fixing the confidence level with which a discovery can be stated. Moreover, a toy Montecarlo, compared with the analytical method used in Section 4.3, provides more accurate values for the statistical parameters that describe the performance because both background and signal statistical fluctuations can be simulated and their combined effect taken into account.

In practice the study has been performed in the following way: a large number of time windows of a given length are created, and, in each window, the relative arrival times of background and signal events are generated.

5.1 Fixed false positive rate poisson-based trigger

Background events are generated by extracting their arrival times from a flat (constant in time) distribution, in such a way that the time differences between adjacent events are exponentially distributed, where the time constant of the exponential is the inverse of the background rate. In this way, background events are distributed in time following a poisson distribution, as the low energy background is expected (and has been observed) to be. The number of generated events for each simulated window is extracted from a poisson distribution with the average being the background rate times the window length; in this way the statistical fluctuations of the background are also included. Signal events are generated by extracting their arrival time from a normalized distribution shaped like the supernova neutrinos time distribution, i.e., in this work, an exponential with decay time 3.5s. As with background, the number of signal events that has been generated in each window is extracted from a poisson distribution whose average is the number of expected neutrino interactions from a supernova at the distance that is beeing simulated. By changing this average value supernovae at different distances are simulated. The exponential distribution from which the signal events arrival times are extracted doesn't necessarily starts at the beginning of the window. Therefore, the behavior of the trigger when applied to a window that contains the supernova signal but in which the signal is not exactly at the beginning of the window has also to be studied. For this reason, different simulations have been completed with different delays between the beginning of the analyzed window and the beginning of the signal. In Fig. 5.1 some features of the Montecarlo are illustrated. The line represents the function (which is normalized, in this case, to 22 signal events) which is the distribution from which the events arrival times are extracted. It is defined on a window whose length is calculated in such a way that, after the signal starting point (second 7 in this example), a lapse of five times the decay time is contained (17.5 seconds). In this way the number of signal events that are expected to happen within the detector (22, in this case) for the supernova that is being simulated are always generated, but only the fraction of them that falls within the first 14 seconds (red line) is analyzed. The 14 seconds window is the length of the fit window used in the second algorithm, described in the next section. The algorithm which is described here, instead, considers only the events that fall in the window w in sync with the exponential (light green window). The signal, of course, is partially contained also in the light red windows depicted in Fig. 5.1. In the study of this algorithm, only the green window, starting from the first signal event, is considered. In the real case, the trigger is likely to fire also in some of the (light red) windows that contain part of the signal. However, due to the exponential decay of the probability of finding an event when the distance from the starting point is increased, the probability that this windows contain more signal events than the first (green) one is negligible.
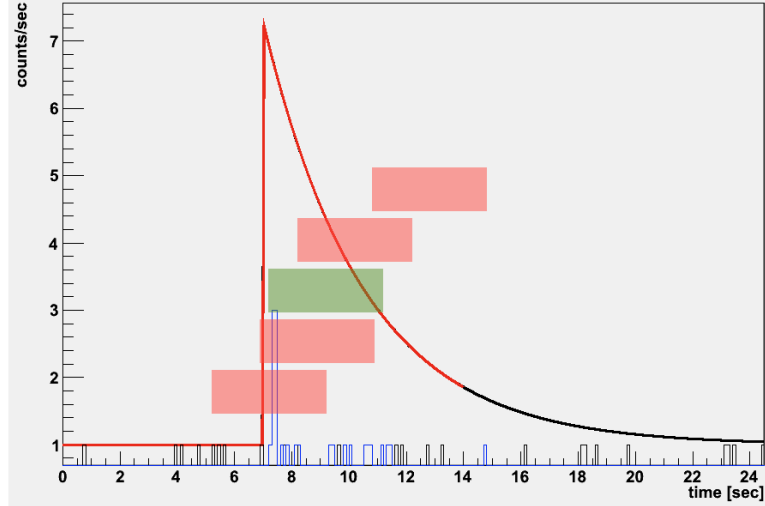
Figure 5.1: Example of distribution from which the event times are extracted to generate the simulated window on which the trigger algorithm is applied. The supernova signal starts 7 seconds after the beginning of the window. The red part represents the window that will be used in the second algorithm described: only a fraction of the events due to the supernova are analyzed; this describes what effectively happens in the real online case, where the algorithm is applied to every window, without knowing if a signal is present and where it starts. The coloured bands represent some of the time windows that are considered by the first algorithm, one for each triggered event in the detector. The green one is the window starting in sync with the supernova signal, and thus the one where the TV_1 is expected to be higher.

Many sets of simulated windows w are generated varying the known number of signal events; each set corresponds to a distance d of the supernova. For each window in each set the quantity TV_1 of Eq. 5.9 is computed, and the distributions of this quantity are plotted in Fig. 5.2 for some values of the distance.

The x axis is in logarithmic scale thus the threshold on TV_1 corresponds to 0 on this axis. The integral of the distributions above zero is the probability of triggering a supernova at the corresponding distance, with a rate of false positives $R_{\text{allowed}} = 1/\text{week}$. Some features of the distributions have to be discussed. TV_1 is not a continuous variable but can assume only a discrete set of values because the integral of the poisson distribution can assume only discrete values[1]. This is the reason why the distributions are discrete valued. Morover, the shape of the distributions tends to be deformed and to

---

[1]The poisson distribution is defined only for integer values unless a continuous extension is used; in this algorithm the discrete version has been used
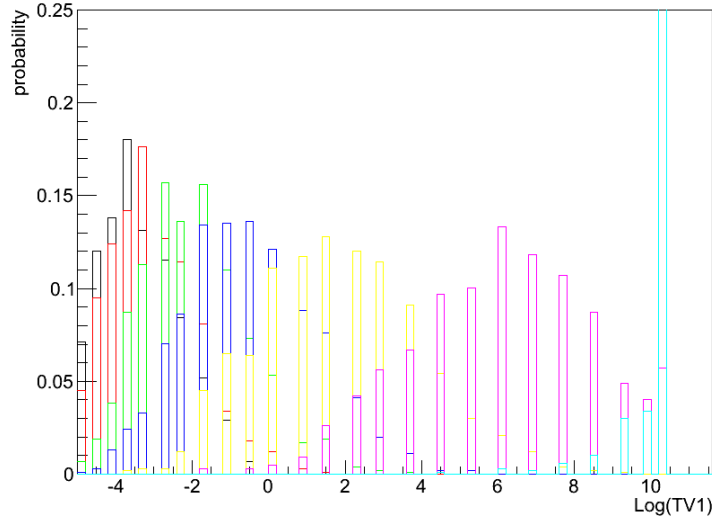
Figure 5.2: Distributions of the trigger value TV_1 calculated on Montecarlo data for different values of the distance d of the supernova. Light blue = 4.5kPc, violet = 5kPc, yellow = 6.5kPc, blue = 7.4kPc, green = 8.5kPc, red = 9.7kPc, black = 10.2kPc. The threshold for the trigger is 0 (x axis is log-scale); the fraction of the distribution above threshold corresponds to the probability of detecting the event, given the fixed rate of false positives.

saturate at some value of TV_1 for increasing magnitude of the signal (decreasing distance of the supernova). This is due to the fact that, when the number of events in the window is much larger than the number of expected background events, the difference in Eq. 5.9 becomes so close to zero that precision problems occur in the calculations. Since this phenomenon is observed only when the number of events is so far from the threshold that the probability of missing the detection is negligible, it is considered to be harmless.

Starting from the distributions in Fig. 5.2, the fraction of the distribution above threshold for each value of the supernova distance is computed. By interpolating these numbers the curve that describes the probability of detection at each distance can be built, and it is reported in Fig. 5.3.

From Fig. 5.3 some numbers can be extracted:

- the probability of detecting a supernova at a distance of 7.2 kPc, with an average rate of false positives of 1/week, is about 50%;

- the probability of detecting a supernova at a distance of 6 kPc or less, with an average rate of false positives of 1/week, is about 100%;

- the probability of detecting a supernova at a distance of 8.5 kPc, with an average rate of false positives of 1/week, is about 10%.
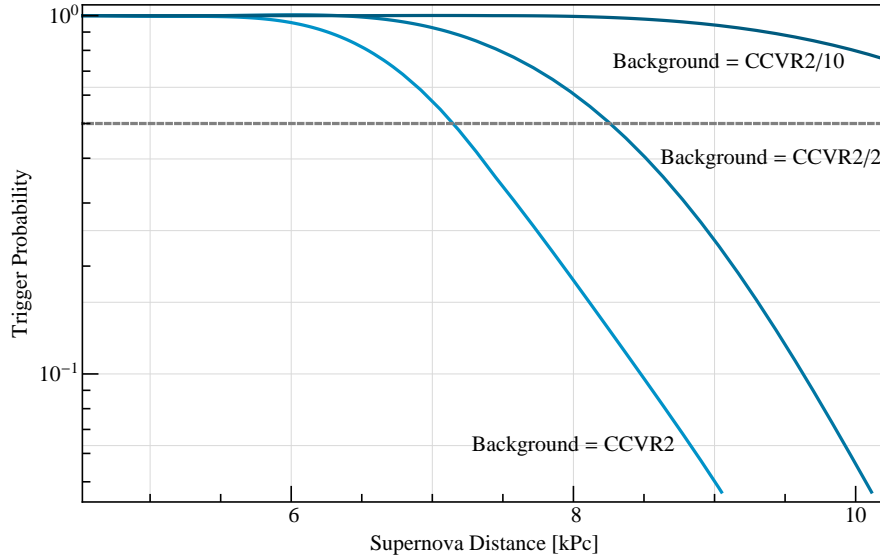
Figure 5.3: Detection probability associated to the poisson-based algorithm as a function of the supernova distance. The three different lines correspond to three different values of the average backgound rate. The dashed line shows the 50% probability of detecting the supernova; the corresponding distance depends strongly on the background level.

In Fig. 5.3 two more curves are reported; they correspond to the probability of detection if the background is reduced by a factor 2 to 10 with respect to CCVR2 background. The reason of this comparison is that the use of CCVR2 background extrapolated to CUORE mass is in general a conservative choice. Since CUORE is beeing built with state-of-the-art procedures for material selection and assembly, a reduction of the background is expected, but it is not easy to quantify. A reduction of the background has a huge effect on the sensitivity of this algorithm; in Eq. 5.9 the term $R_{B+N}(t)$ appears twice, and in both cases it's reduction goes in the direction of increasing the sensitivity. If the mean of the poisson distribution $(R_{B+N}(t)w)$ is reduced, the same value of the sum, that goes from 0 to x_{th}, is obtained for smaller x_{th}. Moreover, since also the factor $\frac{R_{B+N}(t)}{R_{\text{allow}}}$ - that multiplies the sum - is reduced, x_{th} can be further reduced (thus increasing the probability of having a fluctuation above threshold) without increasing the rate of false positives. This combined effect pushes the distance at which a supernova is detected with 50% probability to about 8.5kPc for a factor two reduction of the background, and far beyond 10kPc in case CUORE will succeed in reducing the background by an order of magnitude compared to present detectors.

123

5.2   Likelihood fit-based trigger

The second algorithm that has been developed for the online analysis and trigger of supernova events is descibed in the following. It is applied on the same data used by the previous algorithm. Among the pulses recorded in all the crystal of the CUORE detector, only the ones generated by a particle interaction are selected by means of the shape parameter provided by the OptimumTrigger algorithm. The energy is also taken into account and only events with energy between the threshold and a maximum energy (tipically 25keV, but the chosen value is only marginally relevant because the number of both background and signal events decreases rapidly with energy) are analyzed. For each one of these selected events, the arrival times of all the previous events within a time window of a given length are considered and a set of relative times is created. The lenght of the window can in principle be chosen of any value, but, since the signal has an exponential time profile, a window whose length is 4 times the decay time (14 seconds) can be assumed to contain all the signal when the supernova burst starts at the beginning of the window.

Once the events are selected, a model of the time distribution of supernova plus background events is fitted to the set of arrival times with a maximum likelihood method.

5.2.1   Model building

The model for the distribution of the arrival times within the window is the sum of a model for the background and one for the supernova neutrinos burst.

The background has, as already described, a flat probability distribution because it is generated by processes that follow the poisson statistics. The only parameter that describes a poissonian distribution is the expected value for the number of events in the window, which is equal to the expected rate of events times the length of the window itself. This parameter is fixed, in the fit, to a value calculated starting from the average background rate that has been measured in a window of adequate length before the fit window. This calculation is the same that is performed in the estimation of the average background in the poisson-based counting algorithm of the previous section, and the same considerations on the length of the interval used to evaluate the average background are valid, Section 5.1.1.

The model that describes the time distribution of the interactions of the neutrinos coming from the supernova burst is the already described exponential with 3.5 seconds decay time. In this case both the normalization of the exponential (i.e. the total number of events that are considered to be associated to the supernova) and the starting point of the exponential profile (i.e. the starting point of the burst) within the time window

are free parameters of the fit.

The model can than be formalized as

$$\mathcal{M}(t; S, t_0) = R_{B+N} + \theta(t - t_0)\frac{S}{\tau}e^{\frac{-(t-t_0)}{\tau}} \qquad (5.10)$$

where S is the signal normalization and t_0 the starting point of the exponential, and they are the free parameters of the fit. $\theta(t - t_0)$ is the Heaviside step function that accounts for the absence of signal events before t_0.

5.2.2 Algorithm implementation and test

The implementation of the algorithm inside the module of the CUORE software responsible for online supernova trigger is done by means of the ROOFIT software suit, from CERN software repository. It provides the instruments to build a model and fit it to unbinned data by minimizing the corresponding likelihood. It was chosen, instead of writing a dedicated code for the calculation and minimization of the unbinned likelihood, because of its versatility, speed and wide diffusion. By exploiting MINUIT tools, it provides robust and reliable results in the minimization procedure.

Since the number of events in the window is in general rather small, the fit result turns out to strongly depend on the choice of the starting point of the t_0 parameter; the minimization often converges to a local minimum close to the starting point, instead of converging to the real best fit whose t_0 can fall with uniform probability in any point of the fit range. A simple but effetive trick was implemented to overcome this problem. For each set of events (a time window), the fit is performed 8 times, each time with a starting value of t_0 incremented by 2 seconds, starting from $t_0 = 0$. For each fit the minimum of the likelihood function is returned and the value of the parameters corresponding to the smallest likelihood is considered as the best fit of the model to the data. In this way the strong dependence on the initial value of the parameter is smoothed out and the behavior of the algorithm is almost always predictable, with some biases that will be discussed in the following.

In order to test the performance of the algorithm, the toy Montecarlo generated events have been used once again. First, the best fit parameters have been compared with the corresponding true values that were known a priori because they are the input for the generation of simulated events. A large number (5000) of time windows containing signal events have been used, with both the magnitude of the signal (i.e. the number of events extracted from the exponential distribution) and the starting point randomly chosen. These windows have been analyzed with the maximum likelihood fit algorithm and, for each window, the best fit parameters ($\hat{S}$ and $\hat{t}_0$) have been compared

with the true values by calculating the quantities

$$A = \frac{\hat{S} - S}{\sigma(S)} \qquad\qquad B = \frac{\hat{t}_0 - t_0}{\sigma(t_0)} \qquad\qquad (5.11)$$

where S and t_0 are the true values of the corresponding parameter (that are known because they are the ones used to generate the Montecarlo events) while $\sigma(S)$ and $\sigma(t_0)$ are the errors on the single parameter evaluation returned by the fit procedure (for a discussion on the statistical meaning of these errors see [66]).
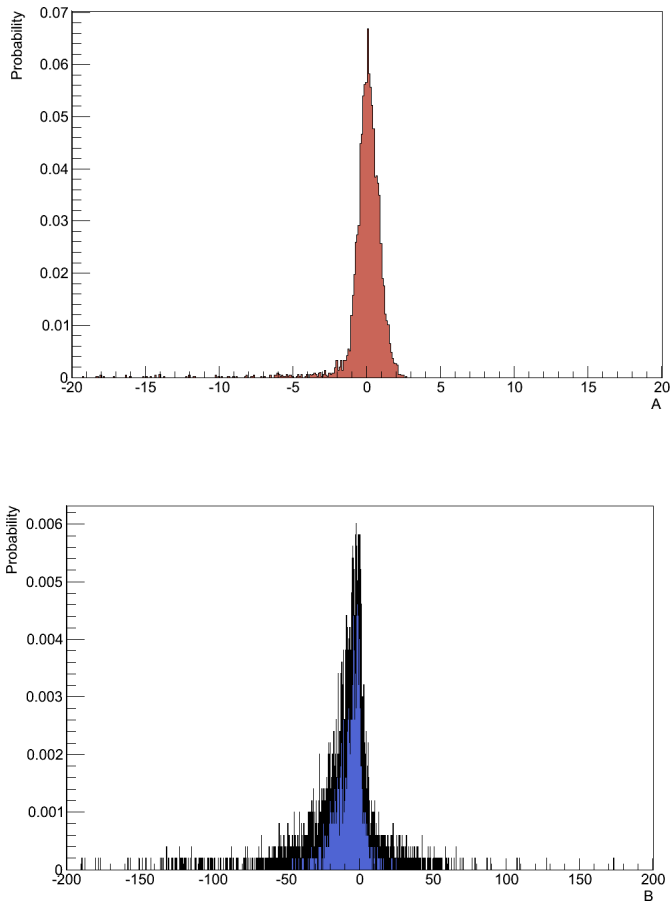

Figure 5.4: Distributions of the variables A and B that show the bias of the corresponding parameter estimators S and t_0. The first shows a good behaviour, with a gaussian shape centered in zero and sigma ~ 1.5. The estimator of the arrival time is much less robust and shows a moderate bias towards small values of the parameter and a tendency to underestimate the error.

The distributions of the variables A and B are depicted in Fig. 5.4, as calculated on 5000 montecarlo generated supernova events with starting time uniformly distributed within the 14 seconds time window, and the signal magnitude also uniformly distributed between 0 (corresponding to a supernova located far beyond the CUORE detection capabilities) and 31 supernova neutrino interactions (for a supernova at 5.5kPc).
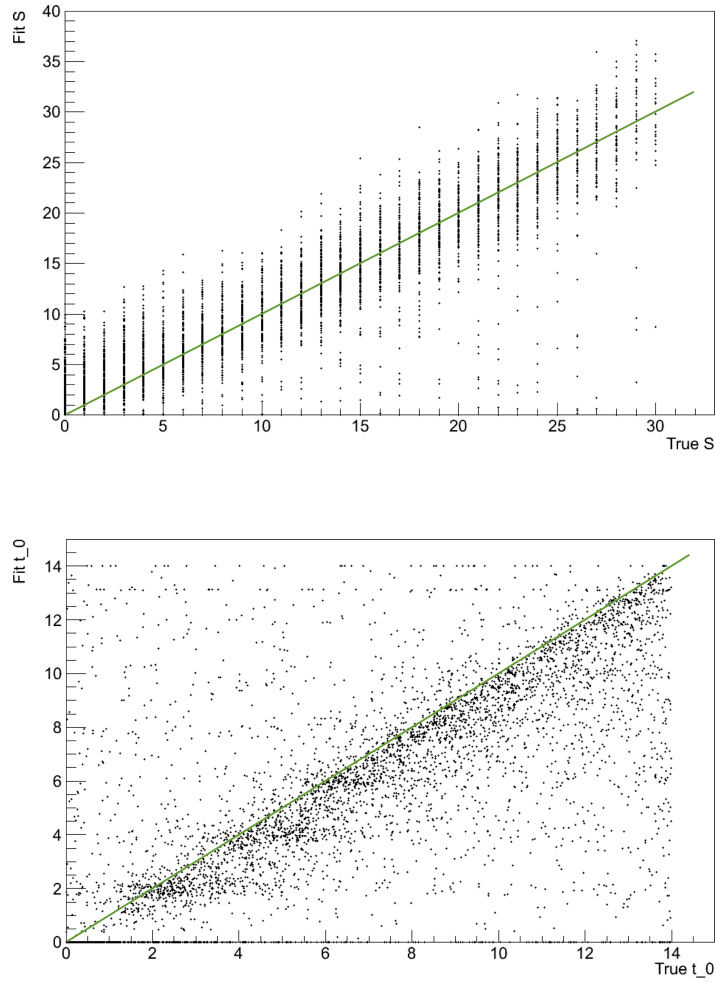

Figure 5.5: Correlation between the true value and the reconstructed value of the two free parameters of the fit, S and t_0. The green line represent the right reconstruction.

From the same simulated data the plots of Fig. 5.5 are extracted, representing the correlation between the real value of the S and t_0 variables and the reconstructed value returned by the fit. Again, the reconstruction of the signal magnitude is precise, with a saturating behavior at low values of the signal (i.e., the algorithm shows a tendency to find small values of the signal also for vanishing simulated signal in the data). The starting time can generally also be extracted but with a minor precision and a bias towards small values across all the range of t_0.
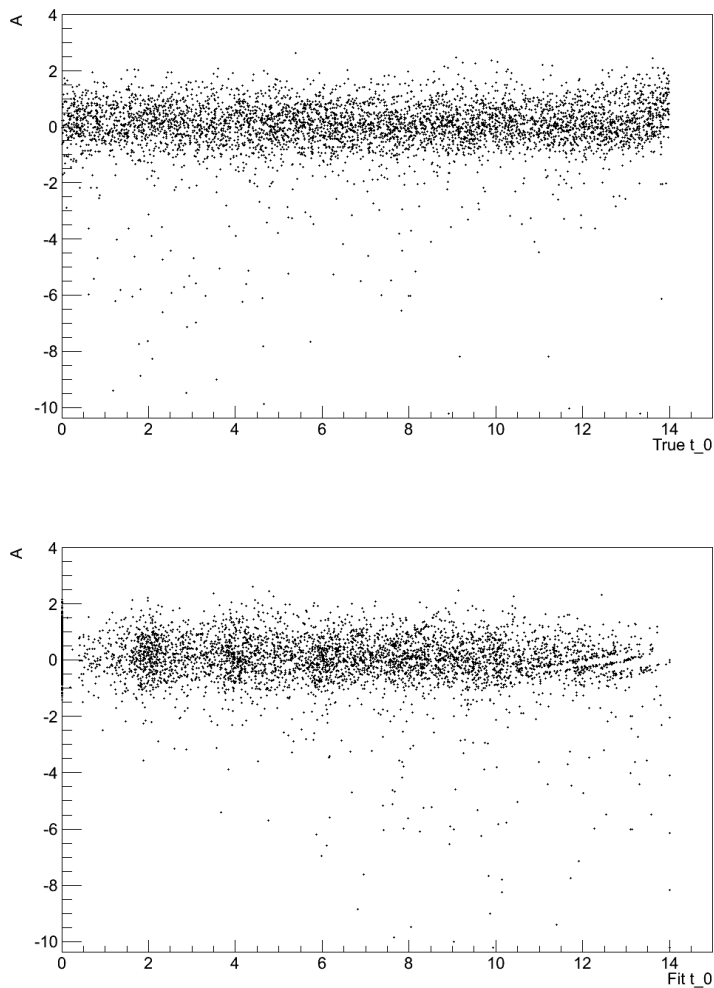

Figure 5.6: Dependence of the A variable, i.e. the bias indicator of the estimator of S, from the true value of the signal starting time t_0 (top) and reconstructed started time (bottom) from the simulated data. There is no evident dependence.

In order to better understand the behavior of the algorithm, the correlation between the reconstructed value of a parameter and the true value of the other has also been checked. In Fig. 5.6 the correlation between A variable and the true value of the signal starting point t_0 is plotted.

Fig. 5.7 is the equivalent of Fig. 5.6 but shows the dependence of the bias of the estimator of t_0 from the true value of the signal magnitude S. Also in this case, no evident dependence is present, showing that the values returned by the fit for the two free parameters are, within the corresponding errors, independent.
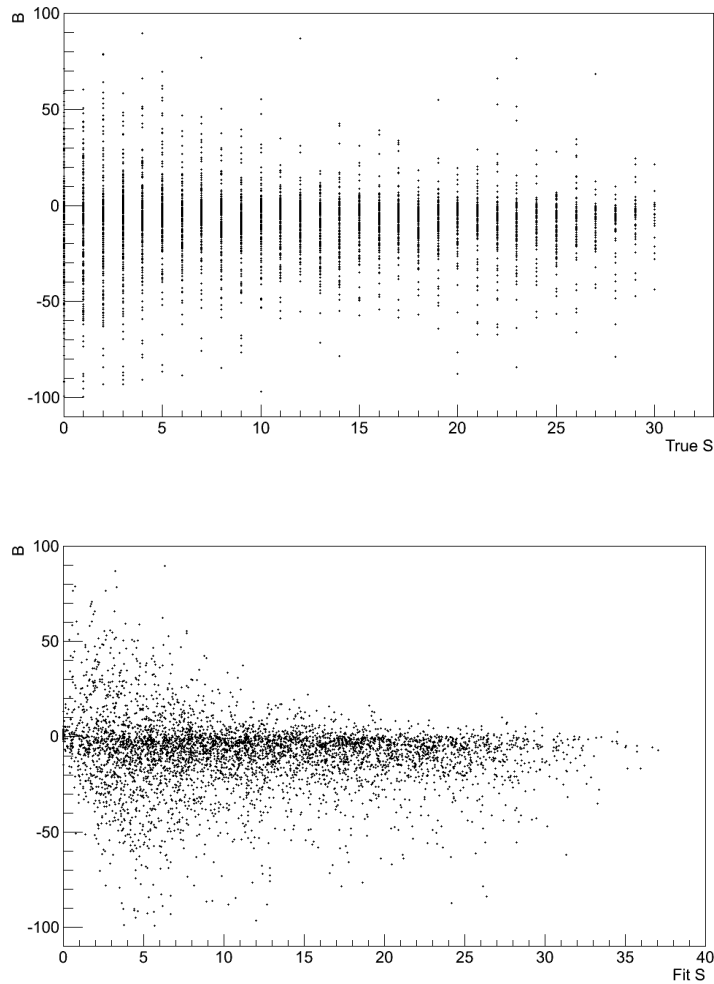

Figure 5.7: Dependence of the B variable, i.e. the bias indicator of the estimator of t_0, from the true value of the signal magnitude S (top) and reconstructed amplitude (bottom) from the simulated data. There is no evident dependence.

5.2.3   Discovery potential of likelihood fit-based trigger

With the same procedure described in Section 5.1.2, the simulated data have been used to calculate the discovery potential of the fit-based algorithm. Since this algorithm is also aimed for an online application, particular attention should be put on the estimation of the probability (or rate) of false positive occurrence. For each event recorded in the whole detector the algorithm returns the expectation value of two quantities that are calculated on the data contained in a window preceding the event itself. Of these quantities only the expectation value of the signal magnitude is used in the online analysis as trigger value ($TV_2 = \hat{S}$); it is simply compared to a threshold and the trigger fires if its value is larger than the threshold. In this case, the time of the beginning of the supernova signal is the value of the parameter $\hat{t}_0$ also returned by the fit. The choice of the threshold is driven by the need to limit the rate of false positive events to a controlled value. In order to select the threshold value, the toy Montecarlo is used and simulated time windows with no signal are analyzed with the algorithm. The values of the signal amplitude $\hat{S}$ returned by the algorithm when the data contain only background are reported in the histogram of Fig. 5.8 for 100000 simulated windows.
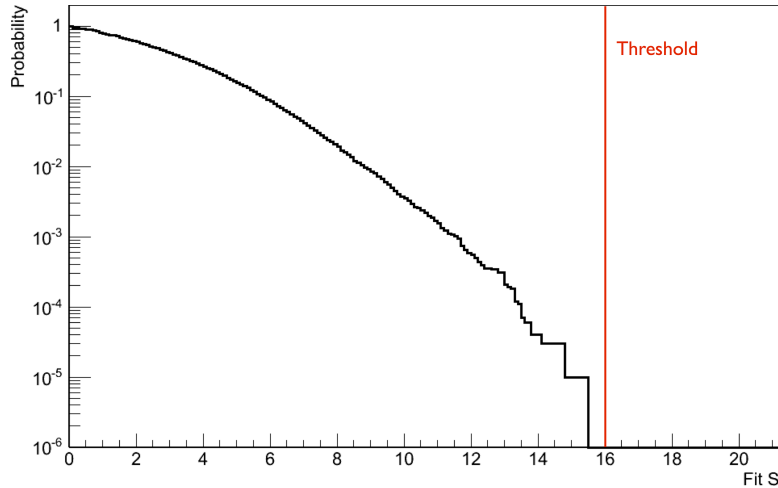

Figure 5.8: Integral of the probability distribution for the estimator $\hat{S}$ of the signal amplitude when no signal is present in the simulated windows. The red line represent the threshold that must be put on the value of $\hat{S}$ in order to have a rate of false positive smaller than one per week when the background rate is 1Hz, the one measured in CCVR2 and scaled for CUORE mass.

The histogram represents the integral probability for the fit parameter $\hat{S}$, i.e. for each value of the parameter $\hat{S}$, the probability of obtaining a larger value of the parameter itself is represented by the height of the histogram. In this way a direct evaluation of the probability of triggering a false event can be obtained. For a rate of events in the whole detector R_{B+N}, a rate of false positive R_{FP} is obtained as

$$R_{\text{FP}} = R_{B+N} \times P_{\text{FP}} = R_{B+N} \times P(\hat{S} > S_{\text{threshold}}) \tag{5.12}$$

that implicitly defines $S_{\text{threshold}}$ as the value of $\hat{S}$ where the integral probability of Fig. 5.8 is equal to R_{FP}/R_{B+N}. By fixing the maximum allowed rate of false positives to $R_{\text{allowed}} = 1/\text{week} \simeq 1.6 \times 10^{-6}\text{Hz}$ and the rate of events to $R_{B+N} = 1\text{Hz}$, the (conservative) value for the threshold is 16 events. In order to obtain a maximum rate of false positives of 1/week, the trigger must fire only when the number of signal events (normalization of the exponential component of the fitted model) returned by the fit exceeds 16 events. This threshold, reported in the plot of Fig. 5.9, allows to evaluate the discovery potential of the algorithm corresponding to this constraint.
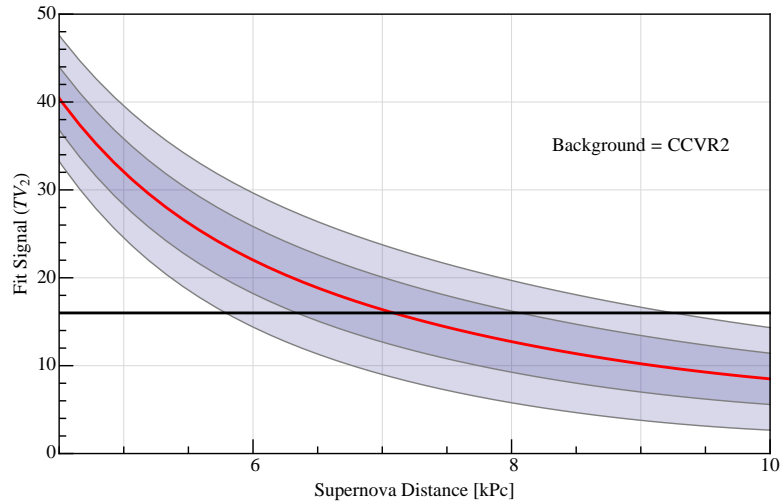

Figure 5.9: The plot represents the extrapolation at all distances of the distributions of the reconstructed signal. The red line represent the average of the distributions, determining the 50% probability of detection. The orizontal black line is the threshold that has to be put with CCVR2 background in order to keep the rate of false positives below 1/week. For each distance, the fraction of the shadowed bands above the threshold represents the probability of detecting a supernova at the corresponding distance.

The plot in Fig. 5.9 has been obtained in the following way: Montecarlo simulated windows with both background and signal have been analyzed; for each value of the simulated signal (corresponding to a given distance of the supernova) the distribution of the reconstructed signal amplitudes (see Fig. 5.10) has been fitted with a gaussian shape, that turns out to be a good approximation of the actual shape of the distribution. The mean value of the fitted gaussian is used as the expected value for the estimator $\hat{S}$ of the signal amplitude corresponding to the considered distance, and the σ is used to draw the confidence bands. Since the expectation values have been computed only for a discrete set of distances, an interpolation has been performed to obtain the continuous curves of Fig. 5.9.
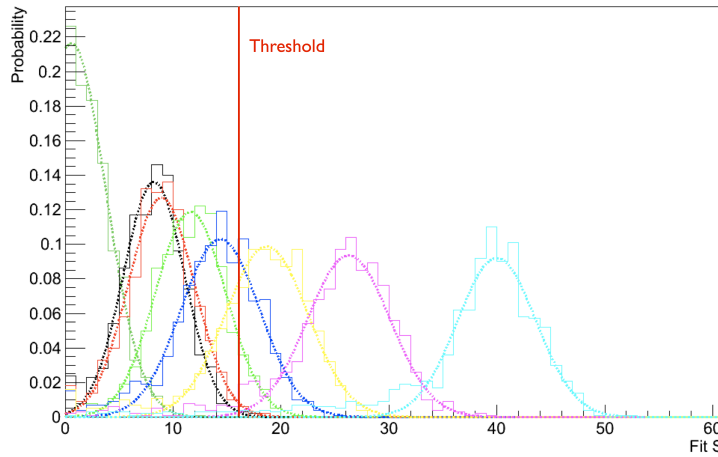

Figure 5.10: Distributions of the reconstructed signal for different simulations corresponding to increasing supernova distance: light blue = 4.52, purple = 5.5, yellow = 6.53, blue = 7.43, green = 8.5, red = 9.69, black = 10.22 and light green = no signal.

In a completely identical way the plots of Fig. 5.11 have been produced for the same two reduction factors of the background already used in Section 5.1.2, a factor two and a factor ten. For each reduction factor, the distribution of reconstructed signal when no signal is simulated has been produced and the threshold choosen according to Eq. 5.12 and following. The distributions of the signal corresponding to the different distances have also been computed with the reduced background.

The effect of a reduction of the background rate on the discovery potential is striking. The reason is that the reduction affects both factors in the second term of Eq. 5.12 at the same time: R_{B+M} is the background rate itself, and the effect is streightforward: if the background rate is reduced by a factor two, the rate at which the trigger value
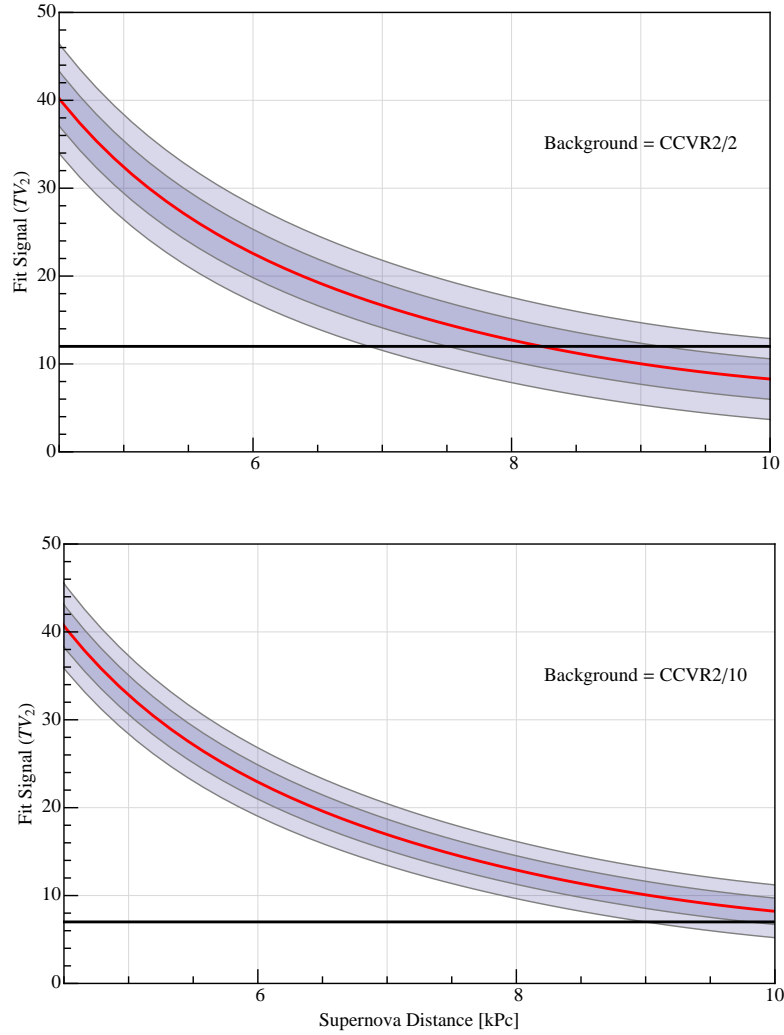
Figure 5.11: As in Fig. 5.9, but for reduced values of the background rate. Lowering the background, the interception between the threshold orizontal line and the bands corresponding to the fitted signal distribution moves towards larger distances, meaning an increase of the discovery potential.

TV_2 is evaluated is also reduced by a factor two and the probability of triggering a false signal (P_{FP}) can therefore be doubled without changing the average rate of false positives. The threshold on $\hat{S}$ (or TV_2) can consequently be reduced.

At the same time, the smaller is the background rate, the better the fit algorithm will perform, in terms of the estimation of the signal amplitude; for a supernova at a given distance, in fact, the signal-to-noise ratio is reduced proportionally to the squared root of the number of background events in the window. The effect is, also in this case, double: the cumulative distributions of the estimator $\hat{S}$ calculated when no signal

is present drop more rapidly when the background is reduced (see the comparison in Fig. 5.12), and the distributions of the same parameter corresponding to a given signal are in general narrower if the contribution of the background is smaller; this effect is evident when the widths of the 1 and 2σ bands are compared in the discovery power plots of Fig. 5.9 and Fig. 5.11.
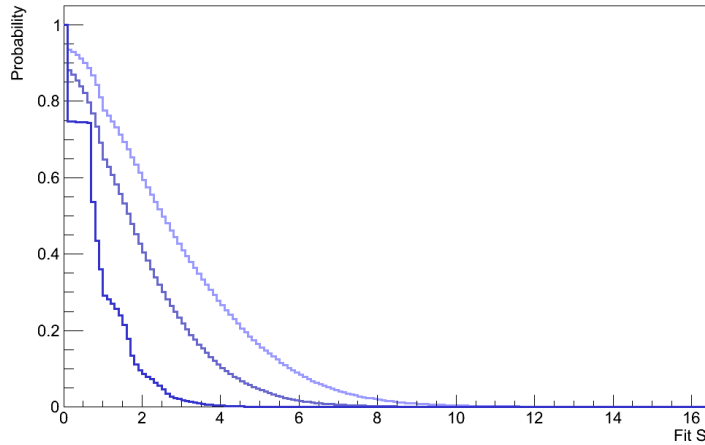

Figure 5.12: Distributions of the reconstructed value of the signal amplitude when no signal is present in the simulated data. The three curves correspond to the three different values of the background rate that have been studied. The smaller is the background, the narrower the distribution around zero.

To conclude the chapter, some numbers can be extracted from the plots, and they are reported in Tab. 5.1. The second and third column contain the distance at which the probability of detecting a supernova, the rate of false positive beeing fixed to 1/week, is respectively 50% and 98%. The last colum represent the probability of detecting a supernova at 8.5kPc.

Background reduction factor	d(P=0.5)[kPc]	d(P=0.98)[kPc]	P(d=8.5kPc)
1	7.1	5.8	0.09
0.5	8.2	6.9	0.40
0.1	>10	9.0	1

Table 5.1: Some significative numerical values of the trigger probability for different values of the background rate.

Chapter 6

Neutrino and nuclear physics from supernova observation and coherent scattering

6.1   Physics with supernovae

In the literature some studies can be found that show how constraints on supernova model parameters can be put based on the observation of neutrinos emitted during a supernova explosion.

The observation of neutrinos via coherent scattering in bolometers could help in improving some of these constraints, mainly because of the possibility of measuring the total, flavour independent, neutrino flux. In this section we show, in a qualitative way, what kind of information can be extracted from a supernova observation in CUORE about one of the crucial parameters of the model describing a supernova explosion, i.e. the temperature of the neutrinosphere where the emission occurs.

As already described in Section 2.3.1, the average energy of the neutrino spectra (or their temperature) is associated to the temperature of the matter at a distance from the proto-neutron star equal to the radius of the neutrinosphere, i.e. where the matter density is low enough to let the neutrinos free stream out of the supernova core. Since large uncertainties are associated to the temperature of the different neutrinospheres, a model-independent measurement of the neutrino spectra everage energy turns out to be of great importance. The total neutrino spectrum that can be observed via coherent scattering is the sum of the spectra of the three neutrino species emitted with three different neutrinospheres radii (see Section 2.3.1). As a consequence, the summed spectrum shape can be expressed as a function of three parameters: the temperature of

one of the spectra, for example $k_B T_{\nu_e}$, and the ratios $T_{\bar{\nu}_e}/T_{\nu_e}$ and T_{ν_x}/T_{ν_e}.

In Fig. 6.1 the effect of a variation in the temperature T_{ν_e}, with the other two parameters fixed, is shown by drawing the total spectra corresponding to variations of the 50% with respect to its original value, adopted in the calculations of Chapter 4.
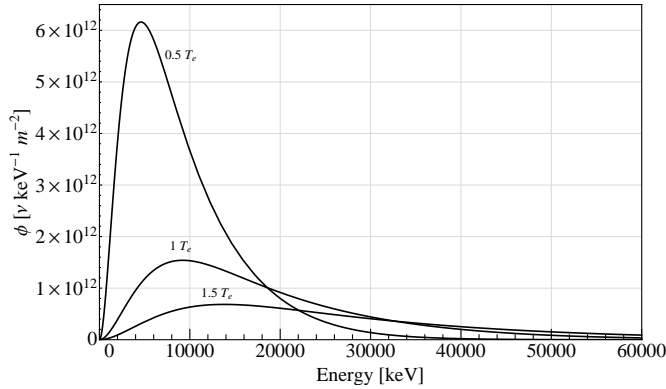

Figure 6.1: Effect of a variation in the electron neutrinos average temperature on the time integrated neutrino total spectra for a supernova distance of 8.5kPc.

By using the new, modified spectra as input for the calculation of the number of expected interactions in the CUORE detector, the sensitivity of the experiment to these variations of the model can be evaluated. For each value of the T_{ν_e} parameter, the spectrum of the nuclear recoils induced in the detector plus the already described low energy background is calculated and reported in Fig. 6.2. In this case the data are calculated for a supernova at 5kPc. The effect of the variations in the temperature parameter is quite predictable. A harder spectrum of the emitted neutrinos corresponds to a harder spectrum of nuclear recoils, while the total number of interactions doesn't change significantly: the reduction in the neutrino flux (the total available energy is the same but each neutrino has, on average, a larger energy) is compensated by the increase in the cross section due to the larger energy (see Eq. 2.48). On the contrary, a softer neutrino spectrum leads to a spectrum of the nuclear recoils that is squeezed towards the lower energies and almost all events are moved below few keV.

These modifications in the spectral shape could be directly appreciated with a fit of the spectrum of the low energy events in case of a large signal-to-noise ratio, i.e. in case of a near supernova. The evaluation of the total number of signal events would prove, in general, more sensitive, due to its strong dependence on the energy threshold. In Fig. 6.3 this dependence is explained: the total number of interactions expected in
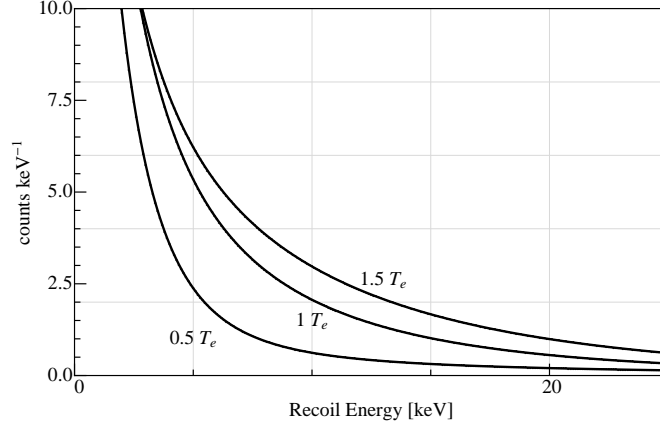
Figure 6.2: Effect of a variation in the electron neutrinos average temperature on the spectrum of nuclear recoils in the detector. E larger temperature corresponds to a smaller number of amitted neutrinos, but with a larger average energy. Their interaction in the detector will lead to a correspondingly harder spectrum of the nuclear recoils. The opposite happens if the temperature is smaller: a larger number of neutrinos is emitted, by the average nuclear recoil energy will be smaller and the corresponding spectrum squeezed below few keV.

the detector and detected above threshold drops drastically when the value of T_{ν_e} is reduced, because of the deformation of the exponentially shaped recoils spectrum that becomes steeper.

For a given energy threshold, a variation in the neutrino spectrum temperature would move a large fraction of the nuclear recoils below or above the threshold, thus sharply changing the total rate for a given supernova distance. The result is reported in Fig. 6.4.

Below $\sim$8.5kPc the curves corresponding to the three models are separated by more than 1σ, calculated as the statistical fluctuation of the number of signal and background counts.

6.2   Physics with coherent scattering

Neutrino-nucleus coherent scattering that proceeds via a neutral current interaction is a phenomenon that, from the theoretical point of view, is well understood and the corresponding cross sections can be calculated with little effort using Standard Model physics. As explained in Section 2.3.2, however, big uncertainties affect the calculation of the form factor that accounts for the distribution of the weak charge within the nucleus. This quantity cannot be easily extracted from direct measurements of the nucleon
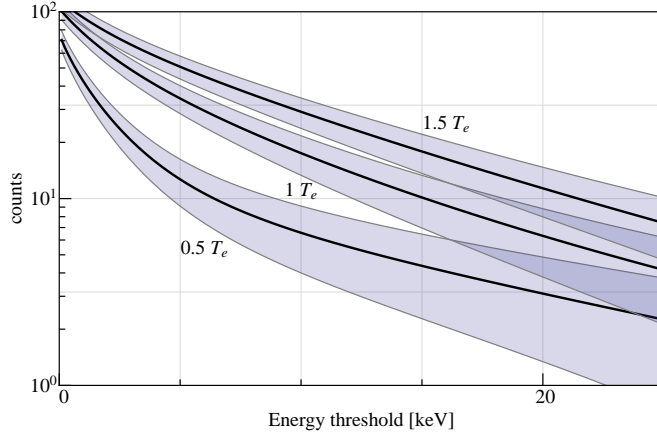
Figure 6.3: Total number of events in the detector as a function of the energy threshold, for three different values of the parameter T_{ν_e}, in case of a supernova at 5kPc; the shadowed bands represent 1σ flucuations of the number of counts.
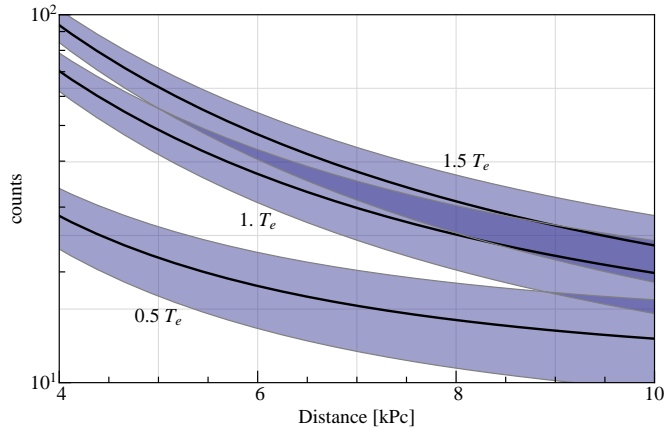

Figure 6.4: Effect of a variation in the electron neutrinos average temperature on the total number of nuclear recoils in the detector. The shadowed bands are 1σ statistical fluctuations of the number of events.

distribution performed with electron beams because in electron-nucleus scattering the electromagnetic effects completely overwhelm any weak interaction one. Only neutrinos can be used to directly probe the distribution of the weak charge, then.

The use of a detector capable of performing a measurement of coherent scattering interactions to explore the weak interaction-related features of the nuclear structure has been proposed, for example, by [67] and [68]. Typical noble gas detector used for

dark matter search could detect coherent scattering, but the choice of heavy elements to be used for this purpose is practically limited to xenon. Bolometric detectors, on the contrary, have been demostrated to have good performance with many different heavy elements rich compounds.

Demonstrating that a one-ton scale bolometric detector like CUORE can detect with high efficiency nuclear recoils from coherent scattering would be a proof of the feasibility of a study of nuclear structure using neutrinos as probes and many different heavy nuclei as target.

Let's imagine that an intense source of neutrinos (like the one proposed by [67] and [68]) could illuminate a CUORE-like detector. The expected neutrino flux at a distance of 20m from the source is $\sim 10^7 \nu s^{-1} cm^{-1}$ for each neutrino family. Since the neutrino flux is obtained from a stopped-pion source, three different neutrinos are generated, with correspondingly different energy spectra. The decay at rest of the pion ($\pi^+ \to \mu^+ + \nu_\mu$ generates a monochromatic muon neutrino with an energy of 29.9MeV. This emission is usually called *prompt* to distinguish it from the following emission of neutrinos from the muon decay, that is *delayed* by the muon-decay time scale ($\tau \simeq 2.2\mu$s). The muon also decays almost at rest emitting an electron neutrino and a muon antineutrino ($\mu^+ \to e^+ + \nu_e + \overline{\nu}_\mu$) with continuous spectra. Since CUORE bolometers cannot resolve time differences of the order of few micro-seconds and coherent scattering is flavour-blind, prompt and delayed neutrino emissions cannot be distinguished and the experiment would observe the total summed spectrum, that is reported in Fig. 6.5.
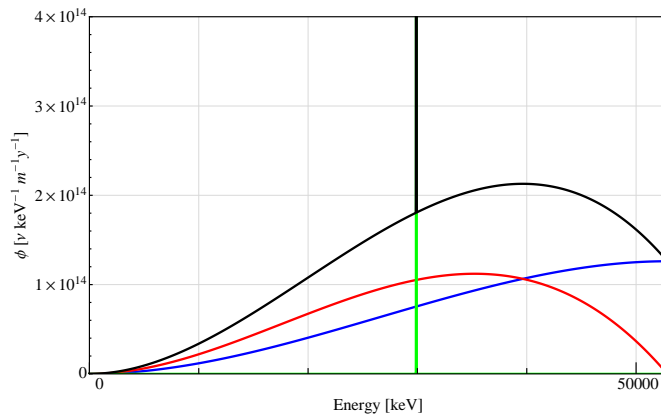

Figure 6.5: Spectra of neutrinos emitted by a stopped-pion source. Green = monochromatic emission from two-body pion decay; red = ν_e from muon decay; blue = $\overline{\nu}_\mu$ from muon decay. Black = summed spectrum.

Once the flux and the spectrum of neutrinos are known, the rate of events as a function of the recoil energy can be calculated in exactly the same way as with supernova neutrinos in Chapter 4. To understand if such a measurement could provide some information about the nuclear form factor, i.e. about the distribution of the weak charge inside the nucleus, a strategy similar to the one used in the previous section can be used: a parameter of the model is changed and the effect on the experimental signature is compared with the experimental uncertainties. In this case, the parameter that presents the largest theoretical uncertainty in the form factor model that was used so far (Eq. 2.53) is the so-called squared radius R_0, and R in particular. In Fig. 6.6 three spectra of the nuclear recoils are plotted; they represent the spectrum observed in the detector by integrating over one year the already mentioned flux of neutrinos, at a distance of 20m from the source. The same source used in [68], whose spectrum is represented in Fig. 6.5, was considered to allow a easier comparison of the results.
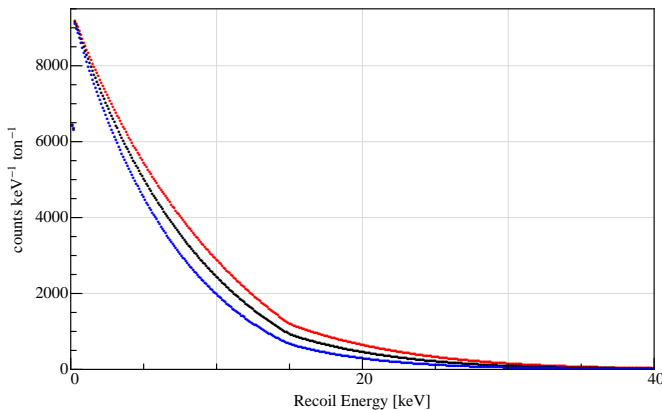

Figure 6.6: Spectra of nuclear recoils induced in CUORE by the hypothesized stopped-pion neutrino source. The three spectra correspond to three different values of the parameter R in the form factor, which is changed by $\pm 20\%$ with respect to the original theoretical value.

Due to the large statistics, the statistical fluctuation (of both signal and background), in this case, is expected to be small compared to other experimental uncertainties; the expected neutrino flux at the detector, for example, is reported ([67]) to be known with a 10% precision in stopped-pion sources like the Spallation Neutron Source (SNS) at Oak Ridge National Laboratory. The use of a single form factor for both neutron and proton distributions inside the nucleus is also an approximation whose effect, however, is expected to be completely negligible on this scale. In Fig. 6.7 the same data of Fig. 6.6

are reported, but the events are grouped in 5keV bins. For each bin the expected number of events is calculated for the three values of the parameter R (blue and dashed black lines); experimental error bands (including all the described contributions summed in quadrature) are added (red thin lines) to the histogram which corresponds to the central theoretical value.
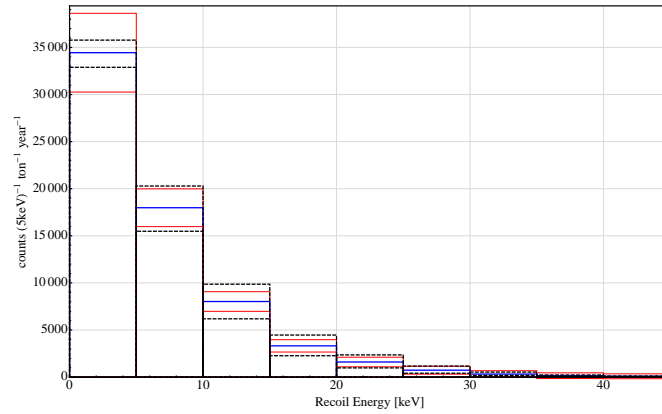
Figure 6.7: Spectra of nuclear recoils induced in CUORE by the hypothesized stopped-pion neutrino source. The spectra are binned with 5keV wide bins. The blue spectrum corresponds to the central value of the parameter R in the form factor; the black dashed spectra are obtained by changing R by $\pm 20\%$ with respect to the original theoretical value; the red thin lines are the experimental errors associated to the blue spectrum.

Figure 6.8: As in Fig. 6.7, but in each bin the number of counts corresponding to the expected theoretical value of R (blue spectrum) has been subtracted and red lines include the background fluctuations.

Fig. 6.8 also rapresents the same data, but for each bin the number of events corresponding to the standard theoretical predi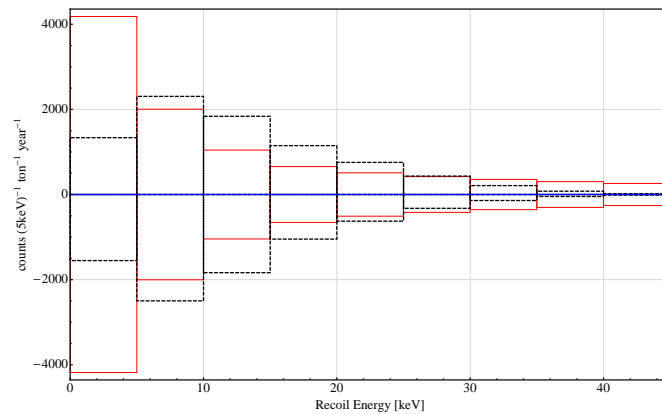ction (blue line in Fig. 6.7) has been subtracted in order to enhance the detail. The experimental uncertainties, including the background (the already used CCV2 background reduced by a factor 10 for CUORE) fluctuation, are included in the red bands.

As expected the sensitivity of the measurement is small in the first bins; at low recoil energies, corresponding to small momentum transferred in the interaction, the form factor converge to one, no matter the value of the parameter R. Below 5keV and above 25keV the experimental error (red bands), which is dominated by the uncertainty on the source flux, is larger than the spread due to the 20% variation of the parameter. The situation changes above 5keV: here the effect of the difference in the form factor is magnified because the tranferred momentum is increased, while the relative experimental error is almost constant because the statistical fluctuation is still small. Between 5 and 25keV the three models can be discriminated with about 2σ sensitivity.

Conclusions

The purpose of the work I presented in this PhD thesis was to show the feasibility of using the CUORE experiment as a real time detector for neutrinos emitted during a galactic core-collapse supernova explosion. This result would be obtained by exploiting ν-nucleus coherent scattering, that generates nuclear recoils within the detector crystals lattice, to detect neutrinos. This neutral-current mechanism is flavour blind, thus it allows to detect neutrinos of all families with the same efficiency; this represents a big advantage on currently operated neutrino telescopes (that usually detect electron neutrinos via charged-current interactions) and would provide a complementary observation from many points of view.

It is shown in these pages that, depending on the background level that CUORE will achieve, a supernova as far as 10kPc can be detected by a real-time trigger algorithm, with a rate of false positives not exceeding 1/week. By realeasing this constraint, the same discovery power can be achieved with a higher background level. Furthermore, an offline analysis of the data collected during the lapse where the supernova neutrinos are expected to interact would bring to an observation of the time distribution of the neutrino interactions with a statistical significance of more than 4σ for a core-collapse occurring in the galactic center region. In the case of an event at this distance, a comparison between the observed number of interactions and the expected total flux would allow to constraint some of the parameters of the model that describes the neutrinos emission.

An important collateral result of this work is to demonstrate that coherent scattering, which is the mechanism of intercation of the supernova neutrinos with CUORE detectors, can be observed in case of a supernova explosion. This observation would be, by itself, a big achievement because, due to the tiny cross section, this process, even if forseen by the Standard Model, has never been observed, and it is hard to conceive an experiment that could observe it with a man-made neutrino source.

List of publications
of Matteo Biassoni

Publications on refereed journals

- *"Validation of techniques to mitigate copper surface contamination in CUORE"*,
  F. Alessandria *et al.* (the CUORE collaboration),
  arXiv:1210.1107

- *"Search for 14.4 keV solar axions from M1 transition of Fe-57 with CUORE crystals"*,
  F. Alessandria *et al.* (the CUORE collaboration),
  arXiv:1209.2800

- *"The low energy spectrum of TeO$_2$ bolometers: results and perspectives for the CUORE-0 and CUORE experiments"*,
  F. Alessandria *et al.* (the CUORE collaboration),
  arXiv:1209.2519

- *"Study of Supernova ν-Nucleus Coherent Scattering Interactions"*,
  M. Biassoni and C. Martinez,
  Astroparticle Physics, vol. 36, pp. 151-155 (2012)

- *"First measurement of the partial widths of ^{209}Bi decay to the ground and to the first excited states"*,
  J.W. Beeman *et al.*,
  Physical Review Letters, vol. 108, 062501 (2012)

- *"Sensitivity of CUORE to Neutrinoless Double-Beta Decay"*,
  F. Alessandria *et al.* (the CUORE collaboration),
  arXiv:1109.0494

- *"CUORE crystal validation runs: results on radioactive contamination and extrapolation to CUORE background"*,
  F. Alessandria *et al.* (the CUORE collaboration),
  Astroparticle Physics, vol. 35, pp. 839-849 (2012)

- *"Response of a TeO$_2$ bolometer to alpha particles"*,
  F. Bellini *et al.*,
  Journal of Instrumentation, vol. 5, P12005 (2010)

Talks, posters, proceedings and internal notes

- *"Da CUORICINO a CUORE"*,
  Invited Talk at SIF 2010, Congresso della Società Italiana di Fisica (Bologna, Italy, September 20-24, 2010).

- *"From CUORICINO result to CUORE-0 startup: CUORE begins"*,
  Poster at BLV2011, Third International Workshop on Barion and Lepton Number Violation (Gatlinburg, Tennessee, September 22-24, 2011).
  Poster published on website.

- *"Rivelazione di neutrini da supernova nell'esperimento CUORE"*,
  Talk at SIF 2011, Congresso della Società Italiana di Fisica (L'Aquila, Italy, September 26-30, 2011).

- *"Low energy performance and coherent detection of supernova neutrinos in CUORE-0 and CUORE experiment"*,
  Poster at Neutrino 2012, The XXV International Conference on Neutrino Physics and Astrophysics (Kyoto, Japan, June 3-9, 2012).
  Published on the Booklet of Poster Abstract of the Conference.

- *"Prestazioni a bassa soglia e rivelazione coerente di neutrini da supernova in CUORE-0 e CUORE"*,
  Talk at IFAE 2012, Incontri di Fisica delle Alte Energie (Ferrara, Italy, April 11-13, 2012).
  Best communication award.
  Proceeding in print.

- *"Study of Supernova ν detection in CUORE"*,
  Internal Note to the Collaboration.

- *"Experimental study of TeO_2 bolometers response to particle interactions in thermistors and glue spots"*,
  Internal Note to the Collaboration.

Bibliography

[1] M. Biassoni and C. Martinez, "Study of Supernova ν-Nucleus Coherent Scattering Interactions," *Astroparticle Physics*, vol. 36, pp. 151–155, 2012. 2, 56, 60

[2] F. Bellini *et al.*, "Response of a TeO$_2$ bolometer to α particles," *Journal of Instrumentation*, vol. 5, p. P12005, 2010. 3

[3] A. Strumia and F. Vissani, "Neutrino masses and mixings and...." arXiv: 0606054[hep-ph], 2010. 5

[4] M. Fehr, M. Rehkamper, and A. Halliday, "Application of MC-ICPMS to the precise determination of tellurium isotope composition in chondrites, iron meteorites and sulfides," *International Journal of Mass Spectrometry*, vol. 232, pp. 83–94, 2004. 8

[5] M. Vignati, *Model of the Response Function of CUORE Bolometers.* Springer Verlag, 1 ed., 2011. ISBN 978-94-007-1231-7. 8

[6] A. Miller and E.Abrahams, "Impurity conduction at low concentrations," *Physical Review*, vol. 120, pp. 745–755, 1960. 9

[7] N. Mott and J. Davies, "Metalinsulator transition in doped semiconductors," *Philosophical Magazine B*, vol. 42, pp. 845–858, 1980. 9

[8] C. Arnaboldi *et al.*, "Results from a search for the $0\nu\beta\beta$-decay of ^{130}Te ," *Physical Review*, vol. C78, p. 035502, 2008. 14, 23

[9] F. Alessandria *et al.*, "Cuore crystal validatino runs: results on the radioactive contamination and extrapolation to cuore background," *Astroparticle Physics*, vol. 35, p. 839, 2012. 20, 70, 78, 86

[10] S. D. Domizio, *Search for double beta decay to excited states with CUORICINO and data acquisition system for CUORE.* PhD thesis, Università degli Studi di Genova, 2009. http://fisica.unige.it/~dottorato/images/stories/Tesi/XXI/DiDomizii.pdf. 21

[11] F. Orio and M. Vignati, "Very Low Threshold Analysis in CUORE," tech. rep., CUORE Collaboration, 2010. 27

[12] B. Aharmin *et al.*, "Combined analysis of all three phases of solar neutrino data from the Sudbury Neutrino Observatory." arXiv: 1109.0763[nucl-ex], 2011. 34

[13] G. Bellini *et al.*, "Precision measurement of the ^{7}Be solar neutrino interaction rate in Borexino," *Physical Review Letters*, vol. 107, p. 141302, 2011. 34

[14] K. Abe *et al.*, "Solar neutrino results in Super-Kamiokande-III," *Physical Review D*, vol. 83, p. 052010, 2011. 34

[15] S. Abe *et al.*, "Precision measurement of neutrino oscillation parameters with Kam-LAND," *Physical Review Letters*, vol. 100, p. 221803, 2008. 34

[16] F. An *et al.*, "Observation of electron-antineutrino disappearance at Daya Bay," *Physical Review Letters*, vol. 108, p. 171803, 2012. 34

[17] N. Agafonova *et al.*, "Search for $\nu_\mu \to \nu_\tau$ oscillation with the OPERA experiment in the CNGS beam." arXiv: 1107.2594[hep-ex], 2011. 34

[18] C. Weizsäcker, "Zur Theorie der Kernmassen," *Zeitschrift für Physik*, vol. 96, pp. 431–458, 1935. 40

[19] J. Schechter and J. Valle, "Neutrinoless double-β decay in SU(2)×U(1) theories," *Physical Review D*, vol. 25, pp. 2951–2954, 1982. 42

[20] F. Avignone, S. Elliott, and J. Engel, "Double Beta Decay, Majorana Neutrinos, and Neutrino Mass," *Reviews of Modern Physics*, vol. 80, pp. 481–516, 2008. 43

[21] J. Menendez, A. Poves, E. Caurier, and F. Nowacki, "Deformation and the Nuclear Matrix Eements of the Neutrinoless Double Beta Decay." arXiv: 0809.2183[nucl-th], 2008. 44

[22] I. Ogawa *et al.*, "Search for neutrino-less double beta decay of Ca-48 by CaF-2 scintillator," *Nuclear Physics*, vol. A730, pp. 215–223, 2004. 48

[23] H. Klapdor-Kleingrothaus *et al.*, "Latest Results from the HJeidelberg-Moscow Double Beta Decay Experiment," *European Physical Journal*, vol. A12, pp. 147–154, 2001. 48

[24] R. Arnold *et al.*, "First results of the search of neutrinoless double beta decay with the nemo 3 detector," *Physical Review Letters*, vol. 95, p. 182302, 2005. 48

[25] F. Danevich *et al.*, "Search for 2 beta decay of cadmium and tungsten isotopes: Final results of Solotvina experiment," *Physical Review C*, vol. C68, p. 035501, 2003. 48

[26] C. Arnaboldi *et al.*, "Results from a search for the $0\nu\beta\beta$-decay of ^{130}Te," *Physical Review C*, vol. C78, p. 035502, 2008. 48

[27] R. Bernabei *et al.*, "Investigation of beta beta decay modes in Xe-134 and Xe-136," *Physics Letters B*, vol. B546, pp. 23–28, 2002. 48

[28] J. Argyriades *et al.*, "Measurement of the double-β decay half-life of ^{150}Nd and search for neutrinoless decay modes with NEMO-3 detector," *Physical Review C*, vol. C80, p. 032501, 2009. 48

[29] R. Mohapatra and P. Pal, *Massive Neutrinos in Physics and Astrophysics*. World Scientific, 3 ed., 2004. 47

[30] S. Elliott and P. Vogel, "Double Beta Decay," *Annual Review of Nuclear and Particle Science*, vol. 52, pp. 115–151, 2002. 47

[31] F. Alessandria *et al.*, "The low energy spectrum of TeO$_2$ bolometers: results and perspectives for the CUORE-0 and CUORE experiments." arXiv: 1209.2519[physics.ins-det], 2012. 48, 86, 87, 109

[32] C. Giunti and C. Kim, *Foundamentals of Neutrino Physics and Astrophysics*. Oxford University Press, 1 ed., 2012. 50, 57

[33] B. Sugerman *et al.*, "A New View of the Circumstellar Environment of SN1987A," *Astrophysical Journal*, vol. 627, pp. 888–903, 2005. 50

[34] R. Manchester *et al.*, "Imaging of the Radio Remnant of SN1987A at 12 mm Wavelength," *Astrophysical Journal*, vol. 628, pp. L131–L134, 2005. 50

[35] D. B. S. Park, S.A. Zhekov and R. McCray, "Supernova Remnant 1987A: Opening the Future by Reaching the Past," *Astrophysical Journal*, vol. 634, pp. L73–L76, 2005. 50

[36] P. Bouchet *et al.*, "SN1987A After 18 Years: Mid-Infrared GEMINI and SPITZER Observations of the Remnant," *Astrophysical Journal*, vol. 650, pp. 212–227, 2006. 50

[37] V. Trimble, "1987A: The greatest supernova since Kepler," *Review of Modern Physics*, vol. 60, pp. 859–871, 1988. 50

BIBLIOGRAPHY

[38] M. Koshiba, "Observational neutrino astrophysics," *Physics Reports*, vol. 220, pp. 229–381, 1992. 50

[39] J. Wheeler, "Observations and Theory of Supernovae," *American Journal of Physics*, vol. 71, pp. 11–22, 2003. 50

[40] S. Colgate and R. White, "The Hydrodynamic Behavior of Supernovae Explosions," *Astrophysical Journal*, vol. 143, pp. 626–681, 1966. 54

[41] H. Bethe and R. Wilson, "Revival of a stalled supernova shock by neutrino heating," *Astrophysical Journal*, vol. 295, pp. 14–23, 1985. 54

[42] S. Woosley and H. Janka, "The Physics of Core-Collapse Supernovae," *Nature Physics*, vol. 1, pp. 147–154, 2006. 54

[43] A. Burrows, E. Livne, L. Dessart, C. Ott, and J. Murphy, "A New Mechanism for Core-Collapse Supernova Explosions," *Astrophysical Journal*, vol. 640, pp. 878–890, 2006. 54

[44] S. Shapiro and S. Tekolsky, *Blacj Holes, White Dwarfs, and Neutron Stars: The Physics of Compact Objects.* John Wiley, 1983. 55

[45] C. Horowitz, K. Coakley, and D. McKinsey, "Supernova Observation Via Neutrino-Nucleus Elastic Scattering in the CLEAN Detector," *Physical Review*, vol. D68, p. 023005, 2003. 56

[46] T. Totani, K. Sato, H. Dalhed, and J. Wilson, "Future Detection of Supernova Neutrino Burst and Explosion Mechanism," *Astrophysical Journal*, vol. 496, pp. 216–225, 1998. 58

[47] J. Gava, J. Kneller, C. Volpe, and G. McLaughlin, "A dynamical collective calculation of supernova neutrino signals," *Physical Review Letter*, vol. 103, p. 071101, 2009. 59

[48] F. Vissani and G. Pagliaroli, "How much can we learn from SN1987A events? Or: An analysis with two-Component model for the antineutrino signal." arXiv: 0807.1301[astro-ph], 2008. 59

[49] M. Costantini, A. Ianni, and F. Vissani, "The interest in neutrinos from core collapse supernovae," *Nuclear Physics B (Proc. Suppl.)*, vol. 139, pp. 27–32, 2005. 59, 60

[50] C. Horowitz, S. Pollock, P. Souder, and R. Michaels, "Parity violating measurements of neutron densities," *Physical Review*, vol. C63, p. 025501, 2001. 61

[51] J. Engel, "Nuclear form factors for the scattering of weakly interacting massive particles," *Physics Letters B*, vol. 264, pp. 114–119, 1991. 61

[52] A. Alessandrello *et al.*, "Preliminary results on double beta decay of ^{1}30Te with an array of twenty cryogenic detectors," *Physics Letter B*, vol. 433, p. 156, 1998. 66

[53] C. Bucci *et al.*, "Background study and Monte Carlo simulations for large-mass bolometers," *European Physical Journal A*, vol. 41, pp. 155–168, 2009. 66, 69, 70, 76

[54] C. Arnaboldi *et al.*, "New Limit on the Neutrinoless $\beta\beta$ Decay of ^{1}30Te," *Physical Review Letters*, vol. 95, p. 14501, 2005. 66

[55] C. Arnaboldi *et al.*, "Results from the CUORICINO neutrinoless double beta decay experiment," *Physical Review C*, vol. 78, p. 035502, 2008. 66

[56] E. Andreotti *et al.*, "^{130}Te Neutrinoless Double-Beta Decay with CUORICINO," *Astroparticle Physics*, vol. 34, p. 822, 2011. 66, 86

[57] R. Ardito *et al.*, "CUORE: A Cryogenic underground Observatory for Rare Events," 2005. arXiv: 0501010[hep-ex]. 66

[58] M. Pavan *et al.*, "Control of bulk and surface radioactivity in bolometric searches for double-beta decay," *European Physical Journal A*, vol. 36, pp. 159–166, 2008. 66, 70

[59] CUORE Collaboration, "LNGS Annual Report year 2006." 2006. 70

[60] F. Alessandria *et al.*, "Validation of techniques to mitigate copper surface contamination in cuore." arXiv: 1210.1107[nucl-ex], 2012. 70

[61] A. Alessandria *et al.*, "Measurements of residual radioactivity in neutron transmutation doped thermistors," *Nuclear Instruments and Methods in Phisics Research B*, vol. 93, pp. 322–325, 1994. 72

[62] F. Bellini *et al.*, "Monte Carlo evaluation of the external gamma, neutron and muon induced background sources in the CUORE experiment," *Astroparticle Physics*, vol. 33, pp. 169–174, 2010. 82, 86

[63] L. Weathers and M. Tsang, "Fabrication of thin scintillator foils," *Nuclear Instruments and Methods in Physics Research A*, vol. 381, pp. 567–568, 1996. 91

[64] G. Angloher *et al.*, "Results from 730kg days of the CRESST-II Dark Matter search," *European Physical Journal C*, vol. 72, p. 1971, 2012. 92

[65] J. Beeman *et al.*, "First Measurement of the Partial Widths of ^{209}Bi Decay to the Ground and to the First Excited States," *Physical Review Letters*, vol. 108, p. 062501, 2012. 92

[66] W. Eadie, D. Drijard, F. James, M. Roos, and B. Sadoulet, *Statistical Methods in Experimental Physics*. North-Holland, 1971. 126

[67] P. Amanik and G. McLaughlin, "Nuclear neutron form factor from neutrino-nucleus coherent elastic scattering," *Journal of Physics G*, vol. 36, p. 015105, 2009. 138, 139, 140

[68] K. Scholberg, "Prospects for measuring coherent neutrino-nucleus elastic scattering at a stopped-pion neutrino source," *Physical Review D*, vol. 73, p. 033005, 2006. 138, 139, 140

Ringraziamenti

Durante il dottorato si incontrano e conoscono tante persone, fisici e non, e ciascuna di loro ha sicuramente contribuito a construire un pezzettino del fisico - e della persona - che sono. Sarebbe giusto ringraziarle tutte, anche se magari, nel momento in cui davano il loro contributo alla mia crescita, non la pensavo proprio così... Alcune persone, però, sono state davvero importanti in questi tre anni, e meritano una citazione esplicita.

Carlo (anche noto come "diamo a Cesare quel che è di Cesare") che mi ha insegnato tante tante cose ma, soprattutto, che in fondo non c'è niente di male nell'avere sempre ragione. Grazie C Bucci.

Paolo (anche noto come Carlo) che mi ha insegnato tante cose ma, soprattutto, che non ho sempre ragione (e che fare parte o meno di un'elite è solo questione di scelte...). Grazie Paolo.

Marisa (anche nota come Signora Professoressa) che in tante occasioni ha dimostrato di fidarsi di me, e che mi ha insegnato, soprattutto, che non c'è niente di male nel buttare Paolo fuori dal suo ufficio per fare una telefonata. Grazie Marisa.

Oliviero che, silenziosamente e discretamente, ha sempre appoggiato le mie scelte e cercato di guidarmi, trattandomi e facendomi sentire "alla pari". Grazie C Olli.

Marco, Elena e Claudia che, nonstante discussioni, divergenze e lunghissime ore chiusi in una clean-room, sono compagni ed amici preziosi con cui confrontarsi senza (o quantomeno con pochi) filtri. Grazie Marco, Elena, Claudia.

Naturalmente, ancora una volta, come tre e cinque anni fa, la mia famiglia, che, nonostante la mia pressoché inesistente capacità di tenerla al corrente di quello che faccio e che mi succede, è comunque, sempre, un appoggio sicuro. Grazie perché vi fidate di me, mamma, papà, Fede, nonna.

E grazie a te, Alessandra Carlotta, per avermi scoperto. Per essere stata capace di conoscermi e accettarmi e per essere capace ogni giorno di farmi sentire che mi conosci e accetti. Per avermi fatto pensare, sinceramente, che con te sto diventando una persona migliore. Grazie per aver voluto iniziare questo viaggio insieme, e per essere pronta a continuarlo, semestre dopo semestre... Grazie Ale.